GENERATION OF CORE/SHELL NANOPARTICLES WITH LASER ABLATION

A Dissertation

by

YOUNG KYONG JO

Submitted to the Office of Graduate Studies of
Texas A&M University
in partial fulfillment of the requirements for the degree of

DOCTOR OF PHILOSOPHY

August 2012

Major Subject: Mechanical Engineering

Generation of Core/shell Nanoparticles with Laser Ablation

Copyright 2012 Young Kyong Jo

GENERATION OF CORE/SHELL NANOPARTICLES WITH LASER ABLATION

A Dissertation

by

YOUNG KYONG JO

Submitted to the Office of Graduate Studies of
Texas A&M University
in partial fulfillment of the requirements for the degree of

DOCTOR OF PHILOSOPHY

Approved by:

Chair of Committee,	Sy-Bor Wen
Committee Members,	Chii-Der Suh
	Choongho Yu
	Hae-Kwon Jeong
Head of Department,	Jerry Caton

August 2012

Major Subject: Mechanical Engineering

ABSTRACT

Generation of Core/shell Nanoparticles with Laser Ablation. (August 2012)
Young Kyong Jo, B.E.; M.E., Kyung Hee University
Chair of Advisory Committee: Dr. Sy-Bor Wen

Two types of core/shell nanoparticles (CS-NPs) generation based on laser ablation are developed in this study, namely, double pulse laser ablation and laser ablation in colloidal solutions. In addition to the study of the generation mechanism of CS-NPs in each scheme, the optical properties of designed CS-NPs are determined with UV-VIS-NIR spectroscopy and EM field simulation.

In the first scheme, which is double pulse laser ablation, two laser beams are fired in a sequence on two adjacent targets with different material. We have successfully demonstrated the generation of Sn/Glass, Zn/Glass, Zn/Si, Ge/Si, and Cu/Zn CS-NPs. Key factors affecting the generation of CS-NPs are (1) surface tensions of the constructing materials affecting the associated Gibbs free energy of CS-NPs, (2) physical properties of selected background gases (i.e., He and Ar), (3) delay time between two laser pulses, and (4) the amount of laser energy.

The second scheme examined for the generation of CS-NPs is through laser ablation of solid targets in colloidal solutions. Compared to the double pulse laser ablation, this second approach provides better control of the size and shape of the resulting CS-NPs. Two colloidal solutions, namely, Au and SiO_2 colloidal solution are applied in the second scheme. Key factors affecting the formation of CS-NPs with the second scheme and are (a) the adhesion energy between the shell and the core material, (b) the diameter of the core and (c) the laser ablation time and the laser energy.

Red shift of absorption peaks are measured in both SiO_2/Au and SiO_2/Ag colloids compared with pure nanoparticles (NPs). The amount of red-shift is very sensitive to the shell thickness of the CS-NPs. The same red shift is reproduced with the corresponding full wave analysis. The observed red shift can be attributed to the additional surface plasmon resonance at the interface of metal/dielectric of the CS-NPs compared with pure nanoparticles. Through adjusting the material and size combination, the absorption peak of the CS-NPs can be tuned in a limit range around the intrinsic absorption peak of the metal of the CS-NPs. The freedom of adjusting the absorption peak makes CS-NPs is favorable in bio and optical applications.

DEDICATION

To my family

ACKNOWLEDGEMENTS

I wish to express my sincere gratitude to my advisor, Dr. Sy-Bor Wen, for his guidance and advice during my Ph.D study. Also, I would like to thank my committee members, Dr. Suh, Dr. Yu, and Dr. Jeong for their kind help and support.

I would like to thank my labmates, Alok Soni, Vijay Meenashi Sundaram, Yu Yang, and Chien-Fan Chen for their valuable discussions, comments and technical assistance on my research. I would also like to thank all the other group members who had worked with me in the office and lab for the past four and a half years.

Finally, I would like to thank my family. Special thanks to my husband, father and mother who have been my source of energy to overcome the difficulties during my Ph.D study.

.

TABLE OF CONTENTS

Page

LIST OF FIGURES

Page

Page

Page

Page

Page

Page

Page

LIST OF TABLES

Page

1. INTRODUCTION

1.1 Pulsed Laser ablation

Laser ablation is a removal of material from a surface through an intense irradiation of a pulsed laser energy. Laser ablation has attracted attention in many areas of science and technology and has been applied in many field such as nanoparticles generation [1], pulsed laser deposition [2], laser surface cleaning [2], and microelectronic device fabrication [3].

The evaporation of a target during laser ablation can be owing to either thermal or non-thermal mechanisms, or sometimes both, depending on the laser wavelength, the pulse duration and the material been ablated [4]. The evaporation of the material with laser starts from the absorption of the laser energy during laser-material interaction. When a pulsed laser beam strikes on the surface of an opaque solid target, part of the incident energy is reflected, and the remaining part is absorbed within a few times of the optical depth of the target. In general, photons can couple with both electron and vibrational modes of the target material. For insulators and semiconductors, the light absorption is dominantly occurred through resonant excitations of the interband transitions or intersubband transitions of electrons [5]. Photons with energy below the band gap of the insulators and semiconductors are unlikely to be absorbed with insulators and semiconductors. In metals, the absorption of laser light is dominated with the free electrons in the conduction band through the mechanisms such as inverse bremsstrahlung (free-free transition).

This dissertation follows the style of *IEEE Journal of Quantum Electronics.*

Energy of excited electrons of metal, semiconductor and insulator during laser-material interaction is subsequently transferred to lattice phonons through electron-photon scattering and causes the heating of the material. The requiring time of the excited electron states to transfer energy to phonons is ~10^{-12} –10^{-10} s for metals and 10^{-6} s for non-metals.

When laser-induced electron excitation rate is low in comparison to the thermalization rate through electron-photon scattering, most of the absorbed laser energy is converted into heat of the material. This process is called photothermal (pyrolytic) processing and the material response can be treated in a purely thermal way. For example, laser processing of metals or semiconductors with nanosecond pulsed laser are considered in this category. If the laser induced excitation rate is high in comparison with the thermalization rate, large electron excitations can build up in the intermediary states. This type of non-thermal material modification is typically referred to as photochemical (photolytic) processing. For instance, material processing with ultrafast femtosecond laser can be described as non-thermal process such as Coulomb explosion [6].

In the current study, ablations are involved with nanosecond pulsed laser ablation through photothermal processing. During nanosecond laser ablation, the photon-electorn excitation and the followed electron-phonon relaxation results in the temperature increase of the sample material during the nanosecond laser pulse. As temperature increases above the melting temperature, a liquid interface is formed and propagates into the material. At the meantime, the surface of the sample material begins to evaporate and expand into background. The temperature of vapor plume can be much higher the critical temperature of the material and is mainly in a plasma phase. The formation of laser induced plasma is within ~100's ps to ~1' ns during the laser irradiation. The high temperature plasma can further absorb the incoming laser energy and to reach higher temperature through photoiozation and inverse bremsstrahlung. The reflection of the following laser energy with the laser induced plasma so-called plasma shielding [7]. Due

to the plasma shielding, only a fraction of nanosecond laser energy is actually used in the ablation process.

At the end of the nanosecond laser pulse, the major evaporation of sample stops. Stored thermal energy in the condensed region of the ablation system is mainly dissipated with conduction, which results in a generation of material waves from near the laser spot through the material. At the same time, the laser induced vapor plume expands into the background rapidly. If the laser ablation is conducted in a background gas, shockwaves are generated in the gas region owing to the rapid expansion of the vaporized material which compresses the background gas. During the plume expansion, the thermal energy stored in the plume is released to the ambient and causes the temperature drops of the vaporized material. When the temperature of vapor plume is lower than the melting temperature of sample material, condensation of vapor plume happens and leads to the generation of nano-material through either homogeneous or heterogeneous nucleation.

There are several advantages in material processing with the laser ablation compared with the conventional methods such as physical machining and chemical methods. For example, the laser ablation can be applied to almost every solid material with little sample preparation when the laser parameters such as wavelength or laser energy are properly selected. In addition, laser ablation is a fast process causing limited thermal damage of the base material, which is required in many precise material processing.

1.2 Core/Shell Nanoparticles

1.2.1 Application

Core-shell nanoparticles (CS-NPs), a group of nanoparticles (NPs) composed with layered structures of different material, have received a significant attention recently. The CS-NPs can provide several unique features compared to traditional NPs with

uniform structures. First of all, optical properties can be tuned with CS-NPs by adjusting the material composition and size/shape of the CS-NPs [8-10]. For example, it has been reported that emission and absorption peaks of CS-NPs can be tweaked by adjusting the surface plasmon and localized plasmon frequencies of the CS-NPs. The surface plasmon and localized plasmon frequencies of the CS-NPs are function of the dielectric constant and size ratio of the core and shell(s) material of the CS-NPs. [9, 11-12]. In addition to the adjustable optical properties, CS-NPs can provide magnetic properties such as enhanced ferromagnetism, super-paramagnetism, or coercivity comapred with single element NPs [13-14]. Furthermore, chemical properties such as catalytic efficiency can be significantly improved with the combinations of selected types core/shell materials. For instance, Ru/Pt CS-NPs exhibited less CO poisoning at the fuel cell system, and Pt/Pd CS-NPs presented a great electrocatalysis compared with single element nano-particles [15-16]. Due to the capability to freely designing and adjusting their physical properties, CS-NPs have potentials to further advance the applications of NPs in optical, electrical, and bio applications [12, 17-22].

1.2.2 Fabrication methods

Several generation methods have been reported to create the CS-NPs of various configurations. For instance, a significant portion of studies have been focused on wet-chemistry method which involves the chemical reaction between seed materials (either core or shell) and surrounding liquids for generating core/shell structure [23]. A wide group of wet-chemistry method have been reported such as reverse micelles [24], sol-gel process [25], and polymerization [26]. However for large scale production, wet-chemistry methods, sometimes, are not eco-friendly because they are inherently batch processes that require the use and disposal of environmentally hazardous solvents [27]. In addition to wet-chemistry methods, physical methods have also been created for CS-NPs generation. Physical methods have advantages over wet-chemistry methods owing to their intrinsic in-situ processes requiring less sample preparation and do not require

eco-hazard solvents. Such physical method includes particle coating processes using spray pyrolysis [28], heated flow tubes [29-33], flame synthesis [34-35] and plasma methods [36-38]. All these methods produces CS-NPs require relatively short production times with little involvement of solvents and minor sample preparations. Laser ablation is one of the physical methods capable in generating NPs. A few schemes have been established for generating CS-NPs with laser ablation such as laser ablation in reactive gases [14, 39-41], laser ablation in liquids [42-45]. Generally, laser ablation can be applied in a wide variety of materials. Therefore, it has advantages in fast processing and high flexibilities in material selection of CS-NPs [46-47]. In addition, CS-NPs with laser ablation, like most physical methods, is an in-situ generation process with few required generation steps and little sample preparation. These combined advantages of CS-NPs generation with laser ablation allow it to be a potential platform for generating all types of CS-NPs with specified material combination, which is important in the experimental characterization of physical/chemical properties of CS-NPs with different size, shape, and material combination for electrical, optical, bio and chemical applications.

1.3 Dissertation Objectives and Outline

The main purpose of this study is to introduce new CS-NPs generation methods with advantages of ns laser processing. As described above, nanosecond laser ablation provides versatility and simplicity in material processing, which can allow the generation of CS-NPs with a wide variety of combination through a relatively simpler process compared with traditional chemical methods. Two new type of CS-NPs generation processes are developed in this study with ns laser ablation, namely, double-pulse laser ablation and laser ablation in colloidal solution.

In chapter II, the first CS-NPs generation scheme, which is double pulse laser ablation, is introduced. In-situ plume dynamics and particle formation during double laser ablation are studied with the thermal emission and laser induced luminescence imaging to

identify the appropriate experimental conditions and the key factors determining the generation of CS-NPs with double pulse laser ablation. In chapter III, the second CS-NPs formation method, laser ablation in colloidal solution, is presented. Key factors determining the generation of CS-NPs through ablation in colloidal solutions are also studied in this chapter. In chapter IV, optical characteristics of resulting CS-NPs from laser ablation are examined with the UV-VIS-NIR spectroscopy and explained with corresponding full wave electrodynamics analysis. In chapter V, concluding remarks are presented to summarize the findings of this study and the applicable future research.

2. GENERATION OF CS-NPs WITH DOUBLE PULSE LASER ABLATION

2.1. Introduction

Laser ablation provides a possible root of fast processing and high flexibility in producing designed CS-NPs generation. CS-NP generation with laser ablation, generally speaking, involves a few standard steps and is especially useful in fast prototyping designed nanoparticle to examine their physical/chemical properties. Several schemes have been established for generating CS-NPs with laser ablation in the past decade. For example, CS-NPs have been formed with laser ablation of solid embedded in liquid [48-50]. This method involves with the ablation of solid sample in liquid environment to form oxide nanoparticles [43]. Also, CS-NPs can be produced by simultaneously using resistive evaporation and laser ablation in an inert gas condensation (IGC) system [41]. In this method, IGC system is employed to produce the core and the resistive evaporation is used to form the shell. By utilizing such method, magnetic Ni/CoO CS-NPs were successfully generated. Furthermore, laser ablation in the reactive gas is also reported for the CS-NPs formation [39, 51]. With this method, the graphite encapsulated metallic particles were generated with laser ablation on solid samples in CH_4 environment. CS-NPs can also be generated from Laser Ablation of Microparticles (LAM) [47]. LAM is a process of nanoparticle formation in which microparticles in a flowing aerosol are continuously ablated by high-power laser pulses. Such method has been used in generating CdSe/ZnS and Zn/CdSe CS-NPs. For all existing laser ablation methods to generate the CS-NPs, however, have limitations in the combination of the core and the shell material and/or require a preparation of special precursors (e.g., LAM) before the experiments.

To address the issues listed above, a novel double pulse laser ablation scheme is proposed in this study which involves with a sequence of laser ablations on two closely

separated materials. The interaction of the two closely separated laser induced plasma from the two ablations with specified delay times will allow the formation of CS-NPs with desired core and shell material structures. The first laser pulse ablated the target for the core material and forms condensed nano-particles in the background gas. Before the condensed core material is carried away with background flow, a second laser ablation can be triggered to vaporize the shell material and form an additional coating on existing core particles if the core and shell material are compatible and the condensed core particles are properly mixed with the vaporized shell material. This new scheme provides several advantages such as highly flexibility in producing CS-NPs with different compositions through adjusting the materials of the two targets along with delay times between two ablations in the experiments. In addition, due to the extremely fast cooling of the laser induced plasma (>~10,000 K/s) compared with other methods, particles with metastable core/shell structures have potentially to be generated with this new scheme.

To validate the proposed new scheme, designed double pulse laser ablation with a variety of material combinations of CS-NPs were conducted. The designed experiments include a verification of the contribution of (1) surface tensions of the core and shell material, (2) Gibbs free energy of the CS-NPs if they are formed, (3) contribution of background gases (He and Ar), (4) contribution of delay time between two lasers pulses (1, 8 ms), and (5) contribution of laser energy, on the formation of CS-NPs with this new scheme.

2.2 Experimental Setup

2.2.1. Experimental system

A schematic for the experimental setup is illustrated in figure 1. A ns optical parameter oscillator (Opotek Inc., Vibrant 355 series) operating at 355 nm with E~20 nJ and ~4-7 ns pulse width is adopted as the light source for ablating target of the core material. A 193 nm and ~4 ns pulse width ArF excimer laser (GAM Laser Inc., EX5/200-104) is applied as the light source for the ablation of the shell material. Ablations are conducted in the cubic cage (75mm×75mm×75mm) with two laser windows and two imaging windows. The first target (for the formation of core) and the second target (for the formation of shell) are placed perpendicularly with respect to each other at the center of the chamber (figure 2). Note that the location between two samples is confirmed with the range within two plumes overlapped as shown in figure 2(c). An Intensified Charge-Coupled Device (ICCD) system with 1024 × 1024 pixels resolution (Andor, I-Star, 734 GEN series) is utilized to capture plasma emission images through the camera lens. The time delays between the excimer laser and the tunable laser are controlled with a delay generator (BNC, MODEL 575 Pulse/delay generator) as shown in figure 1. The delay generator provides ps precisions to trigger the second laser at a specified delay time with respect to the first laser. The accuracy of the delay generator is monitored with a 500MHz oscilloscope and high response photodiodes detecting the lasing of the first and the second laser.

Two types of background gases, He and Ar, are utilized to the ablation chamber with specified flow rate controlled with a mass flow controller (MFC). The generated NPs are collected with TEM grid with thin carbon membrane (Electron Microscopy Sciences, CF200-Au, CF200-Cu) placed to the outlet gas channel for the background gas. In the present study, Sn (Goodfellow Inc., wire, 1.0mm diameter, 99.99+% purity), Zn (Goodfellow Inc., wire, 1.0mm diameter, 99.99+% purity), Si (Addisonengineering Inc.,

wafer, diameter 125 mm, N-type, orientation <100>), and Cu (Goodfellow Inc., rod, 2.0mm diameter, 99.99+% purity) are selected as the targets for the double pulsed laser ablation to generate CS-NPs. The collected CS-NPs are examined with scanning electron microscope (SEM, FEI Quanta 600 FE-SEM) to determine the particle size and shape distribution. Also, high resolution transmitted electron microscope (HRTEM, FEI Tecnai G2 F20 FE-TEM) and energy dispersive X-ray spectroscopy (EDS, PGT EDS System) are applied to determine the structure of CS-NPs along with their chemical composition.

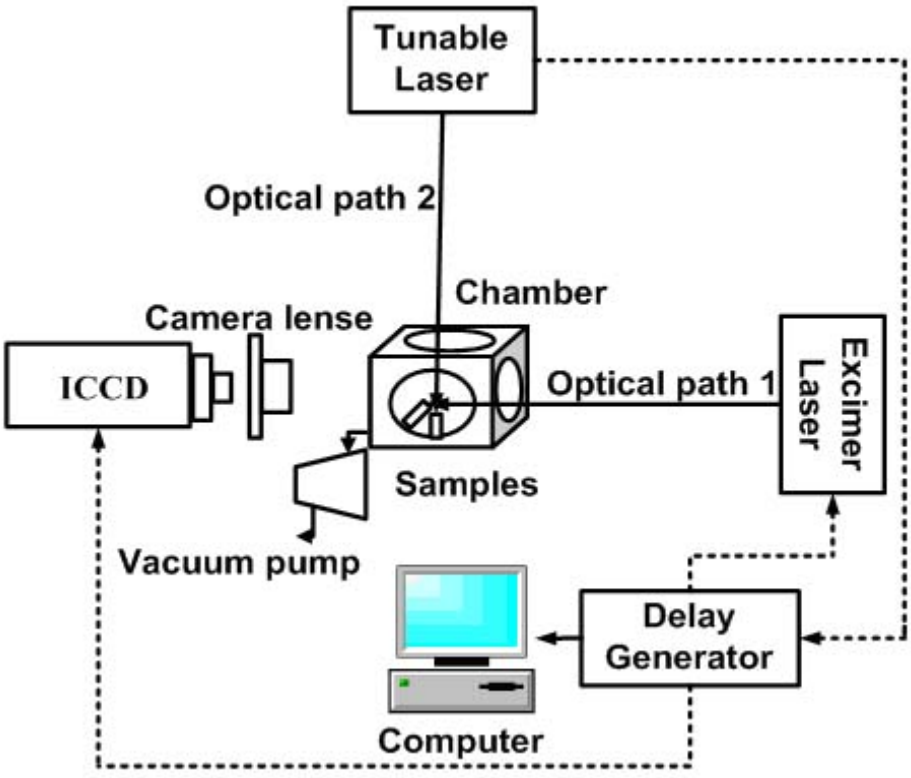

Figure 1. Schematic of the experimental setup for generating CS-NPs with double pulse laser ablation

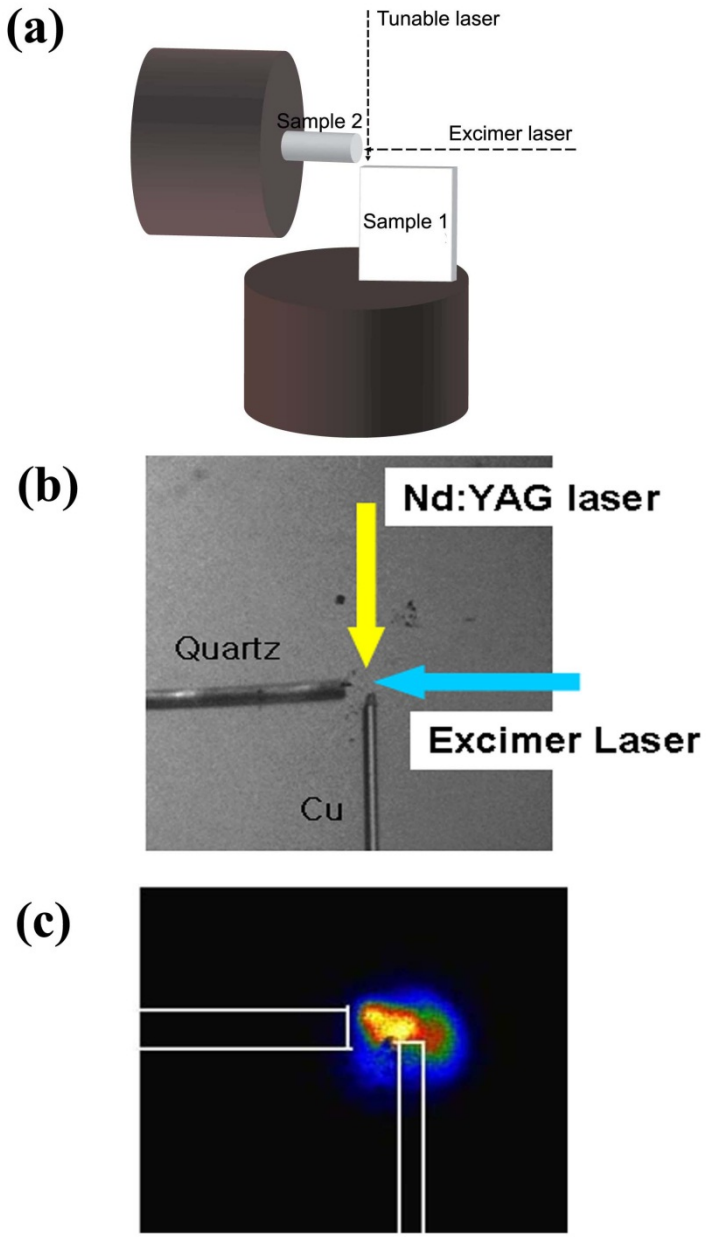

Figure 2. (a) Schematic of the sample alignment with double pulse laser ablation (b) Captured ICCD real time image to adjust the sample location (c) Thermal emission image of two ablated plumes to confirm the plume overlap

2.2.2. Observation of particles generation with the single pulse laser ablation

In order to find the appropriate delay time between two laser pulses during the double pulse laser ablation to successfully generate CS-NPs, in-situ particle formation from the single pulse laser ablation is examined. It has been reported in the previous studies that laser ablation in ambient gas provides the significant nanoparticle condensation at 100'~1000' μs after the laser pulse because temperature of the vapor plume is lower than the boiling temperature of vapor materials during this time interval [52-57].

To verify the onset time of in-situ particle generation with our laser conditions, two imaging techniques are applied. One is the thermal emission imaging to capture the early stage of laser induced vapor plume. The other is the laser induced luminescence imaging to capture the nanoparticles generated from the condensation and nucleation stage. These are illustrated in figure 3 (a) and (b), respectively. E~100 mJ of Nd:YAG laser with 532 nm is utilized for Sn ablation. A ns optical parameter oscillator operating at 355 nm tunable laser is applied as the probe beam. The delay time between the Nd:YAG laser and ICCD is presented in figure 4. The excitation wavelength applied is 497.97 nm referred from NIST atomic spectra database of Sn [58]. In order to avoid the scattering light from the probe beam and other particles, 100 nm of ICCD delay time is applied.

Figure 3(a) shows the in-situ thermal emission images of the laser induced Sn vapor plume. At the beginning of laser ablation (~few ns), hot Sn plasma plume is generated and expands into the background (He). The plume keeps losing its energy during expansion. The plume emission is unable to be captured about 3 μs after the laser pulse when the plasma temperature is too low and condensation is about to happen. Figure 3(b) shows the laser induced luminescence images of generated Sn nanoparticles after temperature drop. At ~300 μs after laser ablation, significant Sn vapor condensation happens and nanoparticles are formed and provides detectable laser induced luminescence during the imaging. The condensed particles keep grows in the following

hundred μs and provides stronger and stronger luminescence during the imaging. The strong laser induced luminescence signal from t>~500 μs suggest that at least few hundreds μs delay time will be required to obtain large enough nanoparticles from the single pulse laser ablation under our experimental conditions.

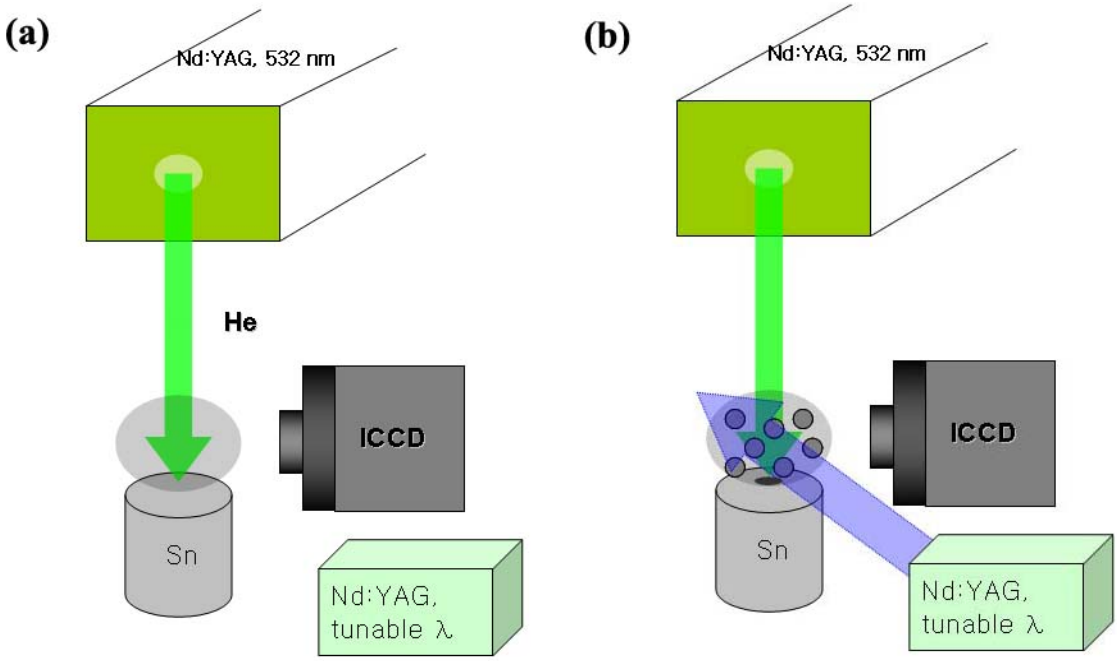

Figure 3. (a) Schematic of the thermal emission imaging. ICCD captures thermal emissions from the laser induced plasma plume (b) Schematic of laser induced luminescence imaging. Generated Sn nanoparticles from the condensed vapor plume are captured by probe laser induced luminescence light

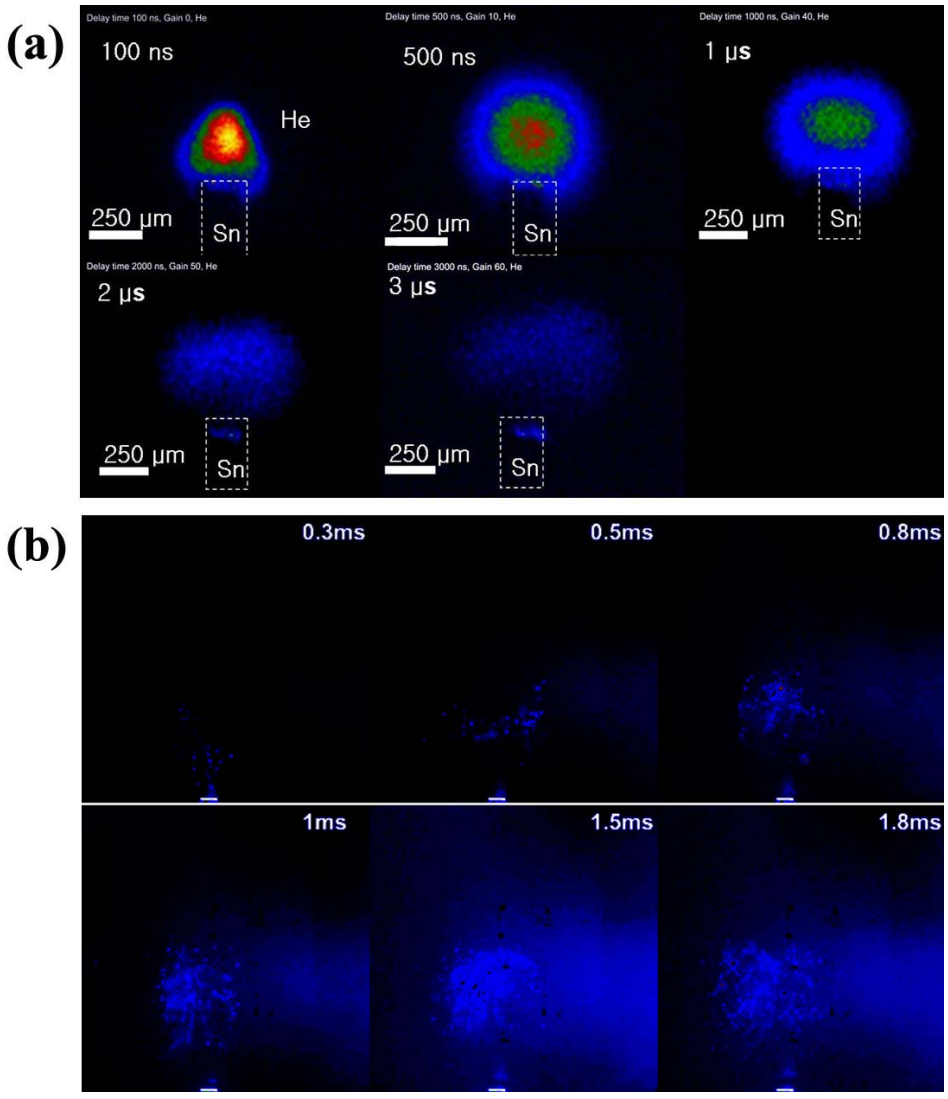

Figure 4. (a) In-situ thermal emission images of the laser induced Sn plume. Sn vapor plume is losing its thermal energy during the expansion. (b) Laser induced luminescence images of the generated Sn nanoparticles from the condenbation of the Sn vapor plume. Sn nanoparticles are significantly observed ~300µs after the laser pulse in the current experimental conditions. (Brightness and contrast are adjusted)

2.2.3. Description of double pulse laser ablation

As presented in figure 4, significant nanoparticles are formed from few 100' μs after the laser pulse. Double pulse laser ablation involves the idea that coating of existing nanoparticles can be made with another laser ablation as shown in figure 5(a). It is expected that if another laser ablation is applied after particles formation from the first laser ablation, those pre-existing particles from the first laser ablation can be coated by condensation of second laser induced vapor. Illustration of the setup of the double pulse laser ablation is in figure 5(b). In this setup, Nd:YAG laser is triggered first to generate the core NPs from sample 1, and then excimer laser is triggered to produce the shell from sample 2. It is critical to use the proper delay time between two lasers in order to obtain the CS-NPs formation. In the present study, 1ms is applied because numerous large core particles exist at this moment based on figure 4.

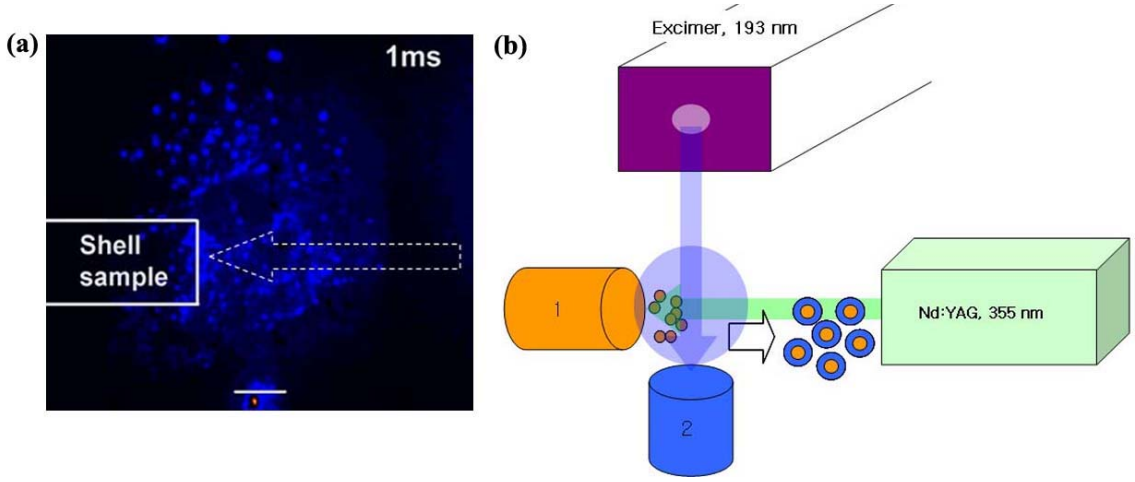

Figure 5. Schematics of double pulse laser ablation. (a) Idea of shell generation on the existing nanoparticles from the first laser ablation, and (b) illustration of double pulse laser ablation in the current study

2.3 Results and Discussion

Under all the laser energy and background conditions examined in this study, CS-NPs are successfully generated under certain conditions (e.g., Sn/glass in Ar and Zn/Si in Ar) but not others (e.g., Glass/Sn in Ar and Si/Ge in Ar). To identify the dominating parameters on the formation of CS-NPs with the proposed double pulse laser scheme, formation of CS-NPs with different (a) surface tension of core and shell materials, (b) delay time between the two lasers, (c) background gas type, (d) laser energy for ablating the core material are examined. These four parameters were determined to be important in previous single component NP generation with laser ablation [53]. The result of each set of experiment is presented and discussed as follows.

2.3.1 Effect of surface tension

From the previous studies, generating nanoparticles from laser ablation can be attributed to a sequence of phase change processes including solid material boiling, evaporation and nucleation into nanomaterials [59-61]. A major difference between the single element nanoparticle generation and the CS-NPs generation is mainly on the additional interface between the core and the shell materials during the particle formation, which is not presented in single element laser ablation. It is expected that the ease of the formation of the specified CS-NPs should be a function of intermolecular forces within the core, shell and interfaces of CS-NPs. The surface tension between the core and the vapor of the shell material should be larger than combination of the surface tension of shell vapor and the interfacial tension between the core and shell to proper cover of the entire core (solid or liquid) with the liquid shell under the thermal equilibrium condition [62-65]. This statement is valid for the condensation of liquid shell on either solid or liquid cores under local thermal equilibrium conditions [62]. In the present study, Si, Zn, Ge, Sn, and Glass with different surface tensions were selected as the ablation targets to first identify the possibility of formation of CS-NPs under high surface tension core/low

surface tension shell (high/low) and low surface tension core and high surface tension shell (low/high) combinations. The properties of examined materials are listed in table 1.

Table 1. Thermal properties and surface tensions of target materials examined in this study

	Cu	**Zn**	**Sn**	**Si**	**Ge**	**Glass**
Melting point (K)	1357.77	692.68	505.08	1687	1211	1920
Boiling point (K)	2835	1180	2875	3538	3106	2470
Surface tension at melting point (mJ/m^2)	1355	789	560	865	621	100

(a) Case 1: Zn/glass CS-NP (high/low combination)

To study the possibility of the generating CS-NPs with core material with higher surface tension and shell material with lower surface tension, Zn core and glass shell combination were examined in the case 1 study. Zn has higher surface tension coefficient (~790 N/m) than glass (~100 N/m) at high temperature (i.e., >670 K). Zn is ablated as the core material with the tunable laser ablation (Nd:YAG, 355 nm), and glass (SiO_2) is applied as the shell material with excimer laser ablation (EX5/200-104, 193 nm). Both materials have strong absorption spectra and low ablation threshold within the specified wavelengths and can result in efficient laser ablation. CS-NPs are successfully generated under this condition. Figure 6(a), (c) show the High-Resolution Transmission Electron Microscope (HRTEM) images of Zn/glass CS structure. Core diameter is measured ~12 nm, and the shell thickness ranged from 3.5~4nm. Due to higher atomic weight in Zn, the electron scattering cross section is larger, and the contrast of Zn is higher than glass (SiO_2). To verify the compositions of core and shell region, ~1nm size

Energy Dispersive Spectroscopy (EDS) probe beam is applied throughout the CS-NP. The EDS line scanning result is presented in figure 6 (b) and (d). The beam path is indicated as a red line on the HRTEM image. The maximum Zn signal is shown at the center of particle, and the maximum SiO_2 signal is shown at the edge of particle, which is an evidence of the formation of Zn/glass CS-NPs under the examined condition.

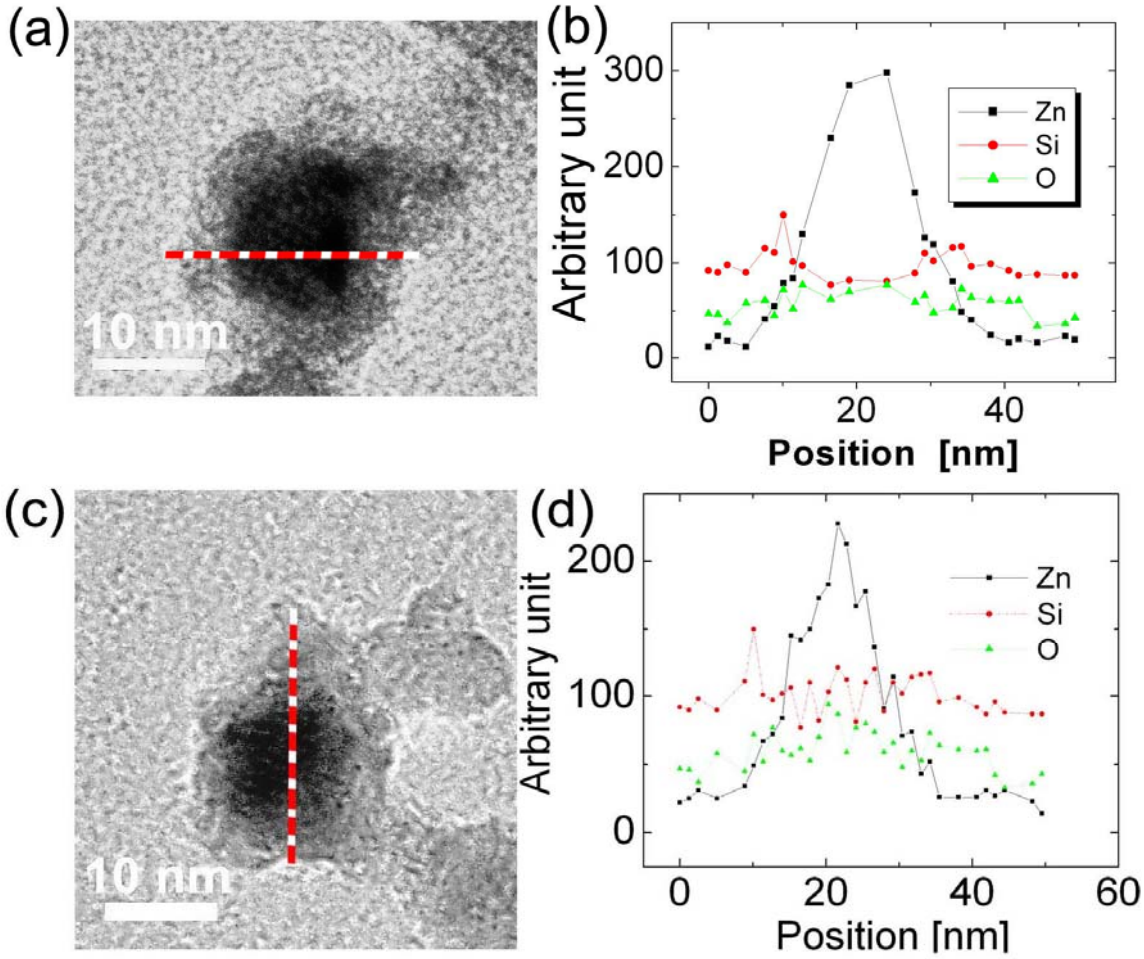

Figure 6. Zn/glass CS-NP. (a), (c) HRTEM image of Zn/glass CS-NP. The Zn region is darker than the glass (SiO_2) region due to its higher atomic weight, (b), (d) EDS line profile of Zn/glass CS-NP. The maximum Zn signal appears at the center of particle, and the maximum SiO_2 signal appears at the edge of particle, which suggests a Zn/glass CS structure. The red line shows the EDS beam path.

(b) Case 2: Sn/glass CS-NP (high/low combination)

Sn/glass CS, is tested as another high/low core/shell combination to verify the formation of CS-NPs under such combination. Sn has higher surface tension coefficient (~560 N/m) than glass (~100 N/m) in its melting temperature. Detail experimental conditions such as laser energy, background gas type, and gas flow rate are presented in table 2. Similar to the results from Case 1, figure 7(a) shows HRTEM image of the collected NPs. Core diameter is measured ~10 nm, and the shell thickness ranged from 5~7 nm. Due to higher atomic weight, Sn is darker than Glass. EDS line profile is presented in figure 7(b). The beam path is indicated as a red line on the HRTEM image. From the EDS provided, since Si and O show the same trend compared with Sn, it is expected that the formed nanoparticle contains SiOx and Sn rather than a simple mixture of Sn-Si-O. Since Sn has a peak at the center compared SiOx has a peak at the shell, it is expected that the generated CS-NP is a Sn core and SiOx shell particle. The broadening of the Sn signal to the shell region can be understood by the electron beam broadening due to the presence of interface between heavier core and lighter shell material in the Sn/SiO_2 combination. Sn has a significant higher atomic weight compared with the shell material [66]. Based on a quantitative formula provided in reference [66], the broadening of the Sn in EDS can be ~15 nm, which is comparable to the generated shell thickness in this experimental condition.

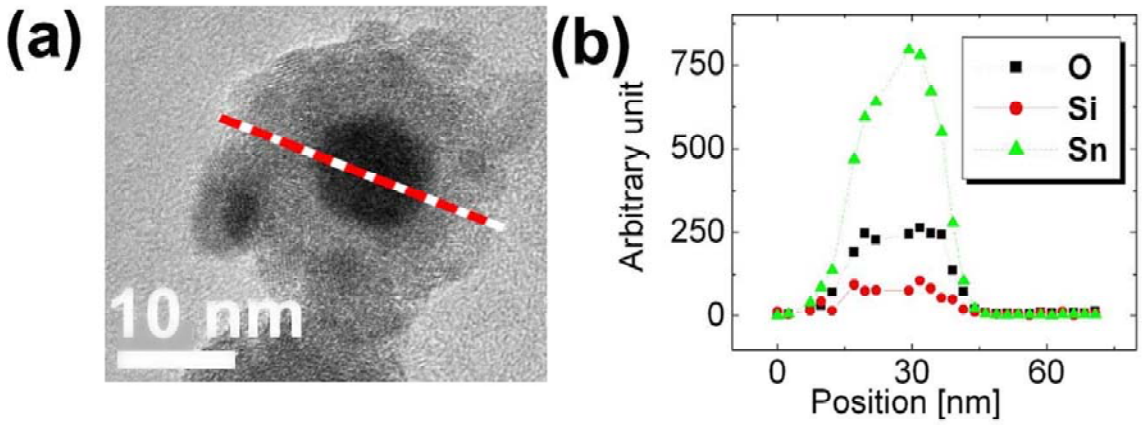

Figure 7. Sn/glass CS-NP. (a) HRTEM image of a Sn/glass CS-NP. The Sn region is darker than the glass (SiO_2) region in the HDRTEM images due to its higher atomic weight, (b) EDS line profile of the Sn/glass CS-NP. The maximum Sn signal appears at the center of particles, and the maximum SiO_2 signal appears at the edge of particle, which suggests a Zn/glass CS structure. The red line shows the EDS beam path

Table 2. Experimental conditions for the effect of surface/interfacial energy, background gas, delay time, and laser energy.

	Surface/interfacial energy effect				**Background gas effect**		**Delay time effect**		**Laser energy effect**	
Type of CS-NPs designed	**Zn/Glass**	**Sn/Glass**	**Zn/Si**	**Ge/Si**	**Cu/Zn**	**Sn/Si**	**Cu/Zn**	**Sn/Si**	**Cu/Zn**	**Sn/Si**
First laser (Core)	Tunable Nd:YAG (355 nm, 20mJ)	Tunable Nd:YAG (355 nm, 20 mJ)	Tunable Nd:YAG (355 nm, 20mJ)	Tunable Nd:YAG (355 nm, 20mJ)	Tunable Nd:YAG (355 nm, 20 mJ)	Tunable Nd:YAG (355 nm, 20 mJ)	Tunable Nd:YAG (355 nm, 20 mJ)	Tunable Nd:YAG (355 nm, 20 mJ)	Tunable Nd:YAG (355 nm, 8,31 mJ)	Tunable Nd:YAG (355 nm, 8,31 mJ)
Second laser (Shell)	Excimer (193 nm, 9mJ)	Excimer (193 nm, 9mJ)	Excimer (193 nm, 9mJ)	Excimer (193 nm, 9mJ)	Excimer (193 nm, 9mJ)	Excimer (193 nm, 9mJ)	Excimer (193 nm, 9mJ)	Excimer (193 nm, 9mJ)	Excimer (193 nm, 9mJ)	Excimer (193 nm, 9mJ)
Gas type	Ar	Ar	Ar	Ar	Ar, He	Ar, He	Ar	Ar	Ar	Ar
flow rate (Standard liter per meter, SLPM)	3	3	3	3	3	3	3	3	3	3
Core material	Zn	Sn	Zn	Ge	Cu	Sn	Cu	Sn	Cu	Sn
Shell material	Glass	Glass	Si	Si	Zn	Si	Zn	Si	Zn	Si
Delay time (ms)	1	1	1	1	1	1	1, 8	1, 8	1	1

(c) Case 3: Zn/Si CS-NP (low/high combination)

In this portion of study, the possibility of formation of CS-NPs with the low/high core/shell surface tension materials is examined. Zn core and Si shell combination which has low and high surface tension coefficients respectively (Zn:~789 N/m, Si: ~865 N/m) is carried out in this portion of study. Detailed experimental conditions are presented in table 2. From the HRTEM images obtained after the experiment, Si

covered Zn particle is observed in figure 8(a). Zn is darker than Si due to its atomic weight difference. The shell thickness is around 2~4nm. EDS line profile is presented in figure 8(b). The beam path is indicated as a red line on the HRTEM image. The center region shows strong Zn signal while edge region shows strong Si signal, which is an evidence of the formation of Zn/Si CS-NPs under the examined condition.

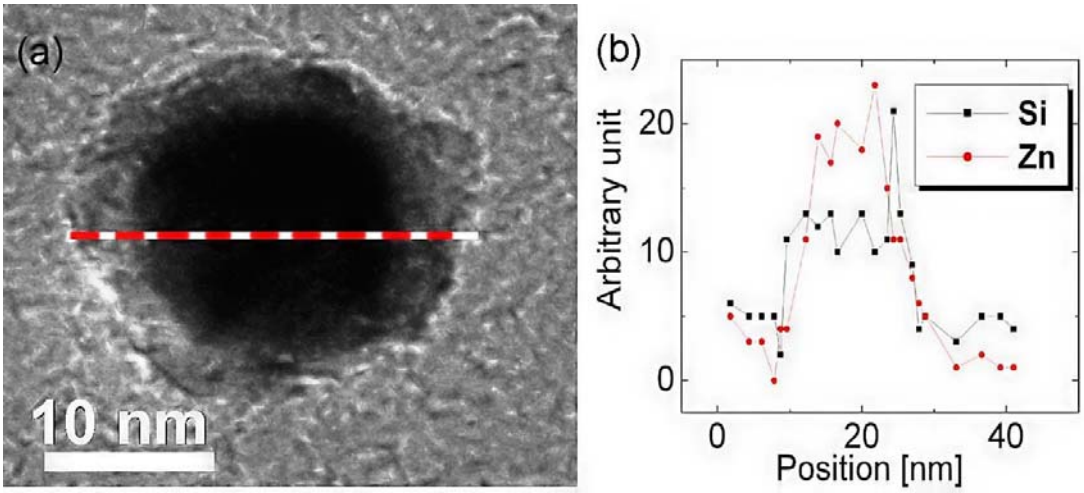

Figure 8. Zn/Si CS-NP. (a) HRTEM image of a common Zn/Si CS-NP from the experiment. Zn region is darker than Si region in the HRTEM image due to higher atomic weight, (b) EDS line profile of Zn/Si CS-NP. The maximum Zn signal appears at the center of particle, and the maximum Si signal appears at the edge of particle, which suggests a Zn/Si CS structure. The red line shows the EDS beam path.

(d) Case 4: Ge/Si CS-NP (low/high combination)

Ge/Si CS-NPs is examined as another material combination for the low surface tension core and high surface tension shell (Ge: ~621 N/m, Si: ~865 N/m). Detail experimental conditions are also presented in table 2. From the HRTEM images, Si covered Ge particle is observed in figure 6(a) (Ge is darker than Si in the TEM image due to its higher atomic weight). However the Si shell is not smooth and does not entirely cover the Ge core. EDS line profile is measured throughout the core shell region as shown in figure 9(b). The beam path is indicated as a red line on the HRTEM image. The center region which is black sphere on figure 9(a) shows strong Ge signal, and the edge region

shows strong Si signal, which is an evidence of the formation of Ge/Si CS-NPs under the examined condition.

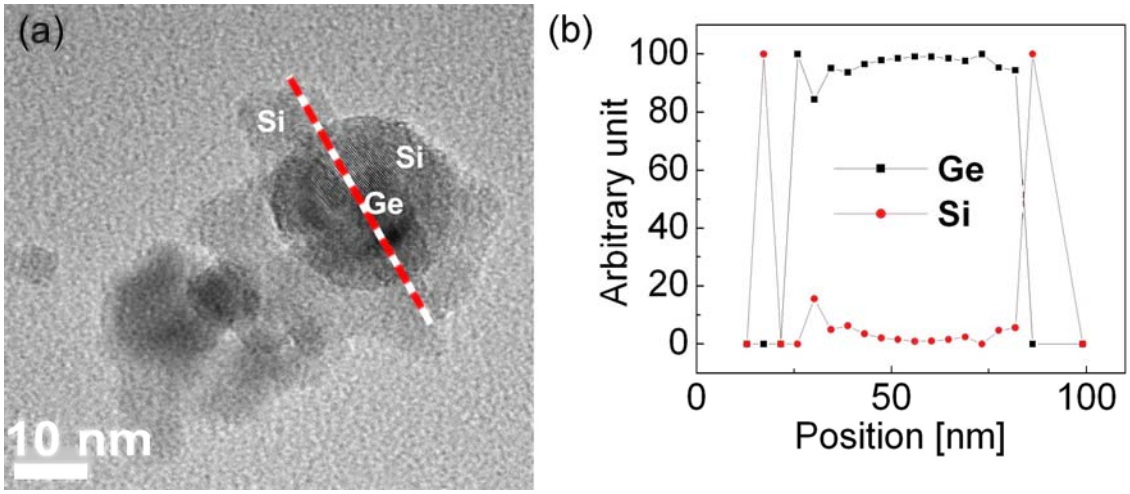

Figure 9. Ge/Si CS-NP. (a) HRTEM image of Ge/Si CS-NP. The Ge region is darker than the Si region due to its higher atomic weight, (b) EDS line profile of Ge/Si CS-NP. The strong Ge signal appears at the center of particle, and the SiO_2 signal appears at the edge of particle, which suggests a Ge/Si CS structure. The red line shows the EDS beam path.

Based on the result of the above four cases, the possibility of formation of CS-NPs with the new scheme is not simply determined by the surface tension relation between the core and the shell material. CS-NPs can be generated from the core/shell combination with either low surface tensions core/high surface tension shell or high surface tension core/low surface tension shell combinations. To identify the role of surface tension on the formation of CS-NPs, the Gibbs free energy analysis for a CS-NPs is conducted as follows: when the condensed core particles are mixed with the vapor of the designed shell material from the second laser ablation, the vaporized shell material will either coat on existing core particles to form CS-NPs through heterogeneous nucleation, or will form separate NPs with respect to the core particles from the homogeneous nucleation. In order to obtain a large number of CS-NPs rather than separated particles with either the core material or the shell material, the Gibbs free energy for the formation of CS-NPs should be lower than the Gibbs free energy for the formation of separated particles

composed with single element as illustrated in figure 10 (1). The Gibbs free energy for the formation of CS-NPs can be estimated as

$$E_{CS-NP} = -(V_C \Delta G_C + V_S \Delta G_S) + A_C \gamma_{CS} + A_{S,CS} \gamma_S \quad (2.1)$$

where V and A are the volume and surface area of particles respectively; ΔG_S is the Gibbs free energy of the bulk core or shell material; γ is the surface tension of the material. Subscripts C and S indicate the core and shell properties, respectively. γ_{CS} represents the interfacial energy between the core and the shell interface [67]. For example, the surface area of core in figure 10 (1) will be Ac, and the surface area of shell of a core/shell structure in figure 10 (2) will be $A_{S,CS}$.

The Gibbs free energy for the formation of pure element particles containing either the core element or the shell element (c.f., figure 10 (2)) can be expressed as

$$E_{Seperate\ particles} = -(V_C \Delta G_C + V_S \Delta G_S) + A_C \gamma_C + A_{S,NO-CS} \gamma_S \quad (2.2)$$

where, $A_{S,NO-CS}$, refers to the surface area of the single particle from the shell material when the amount of shell material does not coat on existing core particles but forms separated particles. For example, the surface area of the condensed particle with the shell material when it didn't form a core/shell structure, as in figure 10 (1), will be $A_{S,NO-CS}$.

The difference between E_{CS-NP} and $E_{Seperate\ particles}$, which is ΔE, can be expressed as

$$\Delta E = E_{CS-NP} - E_{Seperate\ particles} = A_C(\gamma_{CS} - \gamma_C) + \gamma_S(A_{S,CS} - A_{S,NO-CS}) \quad (2.3)$$

ΔE should be a negative number to have high possibility for the formation of CS-NPs from the double pulse laser ablation.

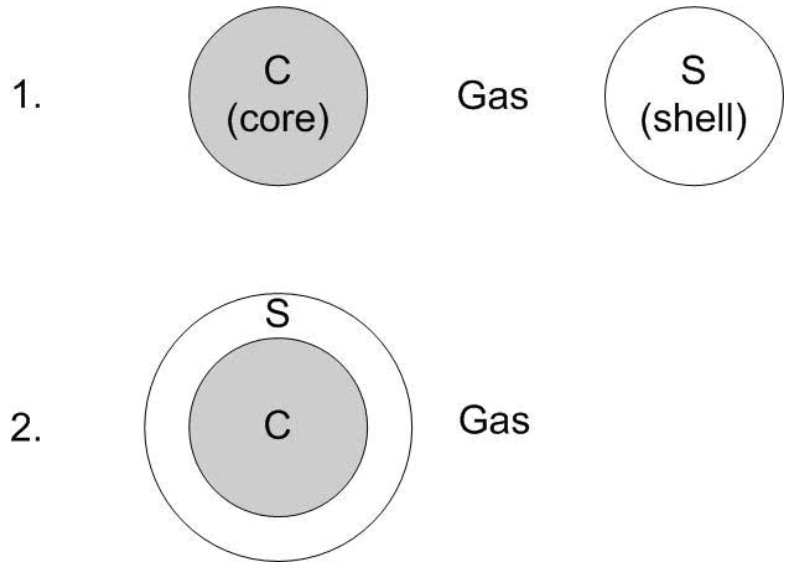

Figure 10. Schematic for the configuration of idealized NPs (1) composed with either core or shell materials (i.e., CS-NPs are not generated from the double pulse experiment), and (2) with core/shell structure (i.e., CS-NPs generated from the proposed double pulse experiment).

To examine the contribution of ΔE on the formation of CS-NPs, ΔE as function of interfacial energy, γ_{CS}, for the four material combinations presented in the last section (i.e., Sn/glass, Zn/glass, Zn/Si, Ge/Si) are plotted in figure 11. Note that CS-NPs are successfully generated under those four combinations. Also, the ΔE under corresponding inversed CS material combinations, namely, (a) Glass/Sn combinations, (b) Glass/Zn combinations, (c) Si/Zn combinations, and (d) Si/Ge combinations are illustrated in figure 11. The reversed combinations are examined by exchange the ablation sequence of the core and the target material. Note that we experimentally observe CS-NPs from only one of these revered combinations (i.e., Si/Zn), which provides the required particle size information for the calculation of the associated Gibbs free energy of the generated CS-NPs. The particle size information required for the Gibbs free energy analysis for the other three failed reversed cases are extracted from the corresponding successful original combinations (i.e., Sn/Glass, Zn/Glass, and Ge/Si) under the assumption that the change of the laser sequence does not change the ablation

behavior of the core and shell targets. Comparisons of the calculated ΔE value as function of γ_{CS} for the four original and reversed combinations are listed as follows:

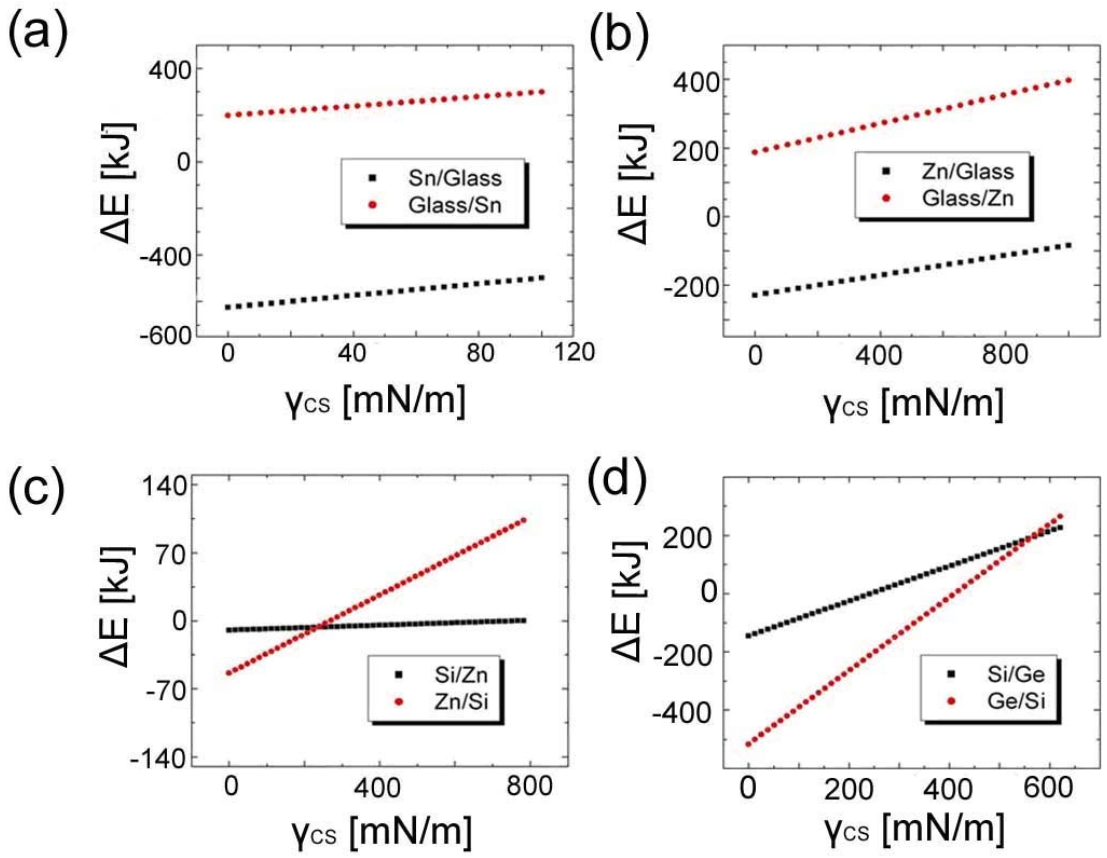

Figure 11. Contribution of interfacial energy to Gibbs' free energy difference(ΔE) between the single particle and CS-NP generation; (a) Sn/Glass and Glass/Sn CS-NPs, (b) Zn/Glass and Glass/Zn CS-NPs, (c) Si/Zn and Zn/Si CS-NPs, (d) Si/Ge and Ge/Si CS-NPs. Each square dot and circle dot represents the CS-NPs with high/low and low/high surface tension material combinations respectively. To generate the CS-NPs under thermal equilibrium conditions, ΔE should be negative.

- glass/Sn and Sn/glass: for the glass/Sn and Sn/glass combinations (figure 11(a)), ΔE is always positive for glass/Sn CS-NPs, and negative for Sn/glass CS-NPs under all kinds of interfacial energy values between these Sn and glass (note that the interfacial energy of two materials has few tabulated data and is affected by quality of the interface between the two materials. In most cases, the interfacial energy is less than the surface

tension energy of the material constructing the interface [68]). Therefore, Sn/glass CS-NP can be easily generated from double pulse laser ablation compared with glass/Sn CS-NP. This trend is consistent with the experimental observation from this study; no CS-NPs are observed in glass/Sn but in Sn/glass combination.

- glass/Zn and Zn/glass: for the Zn/glass and glass/Zn combinations (figure 11(b)), ΔE is always positive for glass/Zn CS-NPs, and negative for Zn/glass CS-NPs under all kinds of interfacial energy values between these Zn and glass. Therefore, Zn/glass CS-NPs can be easily generated from double pulse laser ablation compared with glass/Zn CS-NPs. This trend is consistent with the experimental observation from this study; no CS-NPs are observed in glass/Zn combination but in Zn/glass combination.

- Zn/Si and Si/Zn: for the Zn/Si and Si/Zn combinations (figure 11(c)), ΔE of Zn/Si CS-NP is changed from the negative value to the positive value when interfacial energy is ~230 mN/m. Since ΔE is varied a lot in terms of the interfacial energy, we estimate the interfacial energy for this specific combination (Zn/Si) based on [64], which provides an interfacial energy value ~80 mN/m. ΔE of Zn/Si CS-NP is much smaller than that of Si/Zn CS-NP around this interfacial energy value as illustrated in figure 11(c). Therefore, Zn/Si CS-NP can be easily generated compared with Si/Zn CS-NP under the laser energy studied. This trend is consistent with the experimental observation from this study: a large percentage of Zn/Si CS-NPs and very few Si/Zn CS-NPs are observed under experimental conditions studied.

- Ge/Si and Si/Ge: for the Ge/Si and Si/Ge combinations (figure 11(d)), ΔE is varied from the negative to the positive values under the different interfacial energy between Ge and Si. Therefore, the approximated interfacial energy value between Ge and Si is again estimated with the formula provided in [64], which provides a value ~ 70 mN/m. ΔE of Ge/Si CS-NP is much smaller than that of Si/Ge CS-NP around this interfacial energy as illustrated in figure 11(d). Therefore, Ge/Si CS-NP can be easily generated

compared with Si/Ge CS-NP under the laser energy studied. This trend is consistent with the experimental observation from this study; a larger percentage of Ge/Si CS-NPs but no Si/Ge CS-NPs are observed under experimental conditions studied.

As a short summary, CS-NPs can be successfully generated with the proposed two laser pulses scheme when the Gibbs free energy of the CS-NPs (if they are successfully generated) is lower than the Gibbs free energy of the separated condensed nano-paticles (i.e., the shell material does not coat on the existing core particle but forms shell nano-particles separately). The Gibbs free energy of the CS-NPs (if it is formed) is a function of the surface tension of the core and shell materials, and interfacial energy between core and shell material along with the size of the core and shell of the CS-NPs.

2.3.2 Effect of background gas

Based on the previous studies, particles condensation process from vaporized material of laser ablation is a strong function of the background gas. The differences in the thermal conductivity along with the density and viscosity of different background gases can result in a change of the thermal/flow fields and condensation process of nano-particle generated from laser ablation [55-57]. To identify the contribution of the background gas in the size, shape and composition of CS-NPs from the proposed double pulse laser ablation scheme, two background gases, namely, He and Ar (each thermal conductivities are 142.64 mW/m·K and 12.36 mW/m·K, respectively) are examined [56-57]. Cu/Zn and Sn/Si CS-NPs are chosen as the two combinations in this section considering the ease of generating CS-NP compared with other combinations studied in this research. Also, the single component NP from Cu and Si under different background gases have been well examined in the previous study which can provide a good comparison to this portion of work [53]. The detail experimental conditions for the background gas test are listed in table 2. The TEM images of the generated CS-NPs are presented in figure 12 ~ 15. The sizes of nano-particles generated in He for both combinations are smaller (3~10 nm) than that in Ar (20~30 nm) (figure 12 and 13). This trend is the same as nano-

particle generation from single pulse laser ablation [53]. In addition, more agglomerated particles and larger agglomerated structures are observed in He compared with that in Ar. Note that size of the agglomeration structure is inversely proportional to the size of composing NPs [69]. The stronger agglomerated structures appear commonly with smaller generated NP due to the larger accompanied Van der Waals force and electrostatic force when the NP size is reduced [53]. (see figure 14 and 15) More importantly, the particles in the particle chain in Ar are mostly Cu/Zn CS-NPs. One the other hand, the CS-NPs are lack in the agglomerated structures in He. The lack of CS structure in each agglomerate in He can be attributed to the much higher cooling rate of vaporized material in He and the associated smaller condensed core particles from the first laser ablation. These much smaller core particles from the first laser ablation in He can be digested with the laser induced plasma from the second laser ablation on the shell material, which prevents the formation of CS-NPs for double pulse laser ablation in He. In addition, the smaller core increase the value of Gibbs free energy of the CS-NPs if they are generated (equation 2.3), which impedes the formation of CS-NPs from these small cores in He compared with those big core generated from ablation in Ar based on the Gibbs free energy analysis as in the last section.

As a short summary, the selection of background gas can change the configuration of condensed particles from double pulse laser ablation. Background gas with lower thermal conductivity (e.g., Ar) results in larger core particles from the first laser ablation and have higher chance to form CS-NPs compared with the experiments conducted in He with higher thermal conductivity.

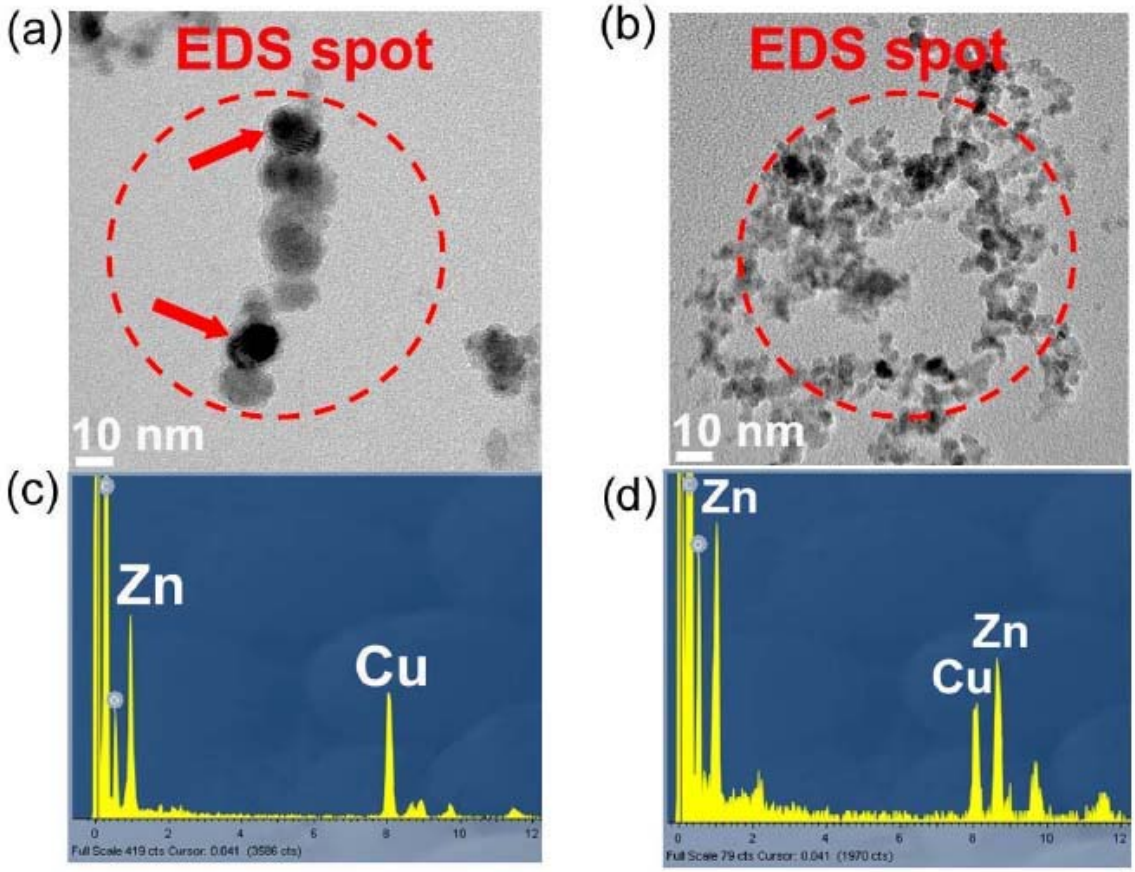

Figure 12. Cu/Zn particles generated in Ar and He. (a) HRTEM image of Cu/Zn particles in Ar. (b) HRTEM image of Cu/Zn particles in He. (c) EDS of particles group in Ar, and (d) EDS of particles group in He. Particle in Ar are larger (20~30 nm) than that in He (3~10 nm). Also, less agglomerations are observed in Ar than that in He. Through both Cu and Zn signals are observed in agglomerated particle from the experiments in Ar and He, CS-NP structures are only observed in the constructing particles of the agglomerations in Ar but not that in He. (Red arrow shows CS-NP)

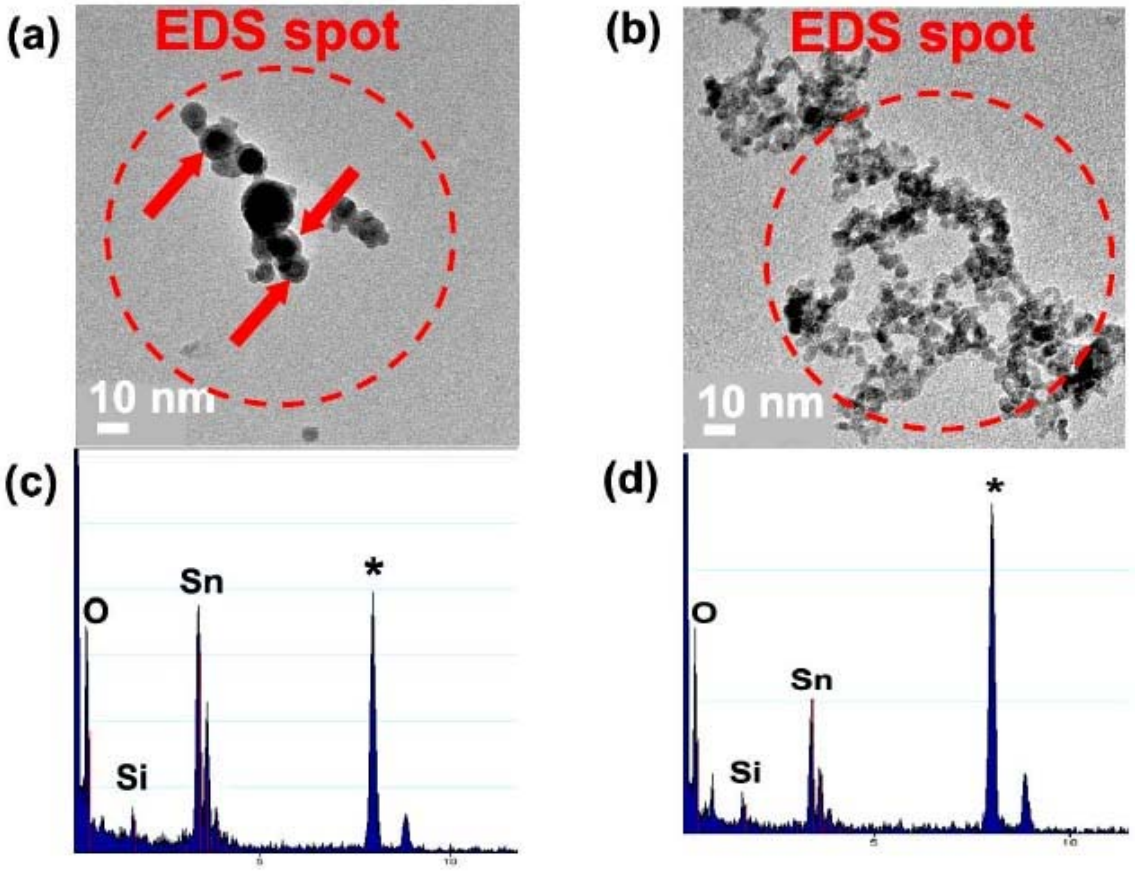

Figure 13. Sn/glass particles in Ar and He. (a) HRTEM images of Sn/glass in Ar. (b) HRTEM image of Sn/glass particles in He. CS structures are observed in Ar but not in He. (c) EDS of agglomerations in Ar. Both Sn and SiO_2 signals appear in EDS suggests a Sn/glass core/shell structure for the CS-NPs imaged. (d) EDS of the entire particle chain in He. Though Sn/SiO_2 CS-NPs are not observed from the experiment in He, both Sn and Si signals appear in the particle agglomeration. (Red arrow shows CS-NPs)

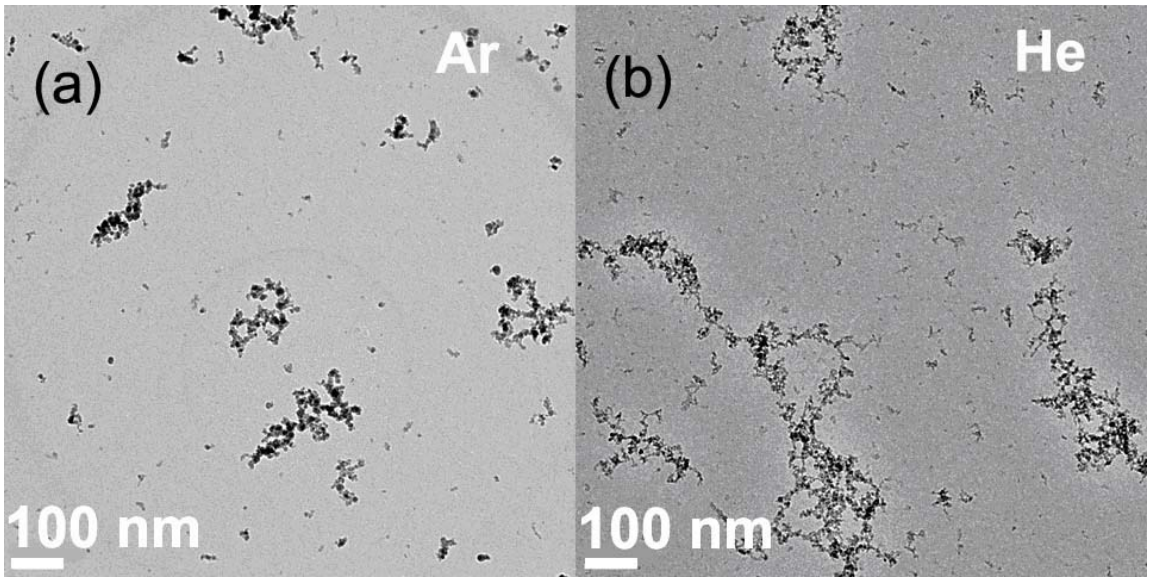

Figure 14. Low magnification HRTEM images of Cu/Zn NPs in (a) Ar and (b) He, respectively. More agglomerations and longer agglomerated chains are observed in He than that in Ar.

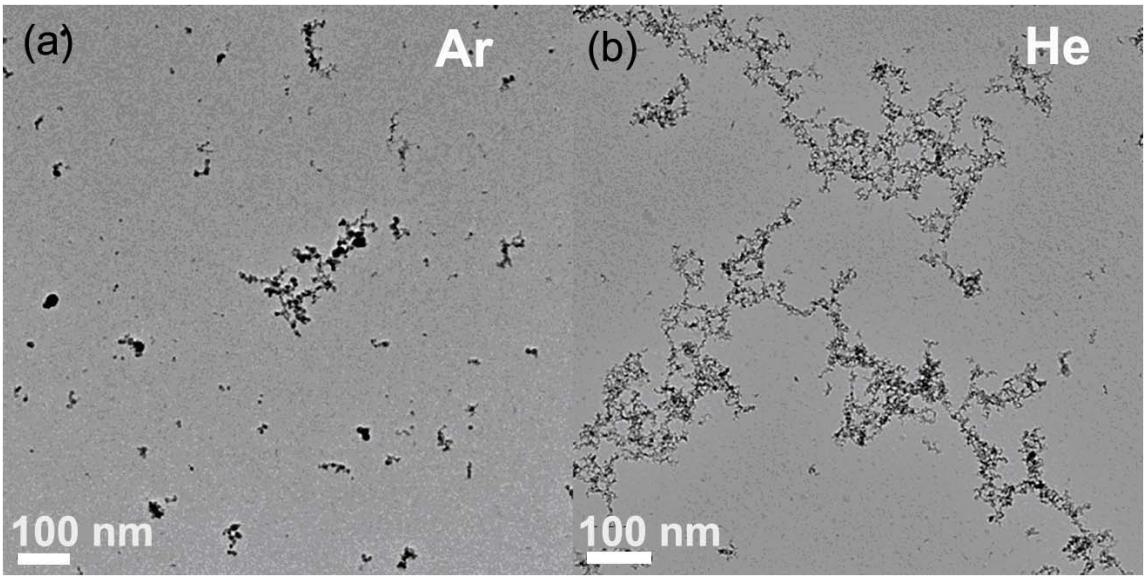

Figure 15. Low magnification HRTEM images of Sn/glass CS-NPs in (a) Ar and (b) He, respectively. Compared with the experiments in Ar, more agglomerations are observed for experiments in He than that in Ar. In addition, longer agglomerated chains are observed for experiments in He.

2.3.3 Effect of delay time between two lasers

In this portion of study, delay time between two laser pulses is examined to identify the contribution of the delay time on the formation of CS-NPs compared with other controllable physical parameters. Ar is selected as the background gas due to the ease of forming CS-NPs as discussed in the last section. As described in chapter 2.3, particles condensation occurs from ~300 μs to ~a few ms after laser pulse for ablation in He. Also, particles agglomeration and growth are observed in the further delay times (few ms). Therefore, the delay time between the two laser pulses should be comparable or longer than ~300 μs to ~a few ms to fully condense core particles from the first laser pulse. However, it is a question whether or not a much longer delay time (>a few ms) between two laser pulses can benefit the generation of CS-NPs with new scheme proposed in this study because agglomerated big particles group are getting dispersed or diffused into background. To answer this question, two different delay times, namely, 1ms and 8ms, are tested to characterize the formation of CS-NPs from the proposed double laser pulse scheme. The results for Cu/Zn and Sn/glass combinations are presented in figure 16 to 19. It is found that both core and shell materials are detected in all the agglomerations for both compositions studied when the delay time is equal to 1 ms. Furthermore, the agglomerations are composed with many CS-NPs under this shorter delay time. On the other hand, most of particles and agglomerations obtained from experiments with 8 ms delay time are composed of the single element (i.e., either with the core or the shell material). No CS-NPs are observed under this longer delay time. The poor generation of CS-NPs under longer delay time between two laser pulses can be attributed to the fluid dynamics (i.e., velocity field) of the particle plume after it is generated. It was observed in previous study that the condensed particle plume can move far away from the ablation site >10's ms after the laser pulse [53]. This dynamics of condensed particle plume from the first laser pulse can result in poor mixing the condensed core particle and the vaporized shell material from the second laser pulse when the delay time becomes longer.

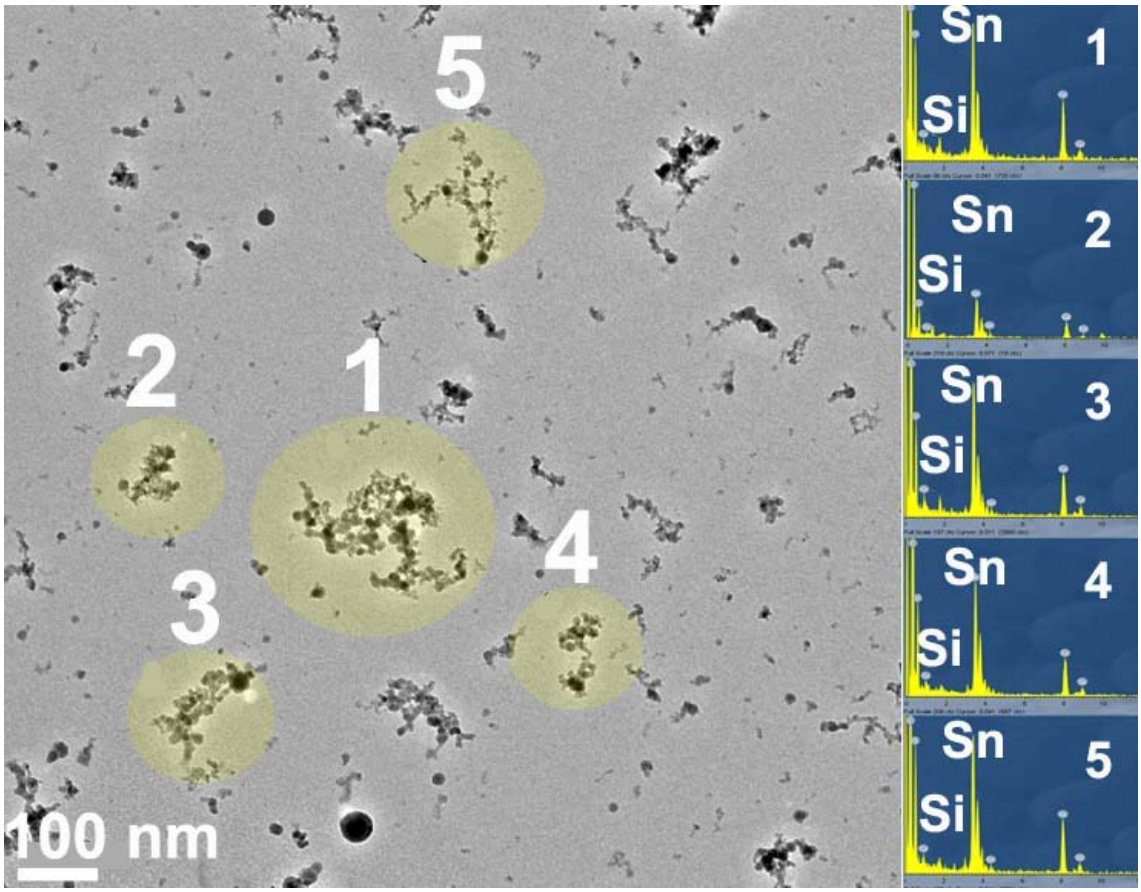

Figure 16. HRTEM image of Sn/glass CS-NPs when 1ms delay time is applied between two laser pulses. EDS is applied throughout the random particle group 1 to 5. All particle groups examined are composed mainly with Sn and SiO_2 together based on the corresponding EDS measurements.

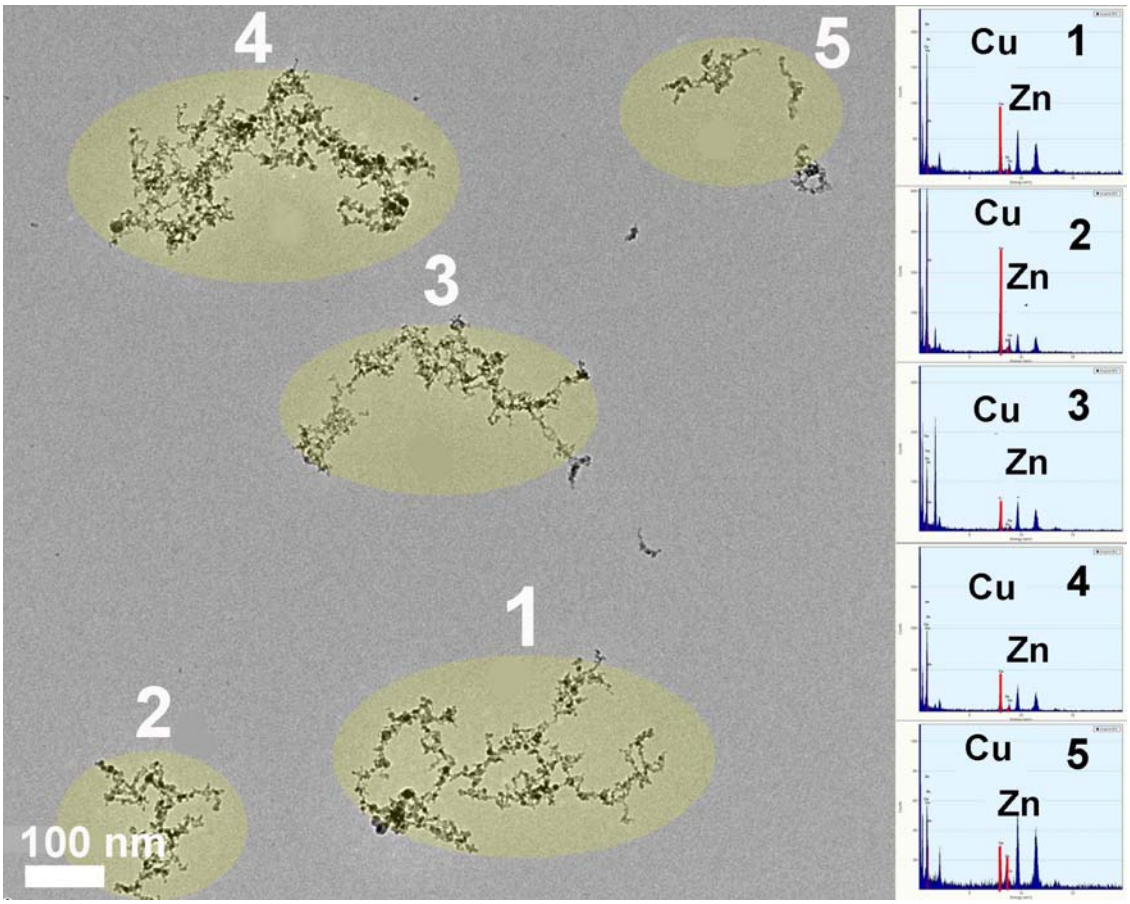

Figure 17. HRTEM image of Cu/Zn CS-NPs when 1ms delay time is applied between two laser pulses. EDS is applied throughout the random particle group 1 to 5. All particle groups examined are composed mainly with Cu and Zn together based on the corresponding EDS measurements**.**

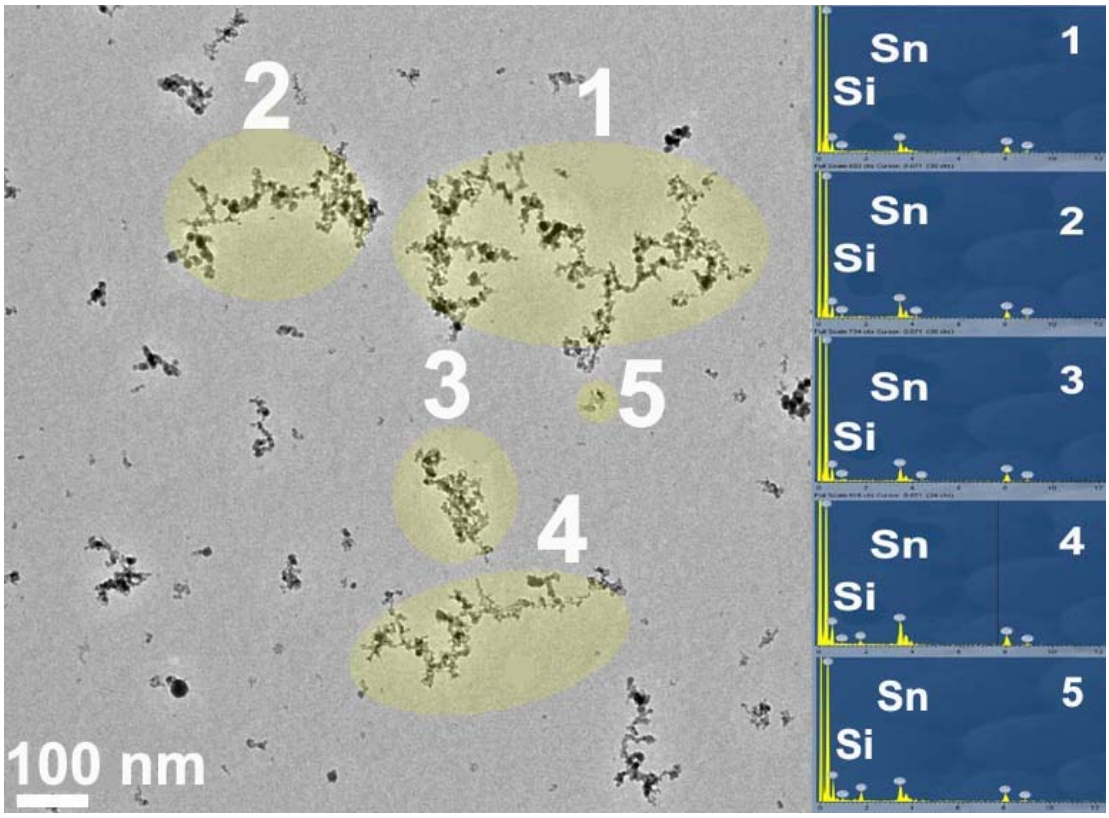

Figure 18. HRTEM image of Sn/glass CS-NPs when 8ms delay time is applied between two laser pulses. EDS is applied throughout the random particle group 1 to 5. It is found that only group 4 and 5 have both Sn and SiO_2. Group 1 to 3 are composed mainly with Sn based on the corresponding EDS measurements.

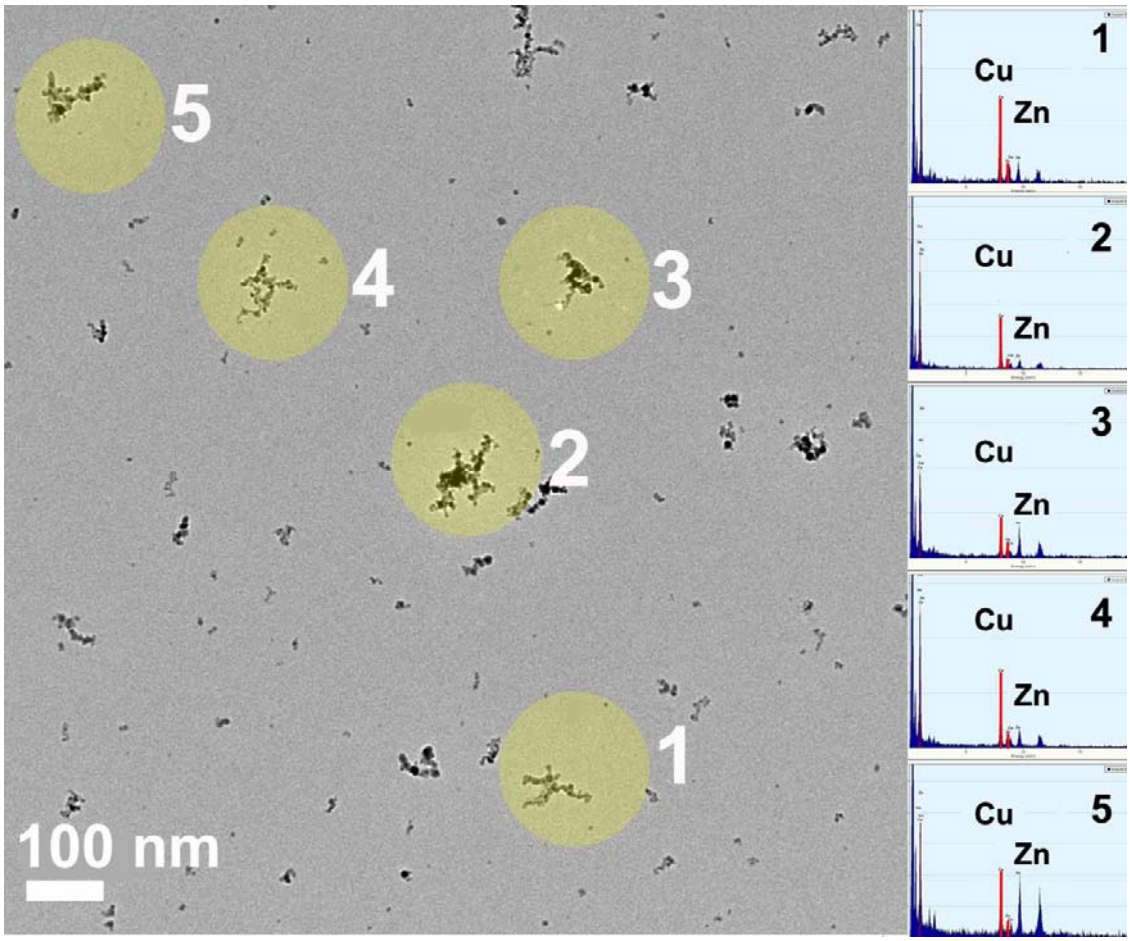

Figure 19. HRTEM image of Cu/Zn CS-NPs when 8ms delay time is applied between two laser pulses. EDS is applied throughout the random particle group 1 to 5. It is found that only group 5 has both Cu and Zn signals. Group 1 to 4 has only Cu signal based on the corresponding EDS.

2.3.4 Effect of laser energy

Laser energy is another important factor which can affect the configuration of the CS-NPs from the laser ablation. Larger nanoparticles can be generated from higher laser energy ablation due to large amount of mass removed from the target and the associated longer condensation process [55-57]. Note that the large core particles increase the possibility of the formation of CS-NPs based on the Gibbs free energy analysis in section (a). Therefore, it is expected that CS-NPs can be generated more easily when the

laser energy applied to the core material is increased. To verify this assumption, two different laser energies (8mJ, 31mJ) are examined for the ablation of core materials. In this controlled experiment, the laser energy for ablating the shell material was remained the same (i.e., 9 mJ). Cu/Zn and Sn/glass combinations are selected again as in the last section. TEM images of the generated CS-NPs under both laser energies are presented in figure 20 and 21. The size of particles generated from smaller laser energy (8mJ) are smaller (<~5 nm) than that from higher laser energy (31 mJ, ~10~30mn) for both combinations (i.e., Sn/glass and Cu/Zn) examined. A large number of CS-NPs are observed from higher laser energy while no CS-NPs were observed with the lower laser energy condition. All the observed particles from lower laser energy are pure particles contain either the core or shell material (figure 20(b) and (d), figure 21(b) and (d)). In addition to the Gibbs free energy analysis, the significant fewer CS-NPs with lower laser energy can be explained from plasma digestion due to the second laser pulse. The small core particle size from lower laser energy can be easily digested with the second laser induced plasma and prevents the formation of CS-NPs with the proposed double pulse laser ablation scheme.

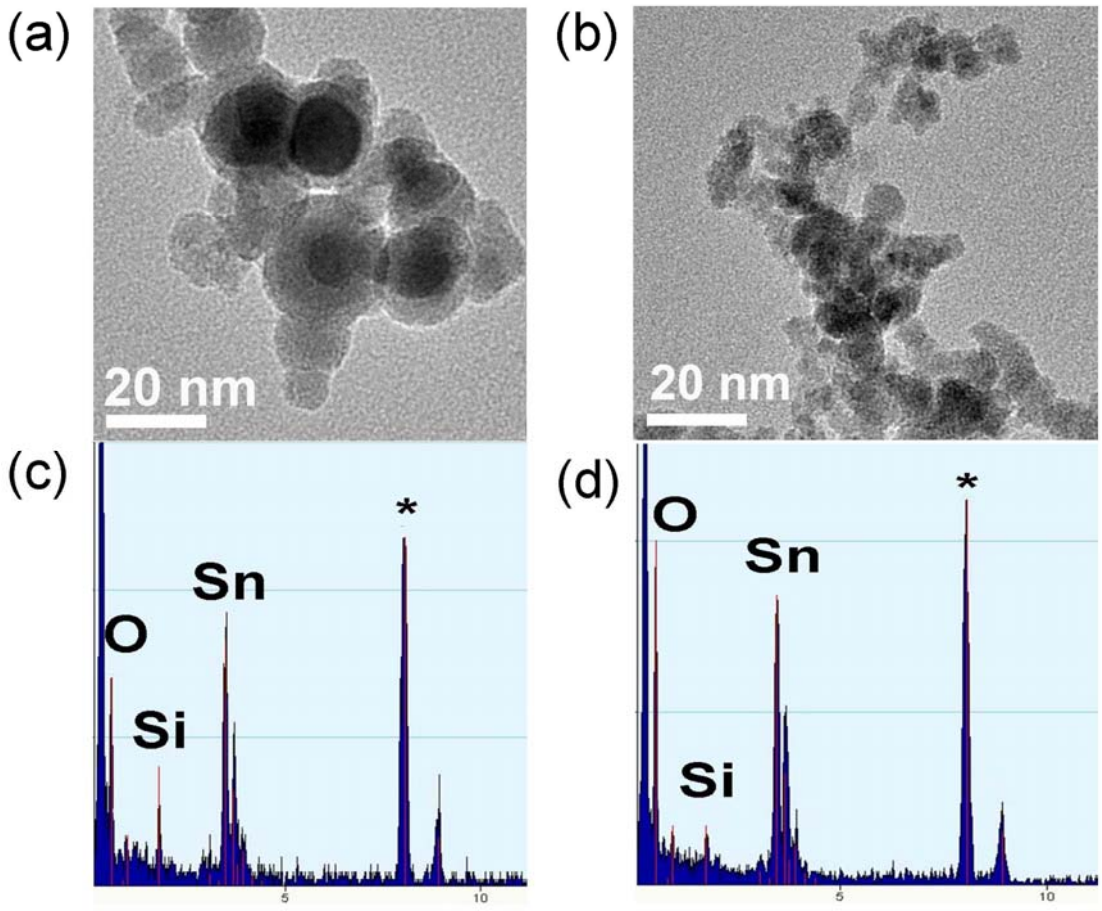

Figure 20. Sn/glass CS-NPs generated from different laser energies for the core targets (E1) when the laser energy for the shell target (E2) is fixed at 9 mJ. (a) Sn/glass CS-NPs from experiments when E1=31 mJ, (b) Sn/glass CS-NPs from experiments when E1=8 mJ, (c) EDS of generated Sn/glass CS-NPs when E1=31 mJ, (d) EDS of generated Sn/glass CS-NPs when E1=8 mJ. More core and shell structures are observed at higher laser energy from the comparison between figure (a) and figure (b). The * peak in EDS results from the substrate of the TEM gird.

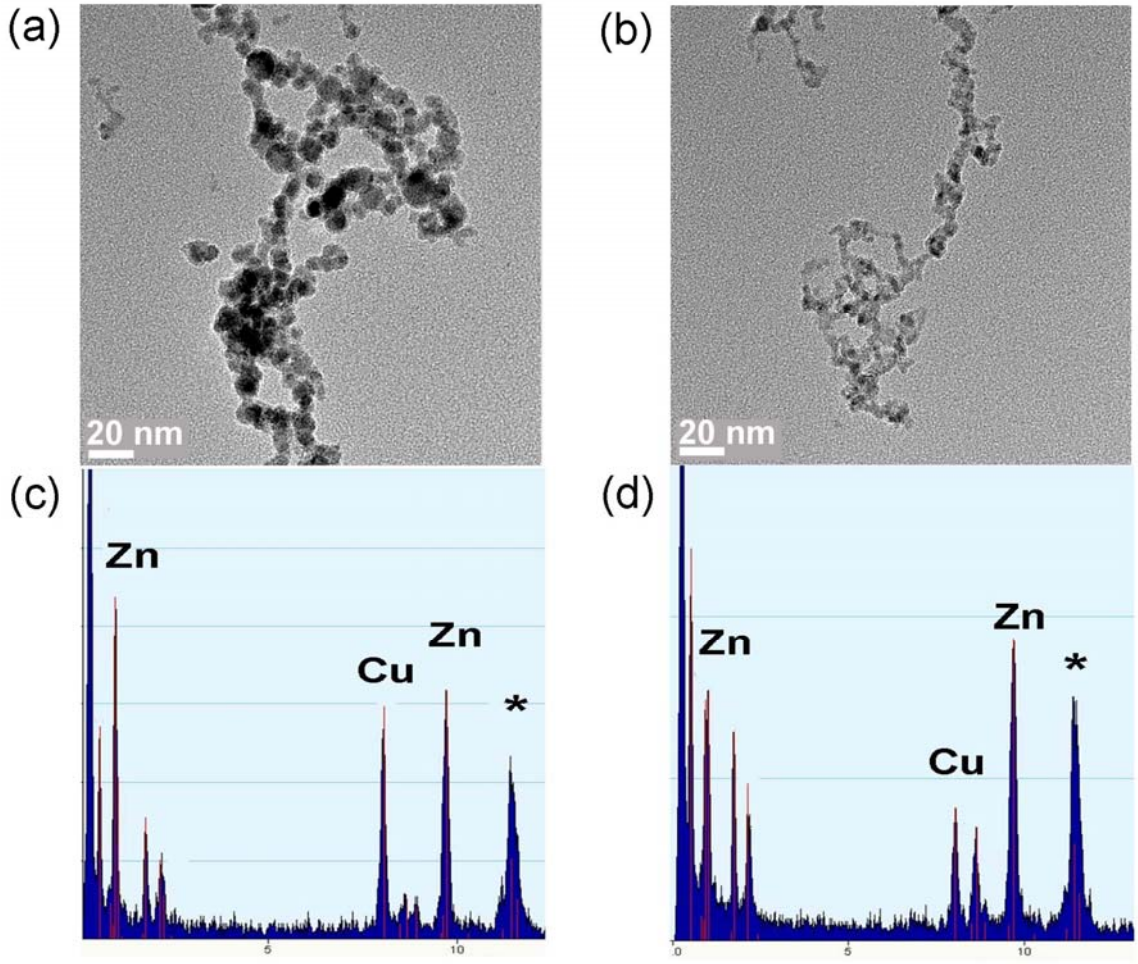

Figure 21. Cu/Zn CS-NPs generated from different laser energies for the core targets (E1) when the laser energy for the shell target (E2) is fixed at 9 mJ. (a) Cu/Zn CS-NPs from experiments when E1=31 mJ, (b) Cu/Zn CS-NPs from experiments when E1=8 mJ, (c) EDS of generated Cu/Zn CS-NPs when E1=31 mJ, (d) EDS of generated Cu/Zn CS-NPs when E1=8 mJ. Note that more core and shell structures can be observed from E1=31 mJ under higher magnification ratio. The * peak in EDS results from the substrate of the TEM gird.

2.4 Summary

Double pulse laser ablation scheme is proposed and examined in this study to generate core/shell nanoparticles (CS-NPs). Compared to other existing methods for generating CS-NPs, the double pulse laser ablation scheme is a simple in-situ method and can be applied to a wider variety of materials. Several types of core-shell nanoparticles (CS-NPs) are successfully generated with the proposed double pulse laser ablation scheme. (e.g. Sn/Glass, Zn/Glass, Zn/Si, Ge/Si, Cu/Zn CS-NPs). Since CS-NPs do not appear under certain experimental conditions examined, four key factors affecting the generation of CS-NPs with this new scheme are also examined in this study, namely; (1) surface tensions of the constructing materials and the associated Gibbs free energy of the CS-NPs if they are formed, (2) contribution of background gases (i.e., He and Ar), (3) contribution of delay time between two laser pulses ablating the core and shell targets respectively, and (4) contribution of the laser energy applied to ablate the core material during the formation of CS-NPs.

Based on the current study, CS-NPs can be successfully generated with the proposed two laser pulses scheme when the Gibbs free energy of the CS-NPs (if they are successfully generated) is lower than the Gibbs free energy of the separately condensed nano-paticles (i.e., the shell material does not coat on the existing core particle but forms shell nano-particles separately). To obtain smaller Gibbs free energy of the resulting CS-NPs, the core material is better to be with higher surface tension than the shell material (though it is not a necessity). Also, the larger core size will ease the formation of CS structures through increasing the difference between the Gibbs free energy of CS-NPs and the separated condensation situation (i.e., ΔE value). The core particle size can be increased through reducing the thermal conductivity of the background gas (e.g., replacing He with Ar) along with increasing the laser energy applied to ablated the core material. As a results, best CS-NP formation is achieved with the proposed double pulse laser ablation in Ar under the maximum laser energy available with the laser utilized (i.e., ~31 mJ). It

is also observed that the delay time between two lasers can affect the successful rate of the formation of CS-NPs with the proposed new scheme. Appropriate delay time between two laser pulses is required for the maximum mixing of the condensed core particles with the vaporized shell material from the second laser pulse. The delay time between the two laser pulses should be longer than the condensation time of the vaporized core material from the first laser pulses (<~1 ms). On the other hand, the delay time between the two laser pulses cannot be too long. Poor material mixing is observed when the delay time between the two laser pulses is ≥8 ms in this study. The condensed core material is moving away from the ablation site under this long delay time and is attributed to the poor mixing of the two ablated material with this new scheme.

3. GENERATION OF CS-NPs WITH LASER ABLATION IN COLLOIDAL SOLUTION

3.1 Introduction

As described in the previous chapter, double pulse laser ablation involves rapid generation, mixing and condensation of plasma from two different samples within ~100s μs, which is difficult to be precisely controlled. In this chapter, we proposed laser ablation of a shell material in a liquid with existing core nanoparticles as an easier alternative to generate CS-NPs with high repeatability.

One of the laser ablation methods for CS-NPs production, laser ablation of solids in liquid environments (i.e., laser ablation of a solid target at the liquid–solid interface) has attracted considerable attention due to its promising potential for high efficient material processing. The difference between laser ablation in colloidal solutions and that in a background gas is the additional confinement of the laser induced plasma/vapor plume with the colloidal solution during expansion [3]. The physical and chemical processes during laser ablation in colloidal solutions have been studied by many groups including the generation, transformation, and condensation of the laser induced plume in liquid [70-74]. During the early stage of laser ablation in colloidal solution, the incident laser pulse passes through the liquid and was absorbed by the surface of the solid sample in a few absorption depth [75]. The irradiated sample material is then heated and vaporized, which is called laser induced plasma plume in liquid. The induced vapor plume expands into the surrounding liquid accompanied with a generation of shockwaves in the liquid. The pressure and temperature of the liquid after the shockwave can be extremely highly (e.g., >~GPa for pressure) compared with the corresponding ablation in air [75-76]. The plume then cools and condenses into liquid and then solid phase (Nanoparticles) of the ablated sample in the confining liquid [77-78]. It is reported that the initial nucleation

and growth of nanoparticles in liquid ambient occurs much faster (~100’ ns) than that in air (~100’ μs) [53, 79].

When nanoparticles exist in the liquid solution before the laser ablation, we expected that the pre-existing surface reduces the cost of surface formation and lowers the nucleation barrier (heterogeneous nucleation) for the ablated material, which leads to easier generation of CS-NPs compared with the double pulse scheme in the last chapter. Based on this understanding, we conducted the laser ablation of solid sample immersed in different colloidal solutions containing pre-existing seed particles. The colloidal solution in mainly transport for the wavelength of the laser selected. The experimental parameters affecting the generation of CS-NPs from ablation in colloidal solutions and are studied in this chapter 3 include the contribution of (1) core materials, (2) shell materials, (3) laser conditions, and (4) core size to identify the size, shape and geometry on the formation of CS-NPs. The resulting CS-NPs are studied with UV-VIS-NIR spectrophotometer to investigate the optical performances of the CS-NPs from laser ablation in colloidal solution.

3.2 Experimental Setup

A schematic for the experimental setup is illustrated in figure 22. A nanosecond Nd:YAG laser (Continuum, Powerlite precision 8000 series) operating at 532 nm with E~100 mJ and 4 ns pulse duration is applied as the light source for ablation. The entire experiment was conducted in an open container with a liquid layer of 4~5 mm in depth. Solid samples are placed at the bottom of the container. Ablation of the immersed solid sample is achieved through delivering the focused laser light through the liquid layer which is almost optically transparent. As a result, the ablated material is mixed with the liquid environment during and after the laser ablation.

Nanoparticles are dispersed in the liquid to form a colloidal solution before the experiment. The pre-existing particles in the colloidal solution became the core of the core/shell nanoparticles to be generated in this study. Two types of liquid environment are prepared in this study, namely, Au colloidal solution and silica colloidal solution. The Au colloidal solution is prepared through mixing 0.1 g of $HAuCl_4$ (Sigma Aldrich, Gold(III) chloride hydrate, 99.999% metalbase) with 10 g of pure DI water for 15 minutes in the ultrasonic bath (see figure 23). The silica colloid is prepared through mixing 0.5 g of silica powder (0.1 or 1 μm in diameter) with 50 g of DI water for 1hr in the ultrasonic bath. TEM images of colloidal particles are presented in figure 23 (a) and (b). CdSe (ESPI Metals, pieces, 5N+ purity), Se (ESPI Metals, pieces, 5N+ purity), Sn (ESPI Metals, sheet, 1×1 inch, 3N purity), Si (Addisonengineering Inc., wafer, diameter 125 mm, N-type, orientation <100>), and Cu (Goodfellow Inc., plate, 2×2 inch, 99.99+% purity) are selected as the immersed solid target to be ablated as the shell material in the current study. The laser spot diameter was controlled to be ~ 1 mm during the 15 min to 40 min ablation of the immersed solid in this study. The generated particles after the ablation of specified solids in the colloidal solution are collected by carbon coated TEM grids (Electron Microscopy Sciences, CF200-Au, CF200-Cu) The colloidal solution is better mixed through ~15 min of sonication before the particle collection to ensure a consistent collection results.

Examination of the size, shape, crystalline structure, and the material composition of the collected particles after the ablation are examined with a high resolution transmitted electron microscope (HRTEM, FEI Tecnai G2 F20 FE-TEM) and energy dispersive X-ray spectroscopy (EDS, PGT EDS System), respectively.

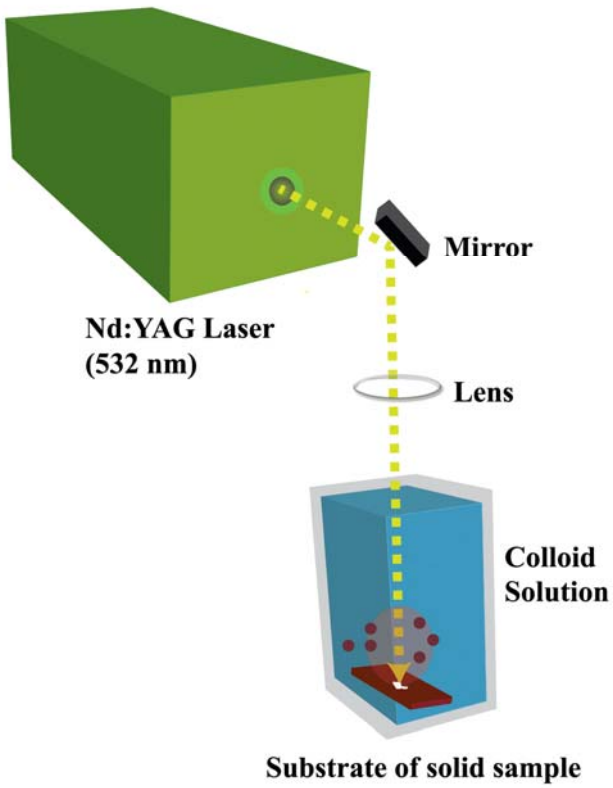

Figure 22. Schematic of the experimental setup for the laser ablation in colloidal solutions. ~1mm laser beam is focused on the target material in liquid. The thickness of surrounding liquid is applied about 3~5 mm.

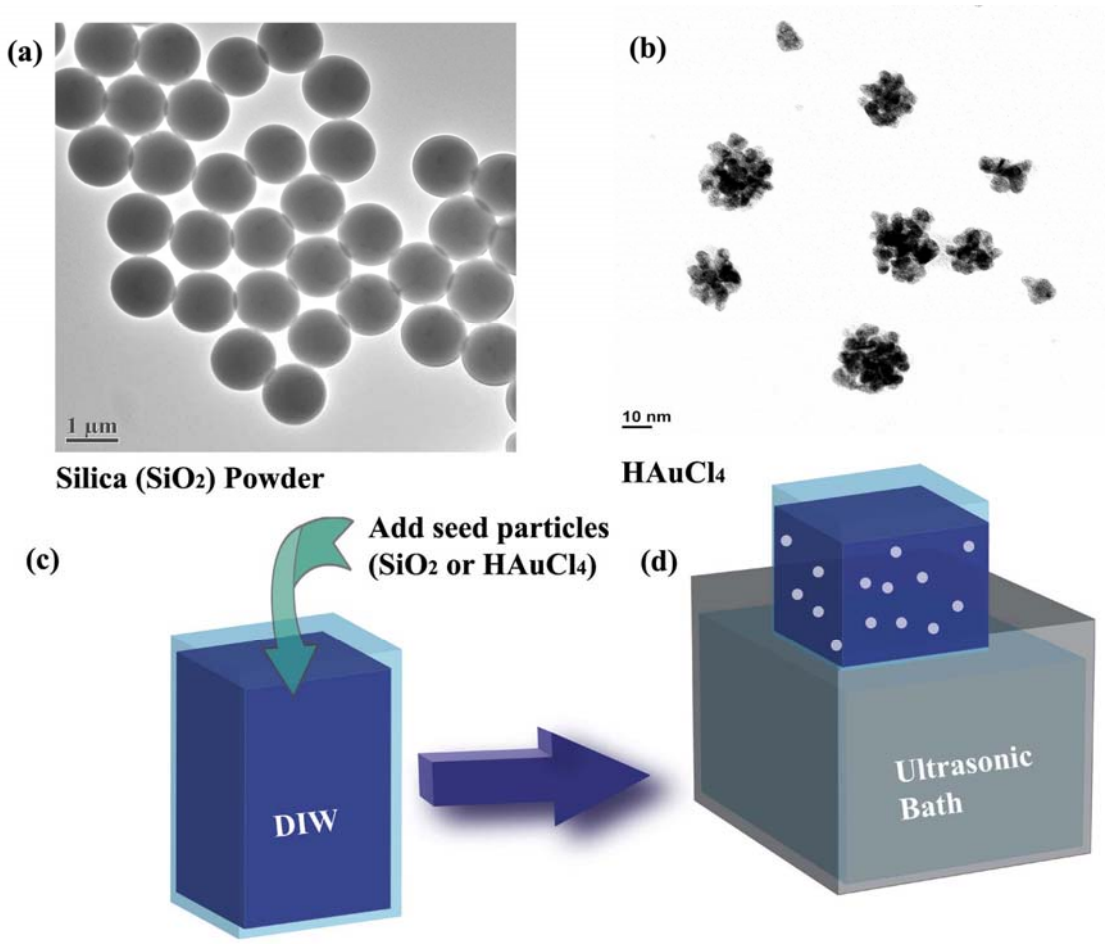

Figure 23. TEM images of (a) seed Silica (SiO_2) powder, (b) seed HAuCl4 cluster and generation of colloid with (c) mixing in DI water (d) ultrasonic mixing (15 min for Au cluster and 1 hr for SiO_2 powder)

3.3 Results and Discussion

Several combinations of CS-NPs are successfully generated (e.g., Au/CdSe, Au/Si, Au/Se, SiO_2/Sn, SiO_2/Cu, SiO_2/Au and SiO_2/Ag CS-NPs) with the proposed laser ablation in colloidal solutions. The characteristics of the generated CS-NPs with different (a) colloidal material, (b) shell material, (c) colloid size, and (d) laser conditions are summarized as follows.

3.3.1. Laser ablation of semiconducting materials in Au colloidal solution

(a) Au/CdSe, Au/Se, Au/Si CS-NPs formation

Observations have been made for a long time on the interesting optical properties of nano-sized particles composed of Au due to its unique interband electronic transitions [80]. The optical properties of gold nanoparticles can be fine tunes to fit specified conditions by applying additional shell claddings. One of the important types of gold CS-NPs, CS-NPs made of Au core and dielectric or semiconductor shell are attracted attention to numerous research fields. For example, Au/silica CS-NPs can provide the surface plasmon amplification by stimulated emission of radiation (SPASER) that support the possible applications in nano-laser or nano-lithography [81-82]. Moreover, Au/CdS CS-NPs are known as its third-order nonlinear susceptibilities and ultra-fast nonlinear optical response so that application can be made in nonlinear optics [83-85]. Further, multilayered nanoparticles such as Au-Silica-Au particles provide the high tunability in extinction shift by adjusting its core and shell dimensions [86-88]. Considering its very promising application, Au colloid is chosen as the first liquid media.

Au nanoparticle by surface plasmons can transfer to the conduction band of the semiconducting materials shell and recombine with holes in the valence band, which can cause the enhanced band gap and defect emissions [89]. Similarly, it is believed that

matching the surface plasmon polariton on Au core with the band gap energy of the semiconductor shell can lead to fast energy transfer between semiconductor shell and Au core [90]. These tunable band gap properties can be applied in non-linear optics and photocatalyst [83, 89, 91].

The semiconducting materials selected in the ablation as the shell material are Se, CdSe and Si. The resulting Au/CdSe, Au/Se, Au/Si CS-NPs and the corresponding EDS profiles are illustrated in figure 24. From TEM images, core/shell structures are clearly observed in the generated particles. The pre-exiting Au colloids form the core of the generated core/shell structures with semiconductors as the shell. The sizes of the prepared Au colloids range from 5 to 70 nm in diameter. The observed shell thickness of each Au/CdSe, Au/Se and Au/Si CS-NPs are around 10~25 nm, 10~20 nm and 2~5 nm, respectively. Compared with CdSe and Se shells, the Si nanoshell is less uniform on the prepared Au core. (c.f., figure 24(c)&(f))

For all the Au-semiconductor combinations examined, a portion of ablated semiconductor shell material can always deposit on existing cores and forms CS structure. The remaining portion forms agglomerated single element nanoparticles of the shell material. The low selectivity between the core and shell material for the proposed laser ablation in colloidal solutions is different from the formation of core/shell structures with our previous double pulse laser ablation study. To understand the low selectivity with the new approach by ablation in colloidal solution, free energy analysis for the formation of CS-NP is calculated as follows.

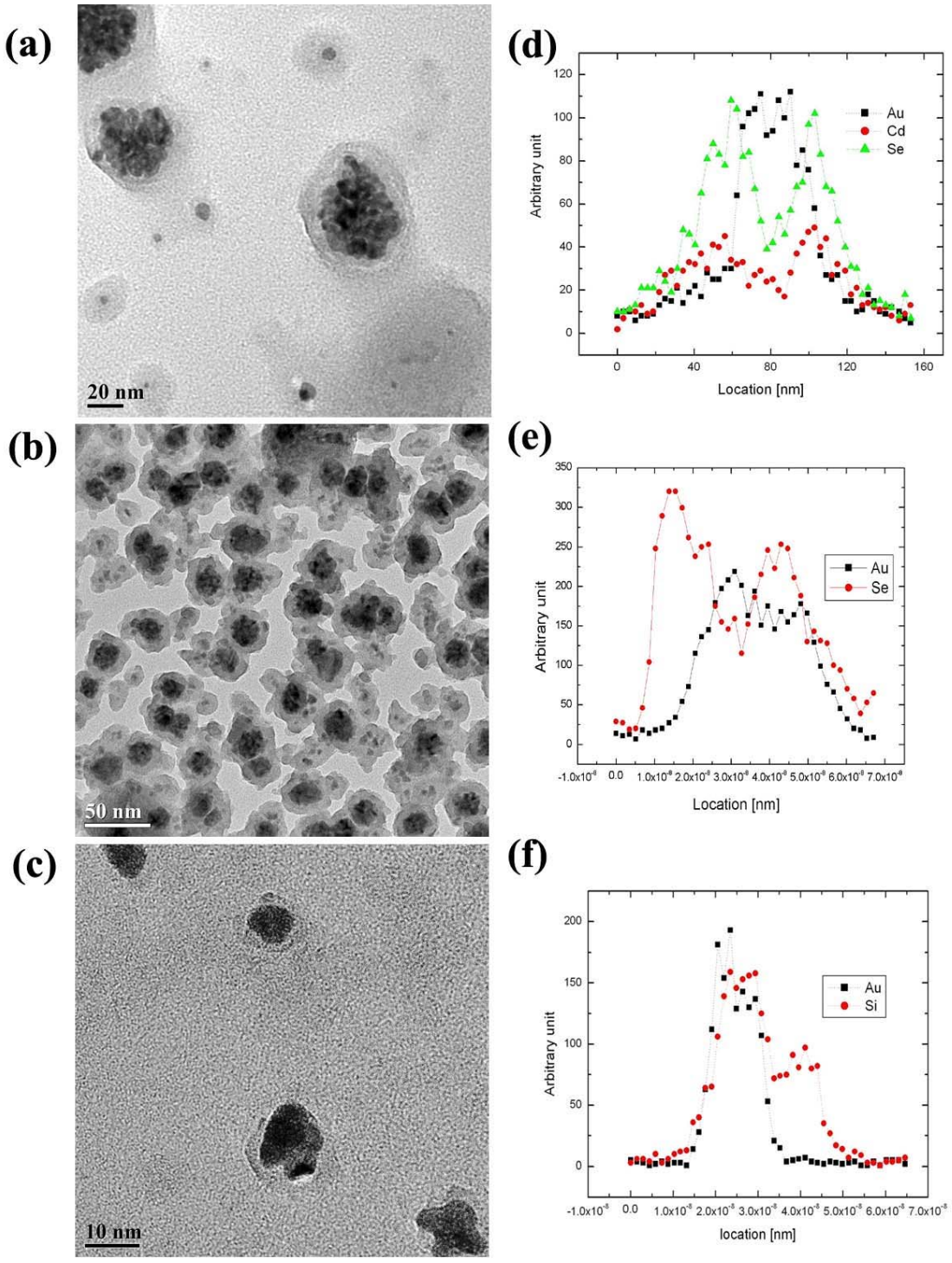

Figure 24. TEM images of (a) Au/CdSe, (b) Au/Se, (c) Au/Si CS-NPs and corresponding EDS line profiles of (d) Au/CdSe, (e) Au/Se, (f) Au/Si CS-NPs.

(b) CS-NPs generation process in colloidal solution

Based on the experimental results in section (a), a detailed description of CS-NPs generation steps is presented in figure 25. When laser beam arrives on the immersed solid sample (A), the light is absorbed by photon-electron coupling and melted by electron-phonon collision in the sample material. This will result in temperature increases above the melting and boiling temperatures, and the vapor plume forms and expands into the liquid (B). Due to the heat transfer from the plume to water environment, water vapor forms and surrounds the vapor plume. At the beginning of plume generation, the colloids exist only in the water vapor and environment (B). Further, sample and water vapor are mixed during the plume expansion due to hydraulic instability and diffusion between two vapor molecules. Then the seed colloids move inside the mixed vapors (D). As temperature decreases below the melting point of the sample material, sample vapor condenses through the homogeneous nucleation or heterogeneous nucleation. If condensation occurs on the existing seed surface, the seed particle coats with the sample material and CS-NP can be generated. Consequently, the colloidal solution will include CS-NPs and single NPs from the laser ablated material.

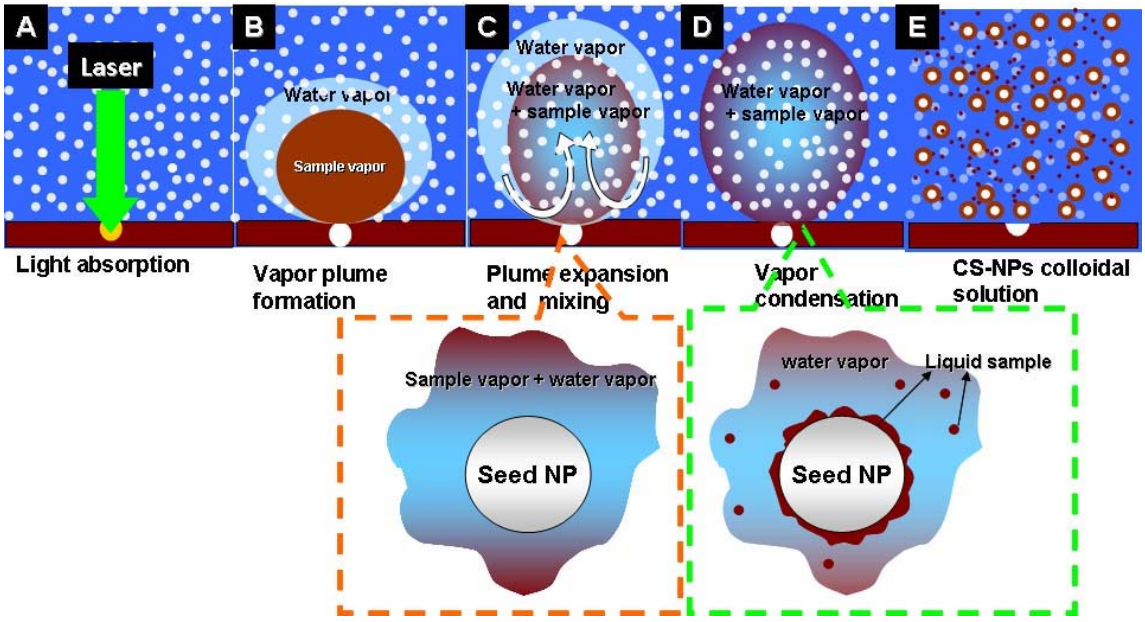

Figure 25. CS-NPs generation process during the laser ablation in colloidal solution

(c) Free energy calculation of shell formation on the pre-existing surface

Compared with the generation of CS-NPs from double pulse ablation, in which both core and shell material experience vapor to solid phase change during the CS-NPs formation, the core material of the present study pre-exists in the colloidal solution as solid nano colloids. The induced shell vapor from ablation of the shell material at the bottom of the colloidal solution is the only material in the vapor to solid phase change in this new method. Therefore, the corresponding free energy analysis is much more simplified compared with the double pulse laser ablations.

Theoretically, nanoparticles generated from the laser ablation are explained with the nucleation and condensation processes of laser induced vapor plume as briefly described in section (b). Also, the particle sizes generated from the nucleation and condensation are determined from the critical radius of homogeneous nucleation and the duration of the particle growth [92-93]. Note that the homogeneous nucleation during the laser ablation refers to the phenomena that spherical droplets form in vapor without pre-

existing concentration surfaces when the temperature of the laser induced vapor plume is less than the boiling temperature of the sample. However, if pre-existing surface is available during the condensation of laser induced vapor plume, the critical cluster will be formed either in the middle of vapor (homogeneous nucleation) or on the pre-existing surface (heterogeneous nucleation) as presented in figure 26.

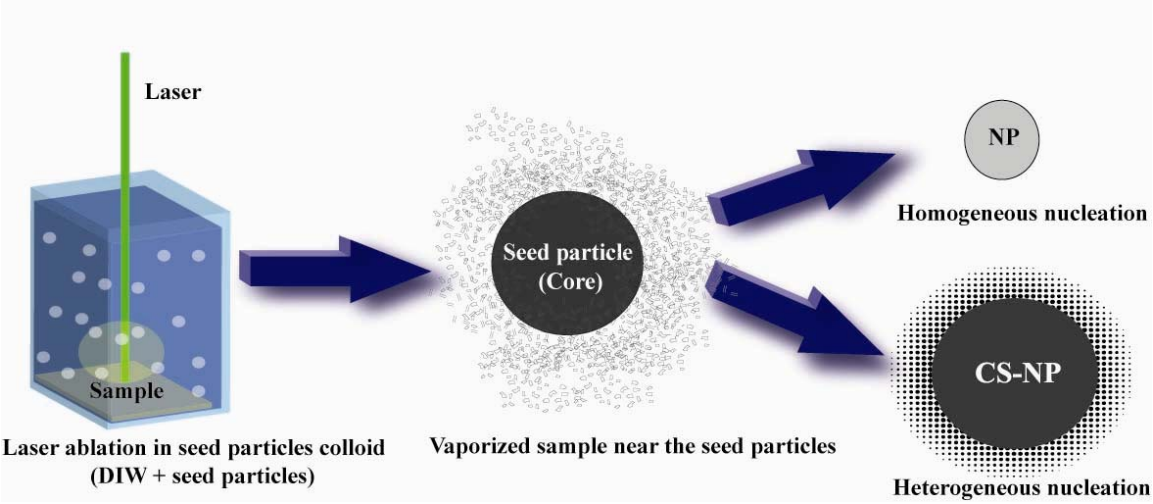

Figure 26. Two possibilities of condensation process with laser induced vaporized material. It could be formed as a single nanoparticle through homogeneous nucleation or condensed on the existing nanoparticle through the heterogeneous nucleation

Based on the classical nucleation theory, thermodynamic explanation of shell formation on the existing particle with the laser ablation is as follows. Assume that pre-existing surface is the perfect sphere (ex. silica nanoparticle), and the laser induced vaporized material is condensed on the existing particle at its boiling temperature (see figure 27), then the free energy of condensed material can be written as equation 3.1 [94]

$$\Delta\varphi^{het*} = f_{\varphi}\Delta\varphi^{homo*} \tag{3.1}$$

where, $\Delta\varphi^{homo*}$ is the formation free energy of the homogeneous critical cluster at the same conditions, f_{φ} is a geometric factor defined as equation 3.2 [94]

$$f_\varphi = \frac{1}{2}\left[\begin{array}{l} 1-\left(\frac{r^* - R_p\cos\vartheta}{d}\right)^3 + \left(\frac{R_p}{r^*}\right)^3\left\{2-3\left(\frac{R_p - r^*\cos\vartheta}{d}\right)+\left(\frac{R_p - r^*\cos\vartheta}{d}\right)^3\right\} \\ -3\cos\vartheta\left(\frac{R_p}{r^*}\right)^2\left\{1-\left(\frac{R_p - r^*\cos\vartheta}{d}\right)\right\} \end{array}\right] \quad (3.2)$$

where, r is the cluster radius, Rp is the particle radius, ϑ is the contact angle, r* is the critical radius of homogeneous nuclei, and $d = \sqrt{r^2 + R_p^2 - 2rR_p\cos\vartheta}$. Geometric information is presented in figure 27. Note that the contact angle is related to the surface tensions between liquid and solid ($\sigma_{l,sol}$), vapor and liquid ($\sigma_{g,l}$), and vapor and solid ($\sigma_{g,sol}$). According to Young's equation, the contact angle is express as equation 3.3.

$$\cos\vartheta = \frac{\sigma_{g,sol} - \sigma_{l,sol}}{\sigma_{g,l}} \quad (3.3)$$

As presented in equation 3.2, f_φ is dependent on R_p, ϑ and r*. Since r* is material dependant property, f_φ is the actual function of R_p and ϑ. Figure 28 shows the calculated f_φ profile with respect to ϑ and R_p in case of Cu nucleation on the spherical silica core. For all values of ϑ and Rp, f_φ is lower than one ($0 < f_\varphi \leq 1$) represents that the existing surface reduces the cost of surface formation and makes nucleation barrier lower if pre-existing surface is available during the condensation process. Therefore, heterogeneous nucleation will likely be induced. Similarly, the laser induced vapor plume will easily be condensed on the pre-existing nanoparticles and it will form a core/shell structure due to its lower threshold energy barrier. Our experimental results are well matched with this energy consideration because a shell can always form on existing cores through ablation of the shell material in the colloidal solution.

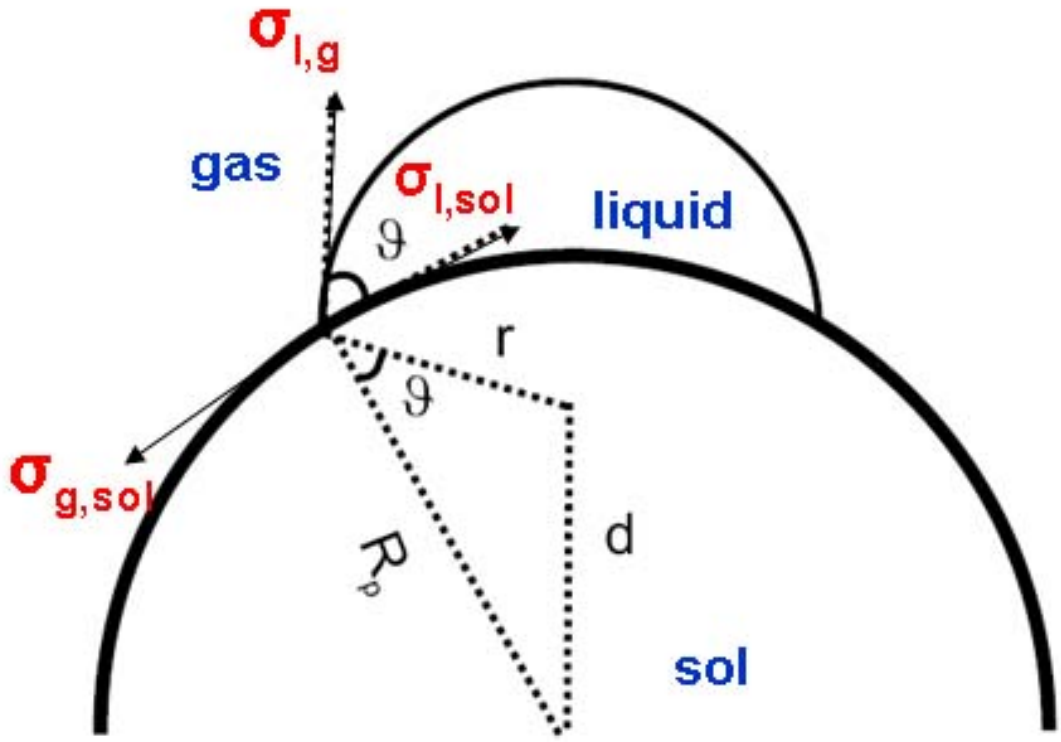

Figure 27. A condensed cluster from laser induced vapor plume on a surface of a spherical particle. The tangent of the cluster surface is marked with $\sigma_{l,g}$, tangent of the particle surface with $\sigma_{l,sol}$, r is the cluster radius, R_p the particle radius and ϑ is the contact angle. The corners of the triangle shown are the center of the spherical particle, the center of the cluster sphere and the point where cluster and particle surfaces meet. Tangent $\sigma_{l,g}$ is perpendicular to the side r, and tangent $\sigma_{l,sol}$ is perpendicular to the side R_p [94].

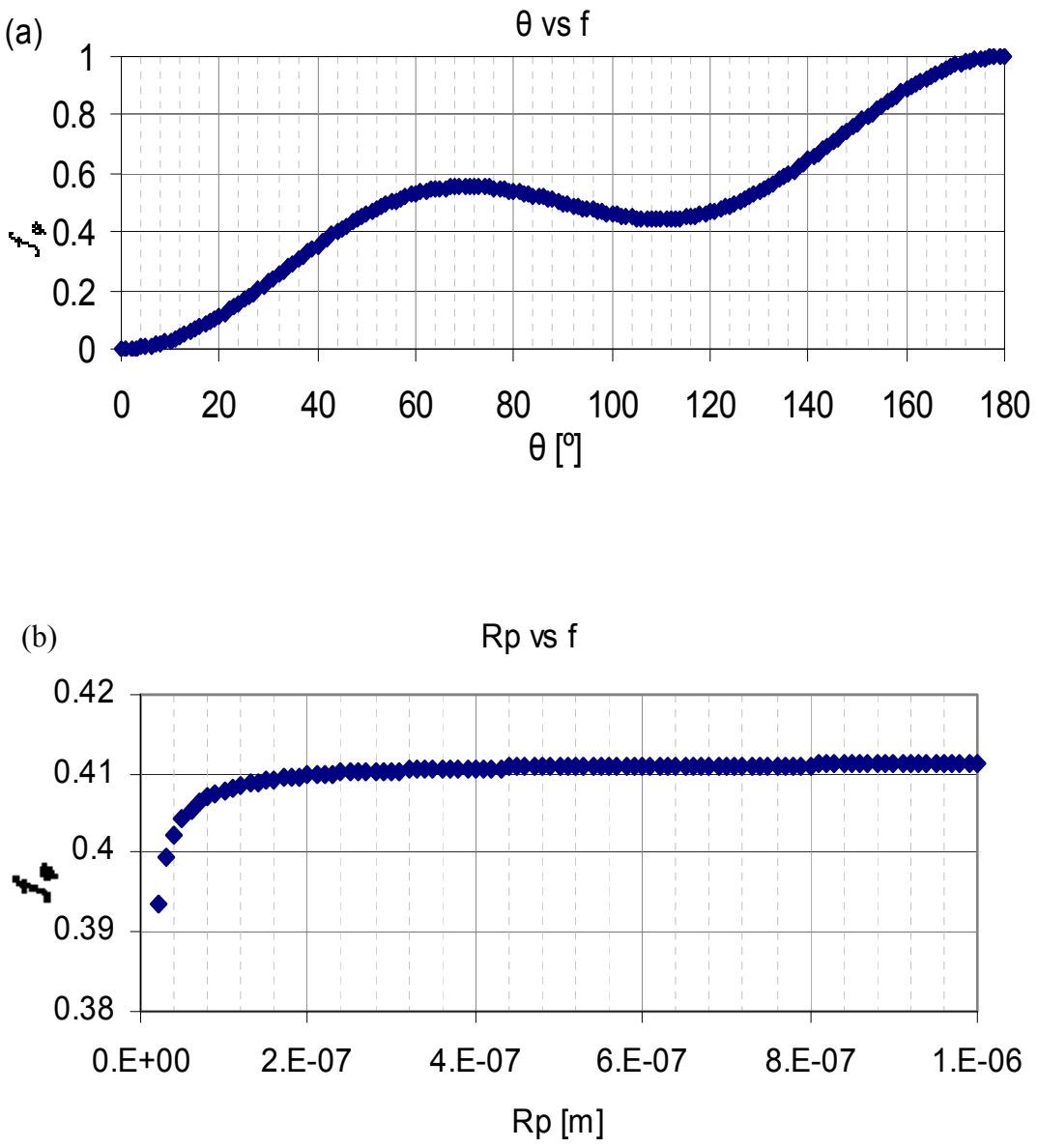

Figure 28. (a) Profile of geometric factor (f_φ) with respect to contact angle (ϑ), (b) Profile of f_φ with respect to seed particle radius (Rp). For any Rp and ϑ values, f_φ is less than one meaning that free energy for heterogeneous nucleation is always lower than homogeneous nucleation.

3.3.2 Laser ablation of metals in silica colloidal solution

Based on the free energy consideration, it is expected that the formation of CS-NP is affected by the shell materials and the size of the core seed. Based on the free energy analysis, the Gibb's free energy of the formation of CS-NPs is reduced (a) when the contact angle between the shell and core material becomes smaller, and (b) when the diameter of the core seed becomes smaller. The smaller Gibb's free energy facilitates the formation of CS-NPs when the laser ablation is conducted in the colloidal solution. The formation of CS-NPs with different shell material and core diameters as well as the ablation times, which is one of the key laser parameters during laser ablation and the formation of CS-NPs are reported as follows.

(a) Effect of shell materials on the CS-NPs generation

To precisely control the size of the core seed, monodispersed silica nanoparticles are mixed with DI water as the colloidal solution during the liquid immersed laser ablation. Silica (SiO_2) is an economic and stable base to construct dielectric/metal core/shell plasmatic structures valuable in biomedical applications [95-96]. Monodispersed SiO_2 can be prepared with standard Stöber process or sol-gel method [97-100]. 100 nm silica particles (Fiber Optic Center Inc., Angstromsphere Monodispersed Silica Powder) are selected in this study as the core seed of the DI water based colloidal solution. Four types of metals, namely, Sn,Cu, Ag and Au are chosen as the shell material to be ablated in the SiO_2 colloidal solution for 30 min with E=~100 mJ and λ=532 nm. The resulting CS-NPs are presented in figure 29. For all four examined metals, ablated metal condenses on the surface of existing SiO_2 colloids and forms CS-NPs. The shell quality shows big deviation among the four studied metals. For SiO_2/Sn CS-NPs, fully covered but non-uniform shell layer made of small Sn clusters (<10nm) is observed in figure 29 (a). However, SiO_2/Cu CS-NPs shows the comparably uniform Cu shell with ~ 5 nm thickness. (see figure 29 (b)) For Ag or Au shell material, shell material is attached to

the SiO_2 core as small separated spheres as in figure 29 (c) and (d). The shell quality with different shell material can be explained with adhesion energy of metal films on oxides [101]. The adhesion energy is the work needed to separate the metal/oxide interface which is expressed as [102]

$$E_{adh} = \gamma_{v/m} + \gamma_{v/ox} - \gamma_{m/ox} \tag{3.4}$$

The adhesion energies of examined materials on SiO_2 re listed in table 3. As presented, Cu has much stronger adhesion energy on the SiO_2 surface than other examined materials indicating the strong bonding exists on the shell formation. Therefore smoother shell, compared with Sn, Au and Ag, can be obtained with Cu shell on the SiO_2 core. Even though uniform shell is not formed with Sn as the shell material, a very thick Sn shell was formed on the SiO_2 compared with all other three examined materials as shown in figure 29(a) under the same laser condition. This thick Sn shell can be explained with the thermal and optical properties of Sn as listed in table 4. Sn has high light absorption (lower reflectivity) at 532nm (the incident laser wavelength that we applied) and low ΔH_{fusion} among the four shell material examined. As a result, much more Sn vapor can be generated during the laser ablation which allows a thick Sn shell to be condensed on the SiO_2 surface. The spherical condensed structures of Au and Ag on the SiO_2 shell can be attributed to the large contact angle between Au and Ag the SiO_2 surface as illustrated in table 3.

Table 3. Comparison of the interfacial properties between selected metals and the SiO_2 surface [103]

Metal	E_{adh} (mJ/m^2)	$\gamma_{v/m}$ (mJ/m^2)	$\gamma_{v/ox}$ (mJ/m^2)	ϑ (º)
Ag	174	814-926	605	142
Au	227-246	1125	605	140
Cu	474	1233	605	128
Sn	198-253	464-573	605	124

Table 4. Comparison of optical and thermal properties of examined materials)

	Sn	**Au**	**Cu**	**Ag**
Reflectivity (532nm)	0.54	0.76	0.61	0.95
Surface tension (mN/m)	560	1169	1303	966
Thermal conductivity (W/m-K)	66	318	401	429
T_{melt}(K)	505	1337	1357	1234
T_{boil} (K)	75	3129	2835	2435
ΔH_{fusion}(kJ/mole)	7	12.5	13.2	11.2
$\Delta H_{vaporization}$(kJ/mole)	296	324	300	250

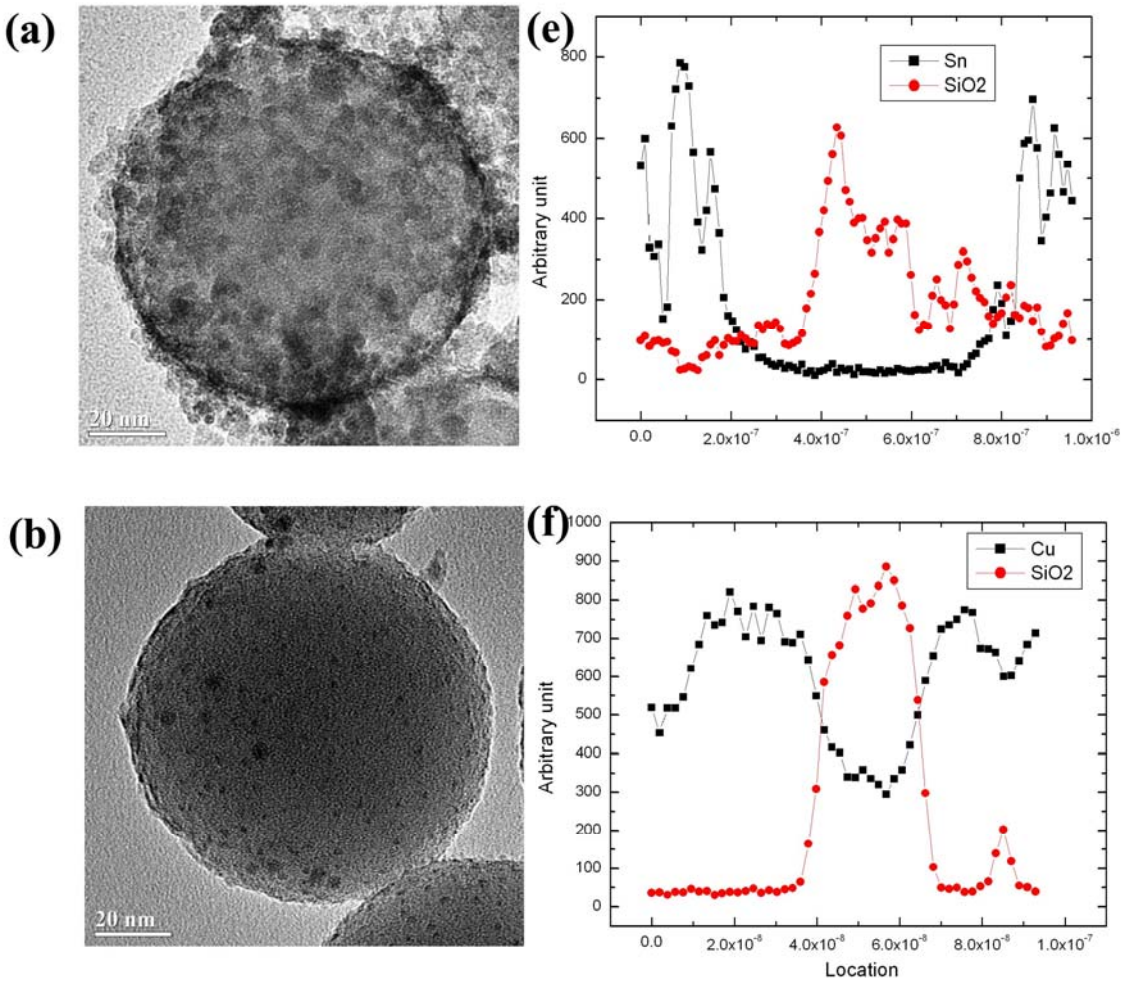
(a)
20 nm
(e)
Sn
SiO2
Arbitrary unit
0
200
400
600
800
0.0
2.0x10-7
4.0x10-7
6.0x10-7
8.0x10-7
1.0x10-6
(b)
20 nm
(f)
Cu
SiO2
Arbitrary unit
0
100
200
300
400
500
600
700
800
900
1000
0.0
2.0x10-8
4.0x10-8
6.0x10-8
8.0x10-8
1.0x10-7
Location

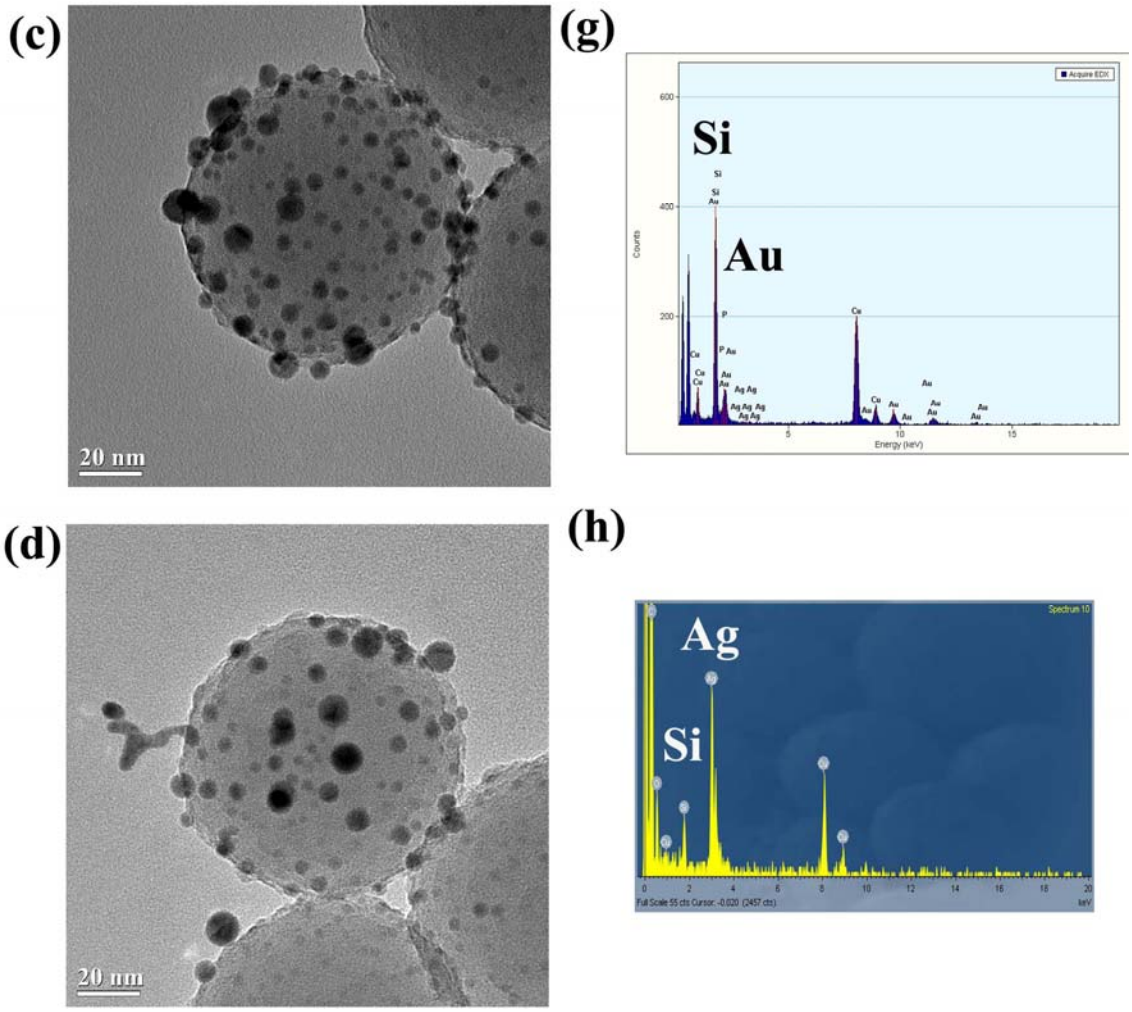

Figure 29. TEM images of (a) SiO_2/Sn, (b) SiO_2/Cu, (c) SiO_2/Au, (d) SiO_2/Au CS-NPs and corresponding EDS results. SiO_2/Sn and SiO_2/Cu CS-NPs show the fully covered shell compared with SiO_2/Au and SiO_2/Ag CS-NPs. Therefore, EDS line profile was only taken for SiO_2/Sn and SiO_2/Cu CS-NPs (e, f). From TEM and EDS line profile, it is clearly show the generated SiO_2/Sn and SiO_2/Cu are core/shell structure. In (f) and (g), EDS signal show each attached small clusters are Au and Ag, respectively. Among four types, Cu shows the comparably uniform shell than other metals. Also Sn shows the fully covered but not uniform shell. Au and Ag present neither uniform nor fully covered shell.

(b) Effect of core size on the CS-NPs generation

As described in the previous chapter (3.3.1.c), the core size affects the free energy on the shell formation. From the geometrical relation presented in equation 3.3 and figure 28 (b), it is expected that the smaller core provides lower free energy barrier for the formation of CS-NPs and the resulting better quality of the CS-NPs structures. To verify our prediction, two different core sizes are examined, namely, 0.1 and 1 μm of SiO_2 nanoparticles. Cu and Sn, which can provide fully covered shell structures on the SiO_2 core under the laser condition, are selected as shell material in this portion of study. The resulting CS-NPs after 20 minutes of laser ablation are shown in figure 30. Based on figure 30, the shell structure is not significantly different for the two core sizes examined. This would be due to the size tested in the current study provides only ~3 % difference in the geometric factor (figure 28(b)). Therefore, the size effect due to the lower energy barrier is not clearly observed when the core diameter reduces from 1 μm to 0.1 μm. However, compared with the 0.1 μm core seed, many single element particles wth the shell material aer formed in accompany with the CS-NPs when 1 μm core seed was applied. (Compare figure 30 (a) with (c)) This reduced of the formation of accompanied single element NP when smaller core seed was applied in the CS-NP generation can be explained with the larger available seed surface area for condensation during the laser ablation when smaller core seed was applied. Since the SiO_2 colloidal solutions are prepared with constant colloidal mass to DI water ratio during the experiment, the number of core seeds as well as the surface area of the seeds are inversely proportional to the diameter of the SiO_2 particles as the core seeds. The number of 0.1 μm of SiO_2 particles is a 1000 times larger than 1 μm of SiO_2 under the same weight ratio, which corresponding to 10 times large surface area. As a result, available surface area for condensation with of small SiO_2 particles (i.e., 0.1 μm) is 10 times larger than that with big SiO_2 particles (i.e., 1 μm). Therefore, almost all the ablated material can attach to the core seeds and forms CS-NPs, which prevents the formation of the single element NPs from homogeneous nucleation, when smaller core seeds are applied.

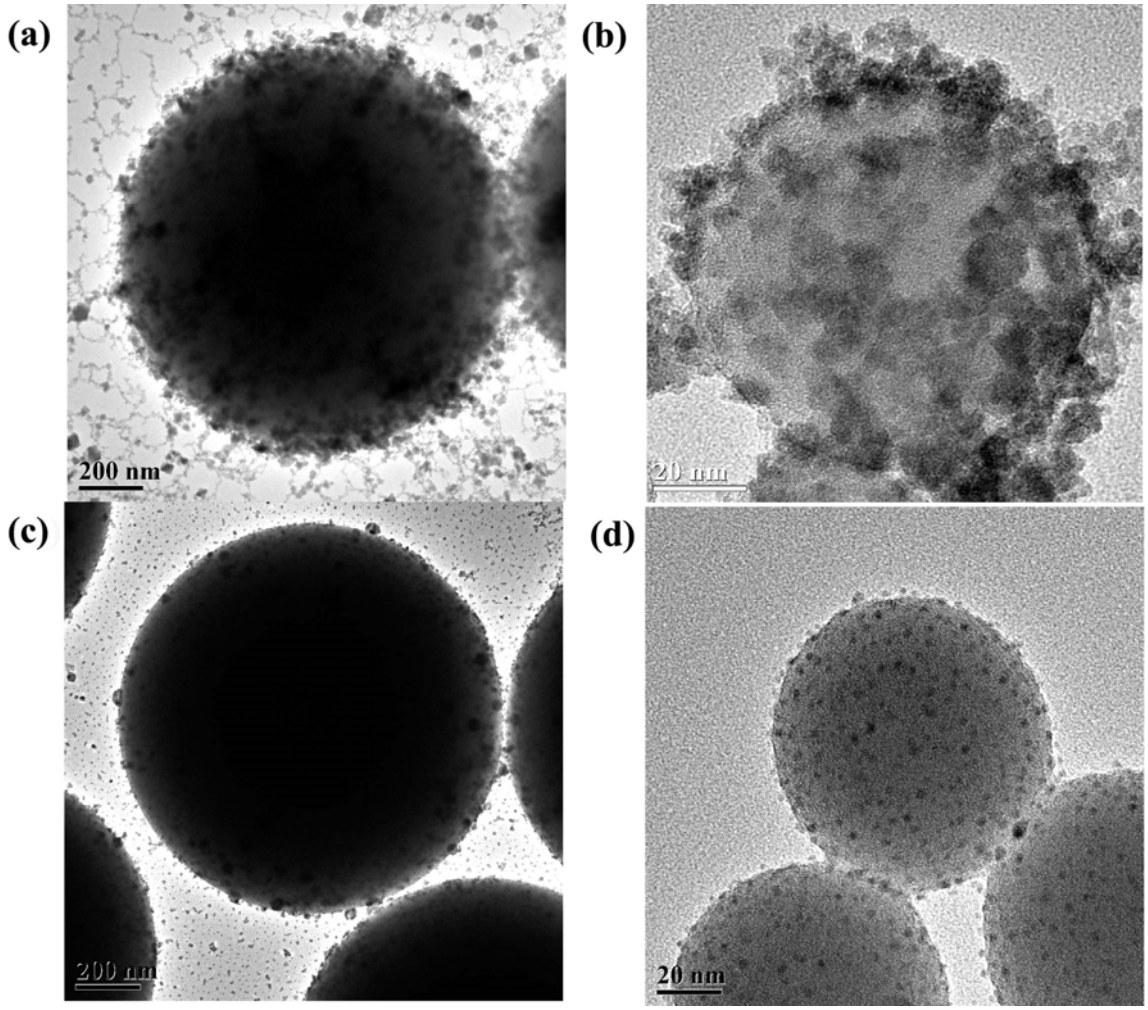

Figure 30. TEM images of (a) SiO_2/Sn CS-NPs with 1µm silica core, (b) SiO_2/Sn CS-NPs with 0.1µm silica core, (c) SiO_2/Cu CS-NPs with 1µm silica core, (d) SiO_2/Cu CS-NPs with 0.1µm silica core

(c) Effect of ablation time on the shell thickness

The total mass of ablated material is proportional to the ablation time. In this section, different ablation times namely, 10, 20 and 30 min of laser ablation are applied on the immersed Cu and Sn samples in SiO_2 colloidal solution with monodisperse silica particles of d~0.1 μm as the colloids. TEM images of generated CS-NPs are presented in figure 31. Based on figure 31, thicker shell are observed on the silica core when the ablation time is increased. Overall, it is found that most SiO_2 particles are partially covered with Sn and Cu for 10 min ablation time as shown in 3.10 (a) and (b). The SiO_2 particles are fully covered after 30 min of laser ablation for both Sn and Cu targets as shown in (e) and (f). The increase of the shell thickness can be attributed to the increased of the ablated material with respect to the ablation time. As a result, more vaporized materials are condensed on the SiO_2 particle which causes thicker shell as ablation time increases.

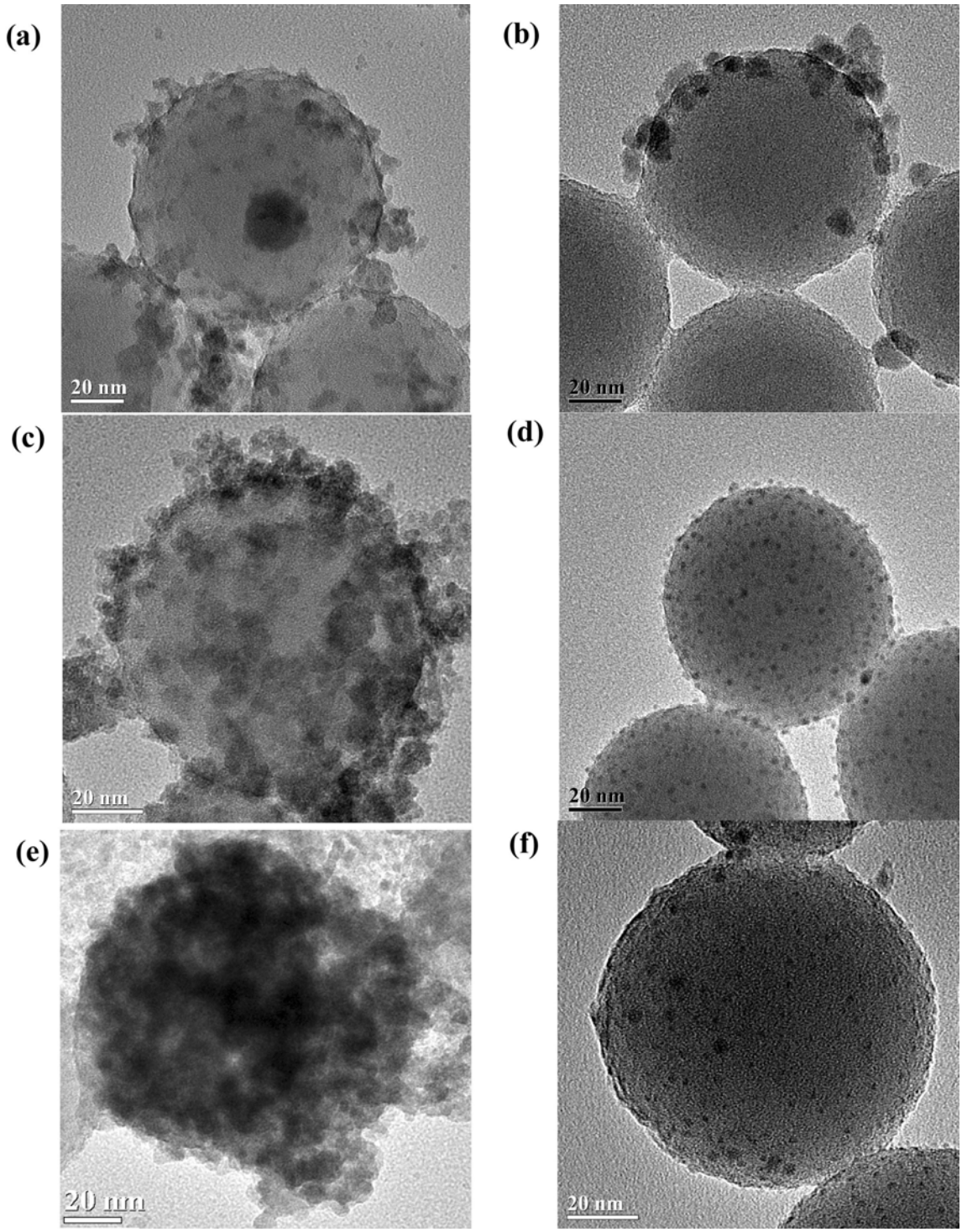

Figure 31. TEM images of (a) SiO_2/Sn CS-NPs with 10 min of laser ablation, (b) SiO_2/Cu CS-NPs with 10 min of laser ablation (c) SiO_2/Sn CS-NPs with 20 min of laser ablation, (d) SiO_2/CuCS-NPs with 20 min of laser ablation, (e) SiO_2/Sn CS-NPs with 30 min of laser ablation, (f) SiO_2/CuCS-NPs with 30 min of laser ablation

3.4 Summary

In this portion of study, CS-NPs generation with the laser ablation in colloidal solutions is experimentally examined. Compared to the double pulse laser ablation, this new methodology provides high productivity in CS-NP formation, a better control of the core size and shell thickness, and a higher flexibility in the selection of core and shell material. Two types of colloids are applied as the core materials, namely, Au and SiO_2 colloids. Results indicate that for all the core-shell material combinations examined, namely, Au/CdSe, Au/Se, Au/Si CS-NPs SiO_2/Sn, SiO_2/Cu, SiO_2/Ag and SiO_2/Au, CS-NPs are successfully generated. From the free energy analysis, it is found that the free energy of the shell formation depends on the core/shell interfacial energy and the core size. However, for all the core-shell combination, the free energy for the condensation of shell material on existing solid core (i.e., heterogeneous nucleation) is always smaller than the condensation of the ablated shell material into pure NPs through homogeneous nucleation.

It is found in this study that the formation of CS-NPs through ablation of solid in colloidal solution is affected by (a) the adhesion energy between the core and shell material, (b) the diameter of the core seed, and (c) the ablation time. For adhesion energy, Cu, which has relatively higher adhesion energy to SiO_2 compared with Sn, Au and Ag, provides comparably smooth and uniform shell formation while Au and Ag present poor quality shell formation. For smaller core diameter, resulting shell formation is not strongly affected by core size in the current conditions. However, smaller core can provide larger surface area during the vapor condensation when it attach to the core seeds and forms CS-NPs. For longer ablation time, shell thickness is presented as a strong function of ablation time indicating that the shell size can be controlled with the current method.

4. OPTICAL PROPERTIES OF CS-NPs

4.1 Introduction

One of the most important characteristics of metal NPs is the dependency of the optical properties on the particle size and shape. For example, Au is yellowish in colloidal solution, while thin Au films are blue under transmission imaging [104]. This blue color film steadily changes to orange, purple, and red, as the grain size of the film is reduced down to ~3 nm [104]. The change of the above color can be attributed to the shift of the wavelength of associated plasmon resonances [86], which is collective electron motion in response to the alternating electric field of incident electromagnetic radiation.

CS-NPs allow tunable surface plasmon and localized plasmon resonance frequencies as functions of the size, shape, and material combination of the CS-NPs. [105]. The plasmon resonance can induce orders local field enhancement both inside and in the near-field of nanoparticles. The enhanced electric filed is especially important in surface enhanced Raman spectroscopy [106], surface plasmon resonance sensing [107] and fluorescent enhancement when the detection signal is proportional to the local electric field intensity [108].

The frequency of the plasmon resonance can be observed from the absorption spectra of the CS-NPs. In the current study, UV-VIS-NIR spectrophotometer (Hitachi High-Tech, U-4100) is applied to measure the absorption spectra of collected SiO_2/Au and SiO_2/Ag CS-NPs in colloidal solutions. Description of the spectra measurement and the results are presented following

4.2 UV-VIS-NIR Spectroscopy

UV-VIS-NIR spectroscopy measures the attenuation of a beam of light after passing through a sample (figure 32). The deuterium discharge lamp and the tungsten halogen lamp are applied as the light source for ultraviolet and near infrared spectral range. The wavelengths of these continuous light sources are split by a holographic grating in a single or double monochromator. The spectral bandpass is then determined by the monochromator slit width which is selected as 1nm in this study.

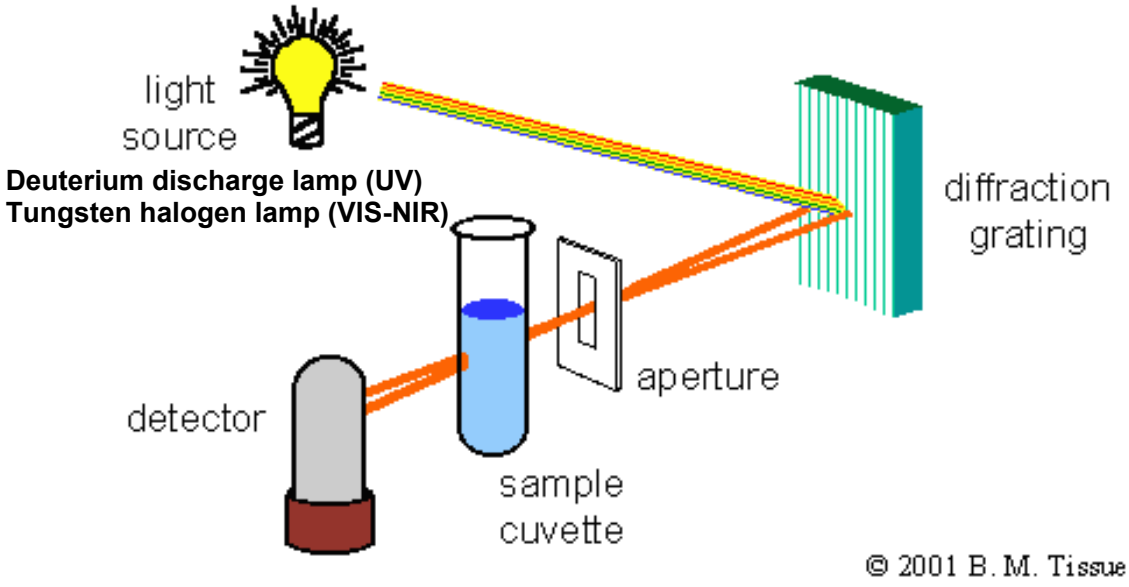

Figure 32. UV-VIS-NIR spectroscopy. After source light is passing through the grating, light is split by wavelength and passing through the slit (aperture) and sample. Arriving light is measured with detector.

Previous studies of the Au/SiO_2 and Ag/SiO_2 UV-VIS-NIR absorption spectra have been reported that two parameters affect the resonance peak shift on CS-NP. The first is the

Au (or Ag) filling ratio on the SiO_2 surface, and the second is the shell thickness. With the non-complete shell which does not fully cover the core, the gradual red shift was observed when the filling ratio of Au (or Ag) on the SiO_2 increases. Once the shell fully covers on the SiO_2 surface, a big red shift is observed. Then this shift reduces as shell become thicker [109-112]

Similar results are obtained in the current study. Figure 33 and 34 show the UV-VIS-NIR absorption spectra of single and CS-NPs of Au and Ag, respectively. ~4nm of red shift observed with SiO_2/Au CS-NP colloid compared with the single Au colloid. Also, the peak of SiO_2/Ag CS-NP colloidal solution presents ~7 nm of red shift compared with the single Ag colloid. Note that our Ag and Au shells do not fully cover the SiO_2 core as figure 35 and 36. Due to the incomplete shell structure, our CS-NPs do not provide significant big red shift, however, the peak shift with the similar filling rate are matched the trend determined from other groups [109, 113].

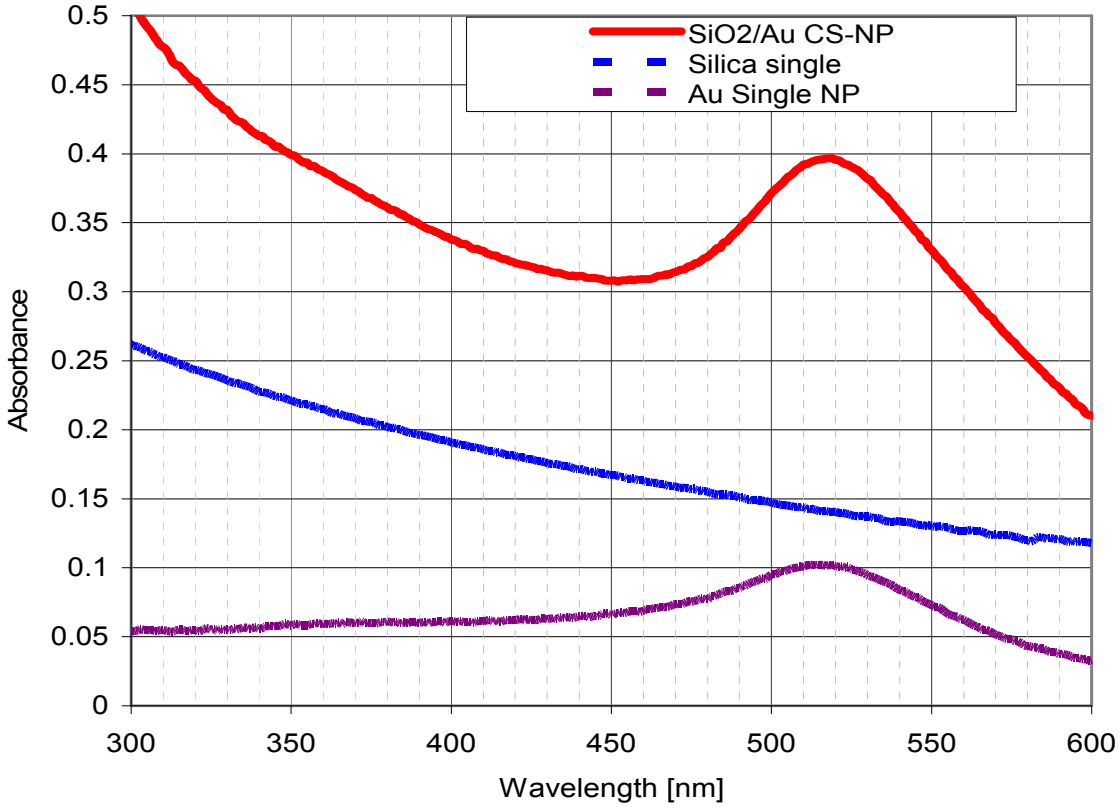

Figure 33. UV-VIS-NIR absorption spectra measured from SiO_2/Au CS-NPs colloid, Au colloid and SiO_2 colloid

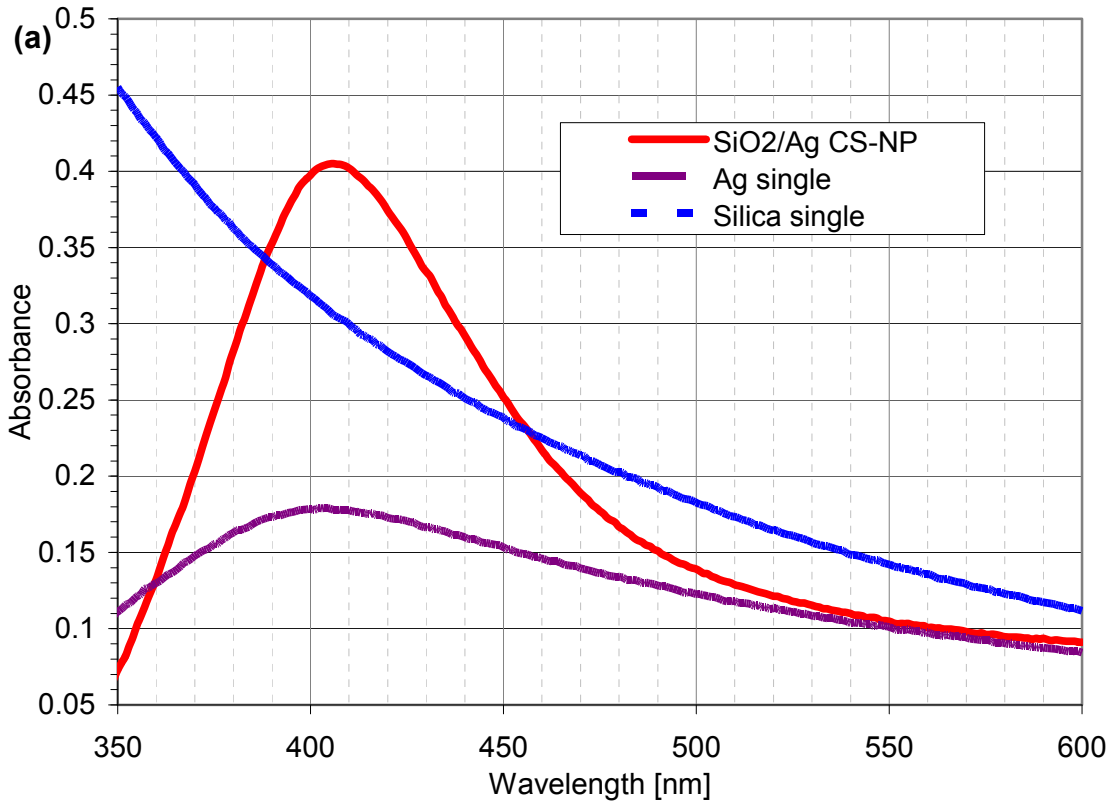

Figure 34. UV-VIS-NIR absorption spectra of SiO_2/Ag CS-NP and single Ag colloids.

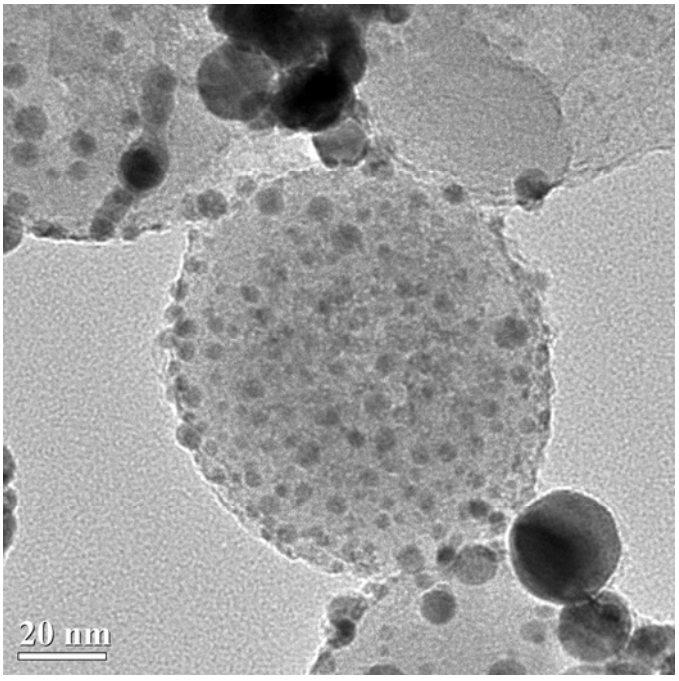

Figure 35. SiO_2/Au CS-NPs with 40 min of laser ablation. SiO_2 core is uniformly covered by gold clusters, but the shell is not fully completed

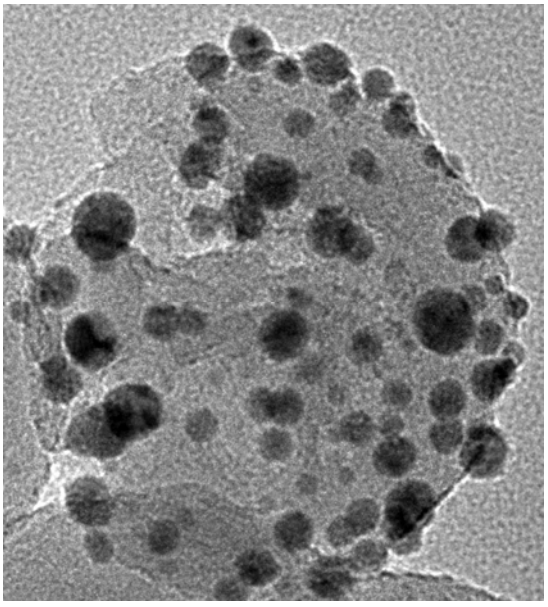

Figure 36. SiO_2/Ag CS-NP with 40 min of laser ablation. SiO_2 core is covered by silver clusters, but the shell is not fully completed

To better understand the measured optical property of the CS-NPs, electromagnetic field simulation is conducted by solving the Maxwell's equations directly. The analytical and numerical theoretical analyses applied to determine the absorption spectra of CS-NPs are presented following.

4.3 Analytical Theory Analysis

The light interaction with the spherical particle was introduced by Mie, in 1908 [114]. The classical electromagnetic theory describes the diffraction of a plane wave by a homogeneous sphere of arbitrary size and composition embedded in a homogeneous medium [88]. Later study expanded Mie theory to describe the single and core/shell structured particles [114-115].

4.3.1 Light attenuation by single NP and CS-NP in colloidal solution

According to Beer-Lambert law, the absorption of light which is traveling through the material can be related by absorbance, transmissivity and the material optical properties as follows.

$$A = \log_{10} T = \log_{10} \frac{I_0}{I} = \frac{NC_{ext} l}{2.303} \tag{4.1}$$

Where, A is an absorbance, T is transmissivity, I_0 and I are the intensity (or power) of the incident light and the transmitted light, N is the number of particles per unit volume, l is the light path length and C_{ext} is the extinction cross-section of a particle. The cross-section extinction includes the cross-section scattering and absorption as shown in equation 4.2.

$$C_{ext} = C_{sca} + C_{abs} \tag{4.2}$$

The corresponding scattering cross-section, C_{sca}, and absorption cross-section, C_{abs}, can be expressed as equation 4.3 and 4.4 calculated via the Poynting-vector determined from equation 5.10 in reference [105]

$$C_{sca} = \frac{k^4}{6\pi}|\alpha|^2 \tag{4.3}$$

$$C_{abs} = k\,\mathrm{Im}[\alpha] \tag{4.4}$$

where, α is the polarizability and $k = 2\pi/\lambda$. Assumed small sphere of sub-wavelength diameter in the electrostatic approximation, α can be derived as equation 4.5 for a single conducting nanoparticle (see figure 37(a)),

$$\alpha = 4\pi r^3 \frac{\varepsilon - \varepsilon_m}{\varepsilon + 2\varepsilon_m} \tag{4.5}$$

where, ε and ε_m are the dielectric functions of single nanoparticle and surrounding medium, r is the particle radius. In case of CS-NP as shown in figure 37(b), α can be expressed as equation 4.6 [105, 114]

$$\alpha = 4\pi r_S^3 \frac{(\varepsilon_S - \varepsilon_m)(\varepsilon_C + 2\varepsilon_S) + (r_C/r_S)^3(\varepsilon_C - \varepsilon_S)(\varepsilon_m + 2\varepsilon_S)}{(\varepsilon_S + 2\varepsilon_m)(\varepsilon_C + 2\varepsilon_S) + (r_C/r_S)^3(\varepsilon_C - \varepsilon_S)(2\varepsilon_S - \varepsilon_m)} \tag{4.6}$$

where, ε_c, ε_s, ε_m are dielectric functions of the core, shell materials and surrounding medium, r_c, r_s are core and shell radius. From this equation the polarizability of the homogeneous particle can be derived when $\varepsilon_c=\varepsilon_s$ and $R_c=R_s$.

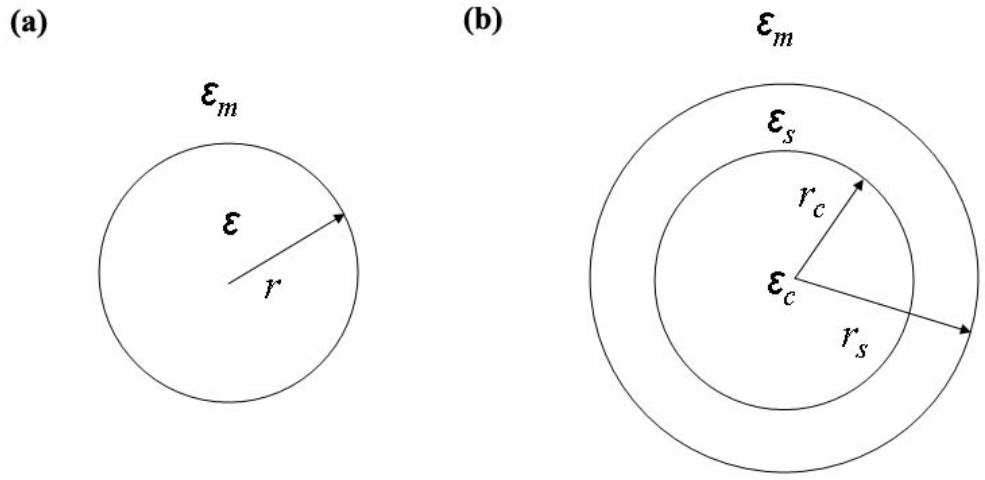

Figure 37. Schematics of (a) single NP, (b) CS-NPs and corresponding geometries and properties

In general, dielectric function, $\varepsilon(\omega) = \varepsilon_1(\omega) + i\varepsilon_2(\omega)$, is the complex function with angular frequency ω. The real and imaginary parts of the dielectric function determine the storage and loss of energy within a material under an electric field. Therefore the interaction of metal with the electromagnetic field can be explained with the specified real and imaginary of dielectric functions. Each real and imaginary part of the dielectric function represents the degree of material polarization by an external electromagnetic field with regard to the incident light and the optical losses such as absorption due to interband transitions or inelastic electron-phonon/electron-electron interactions, respectively [116]. At certain optical frequencies, ε can be experimentally determined via a reflectrometer studies or through the complex refractive index $\tilde{n}(\omega) = n(\omega) + i\kappa(\omega)$ of the medium. The complex refractive index and the complex dielectric constants are related as $\tilde{n}(\omega) = \sqrt{\varepsilon}$, and [105]

$$\varepsilon_1 = n^2 - \kappa^2 \tag{4.7}$$

$$\varepsilon_2 = 2n\kappa \tag{4.8}$$

$$n^2 = \frac{\varepsilon_1}{2} + \frac{1}{2}\sqrt{\varepsilon_1^2 + \varepsilon_2^2} \tag{4.9}$$

$$\kappa = \frac{\varepsilon_2}{2n} \tag{4.10}$$

where, n and κ refer to the refractive index and extinction coefficient, respectively. In the current study, n and κ can be obtained from tabulated data in handbook of optical constants of solids [117]. List of real and imaginary parts of dielectric function with different wavelength for Au and Ag are presented in table 5. Note that the real part of the dielectric function of Au and Ag are largely negative as towards the longer wavelength of the spectral range representing the strong scattering of light. The imaginary part of the dielectric function of Au is larger than Ag throughout the visible spectrum indicating the stronger light absorption can be achieved from Au compared with Ag.

The calculated extinction cross sections for single NP and CS-NPs are illustrated in figure 38. The resulting resonance peak shows big difference between the single NP and CS-NP. For a fair comparison, the size of single NP is selected to be the same as the outer diameter of CS-NP. For example, if 50 nm in diameter of Au core and 10 nm in thickness of SiO_2 shell is measured on CS-NP, 60 nm in diameter of single Au NP is examined for the resonance peak comparison. Also, shell thickness is varied with the fixed core (50 nm in diameter) for the extinction cross section of CS-NP calculation. Based on the calculation with equation 4.2-4.6, red-shift resonance peak is observed with CS-NP compared with the peak of single NP (c.f., figure 38(a) and (b)). As shell thickness decreases, the red shift of the resonance peak wavelength of CS-NP increases compared with single element NP with the same size. In addition to the red shift of the absorption spectra, calculated extinction cross section of both CS-NP and single NP highly depends on the particle size. As the size increases, the extinction cross section of both single NPs and CS-NPs increases.

Table 5. Refractive index, extinction coefficient, and dielectric constants of Au and Ag

Gold					Silver				
Λ (nm)	n	k	ε_1	ε_2	Λ (nm)	n	k	ε_1	ε_2
302	1.81	1.92	-0.4	6.96	302	1.5	0.88	1.46	2.64
310	1.83	1.92	-0.32	7.01	306	1.43	0.77	1.46	2.19
318	1.84	1.9	-0.24	7.01	310	1.32	0.65	1.33	1.71
326	1.82	1.88	-0.2	6.85	312	1.25	0.59	1.21	1.46
335	1.8	1.86	-0.23	6.69	314	1.15	0.54	1.03	1.24
344	1.77	1.85	-0.29	6.52	316	1.04	0.51	0.83	1.07
354	1.74	1.85	-0.39	6.43	318	0.93	0.5	0.61	0.94
365	1.72	1.86	-0.52	6.39	320	0.82	0.53	0.39	0.86
376	1.7	1.91	-0.76	6.47	322	0.71	0.57	0.18	0.8
388	1.67	1.94	-0.95	6.48	324	0.62	0.61	0.01	0.75
400	1.66	1.96	-1.08	6.49	326	0.53	0.66	-0.16	0.7
413	1.64	1.96	-1.16	6.41	331	0.37	0.81	-0.52	0.6
428	1.62	1.94	-1.15	6.27	332	0.32	0.9	-0.71	0.58
443	1.56	1.9	-1.19	5.95	335	0.29	0.99	-0.89	0.58
459	1.43	1.85	-1.37	5.26	340	0.26	1.12	-1.19	0.58
477	1.24	1.8	-1.68	4.46	344	0.24	1.24	-1.48	0.59
496	0.92	1.84	-2.55	3.37	354	0.21	1.44	-2.03	0.6
517	0.61	2.12	-4.12	2.58	365	0.19	1.61	-2.56	0.6
539	0.4	2.54	-6.29	2.04	376	0.2	1.67	-2.75	0.67
564	0.31	2.88	-8.2	1.76	388	0.19	1.81	-3.24	0.7
653	0.17	3.15	-9.89	1.05	400	0.17	1.95	-3.77	0.67
689	0.16	3.8	-14.41	1.22	413	0.17	2.11	-4.42	0.73
729	0.16	4.35	-18.9	1.43	428	0.16	2.26	-5.08	0.72
775	0.17	4.86	-23.59	1.69	443	0.16	2.4	-5.74	0.75
827	0.19	5.39	-29.02	2.03	459	0.14	2.56	-6.53	0.74
886	0.21	5.88	-34.53	2.47	477	0.13	2.72	-7.38	0.72
954	0.24	6.47	-41.81	3.05	496	0.13	2.88	-8.28	0.75
1033	0.27	7.07	-49.91	3.85	517	0.13	3.07	-9.41	0.8
1127	0.31	7.93	-62.79	4.95	539	0.13	3.25	-10.55	0.84
1240	0.37	8.77	-76.77	6.52	564	0.12	3.45	-11.89	0.83
1265	0.39	8.09	-65.3	6.29	590	0.12	3.66	-13.38	0.89
1291	0.4	8.25	-67.9	6.65	620	0.13	3.88	-15.04	1.02
					653	0.14	4.15	-17.2	1.16
					689	0.14	4.44	-19.69	1.24
					729	0.15	4.74	-22.45	1.4
					775	0.14	5.09	-25.89	1.46
					827	0.15	5.5	-30.23	1.6
					886	0.16	5.95	-35.38	1.94
					954	0.2	6.43	-41.31	2.55
					1033	0.23	6.99	-48.81	3.16
					1127	0.25	7.67	-58.77	3.85
					1240	0.33	8.49	-71.97	5.59
					1265	0.38	7.78	-60.39	5.84
					1291	0.38	7.92	-62.58	6.07

In order to explain the red shifted resonance peak with CS-NP, the real and imaginary part of polarizability is presented in figure 39 and 40. Note that the polarisability is the measure of the change in a molecule's electron oscillation in response to an applied electric field. As shown in figure 39(a), CS-NP presents much stronger polarizability than the single Au NP in both real and imaginary parts. This big difference can be explained with the origin of polarizability, which is determined by the coupled dielectric functions and the particle size. The polarizability of the single Au NP applied in the current study is determined by the coupled dielectric functions of two materials: Au and DI water. Since DI water is also an dielectric material with only real part dielectric constant. The light attenuation/absorption of the single element Au NP is mainly determined by Au and medium. However, in case of SiO_2/Au CS-NP, its polarizability is determined by the dielectric functions of the core material (SiO_2), shell material (Au) and the medium (DI water) as well as the core/shell size ratio. This coupled dielectric functions indicate that the electron oscillation of Au in CS-NP is strongly affected by core/shell geometry. Consequently, geometric/dielectric confined electron oscillation results in the big deviation of polarizability in CS-NP as shell thickness is changed. The polarizability directly contributes the absorption and scattering cross section through the particle as shown in equation 4.3. The calculation results of scattering and absorption cross section for single Au and SiO_2/Au CS-NP are shown in figure 39(b). Results indicate that the resonance peak of both scattering and absorption cross section are red shifted with CS-NP as shell thickness is decreased while the peak is not much changed with single NP with different sizes. Note that the peak shift is attributed by big deviation of imaginary and real part of polarizability with the core/shell geometry.

Similar results are obtained with Ag and is illustrated in figure 40. The polarizability of SiO_2/Ag CS-NP is also a strong function of shell thickness and provide red shift compared with pure Ag NPs. Compared with Au (figure 39(b)), Ag presents larger scattering cross section for both single NP and CS-NP as in figure 40(b). The real part of the dielectric function of silver is a large negative number especially towards the

longer wavelength of the visible spectrum, which causes strong scattering of light As explained in the previous section. The imaginary part of the dielectric function of silver is small throughout the visible spectrum indicating weak light absorption. Due to coupling with different interband transitions, light attenuation through Au and Ag also shows some differences at different wavelengths. Nevertheless, red shifts are observed in core shell structures of both Au and Ag.

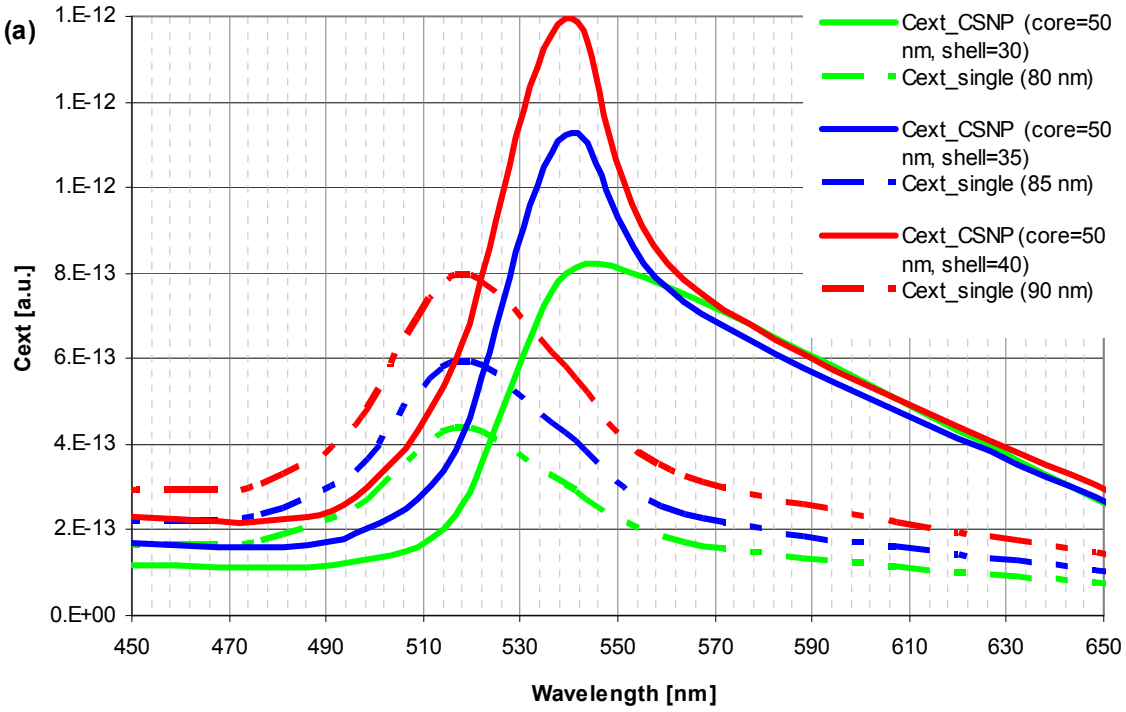

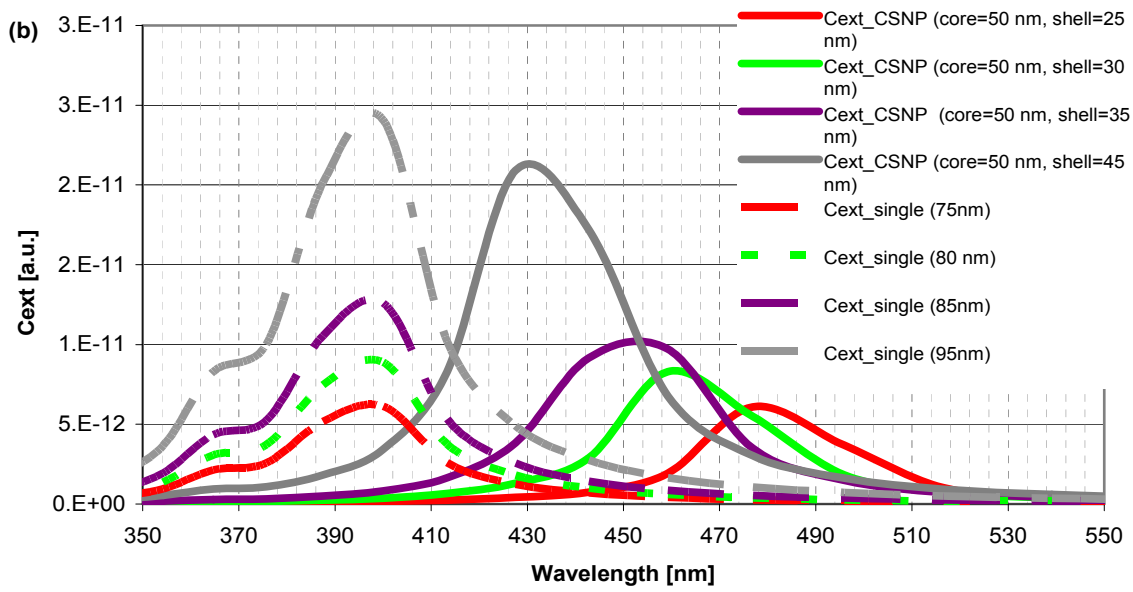

Figure 38. Calculated extinction cross sections of (a) Au single NP and SiO_2/Au CS-NP with different shell thickness, (b) Ag single NP and SiO_2/Ag CS-NP with different shell thickness

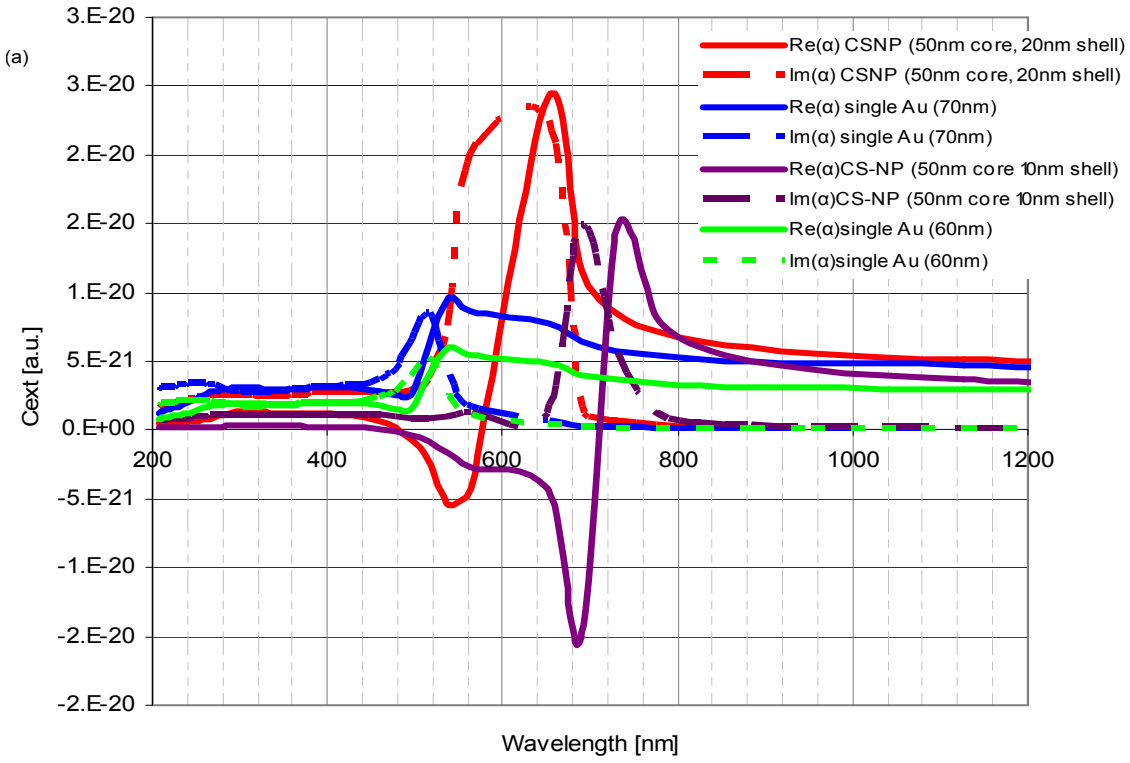

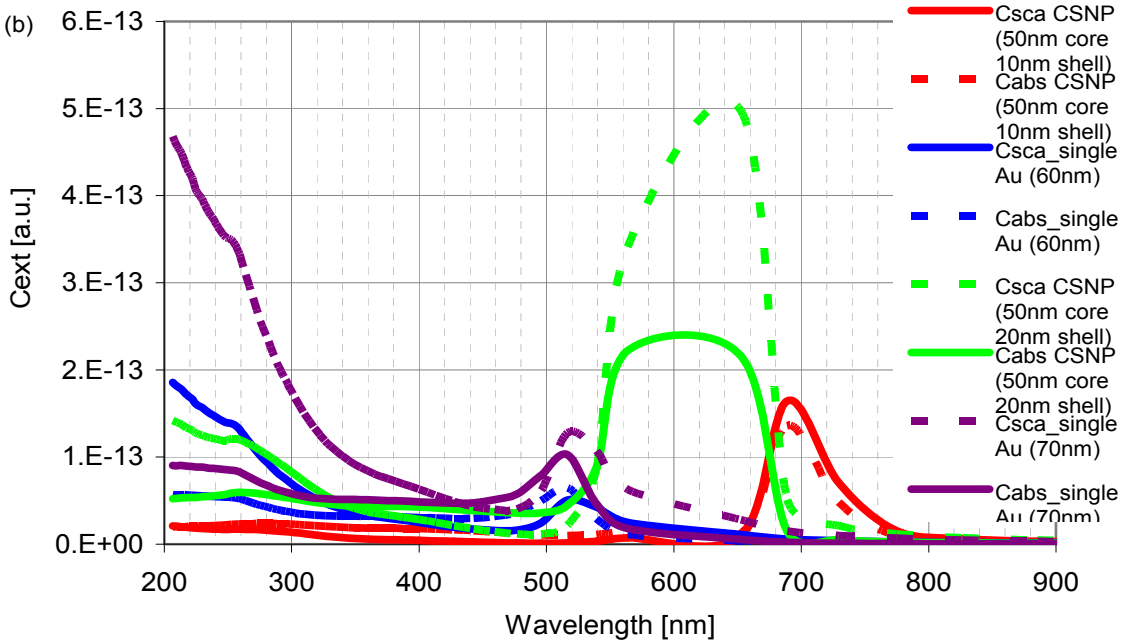

Figure 39. (a) Imaginary and real part of polarizability of Au NP and SiO_2/Au CS-NP with 10 and 20 nm thickness. (b) Absorption cross sections and scattering cross sections of Au NP and SiO_2/Au CS-NP with different sizes.

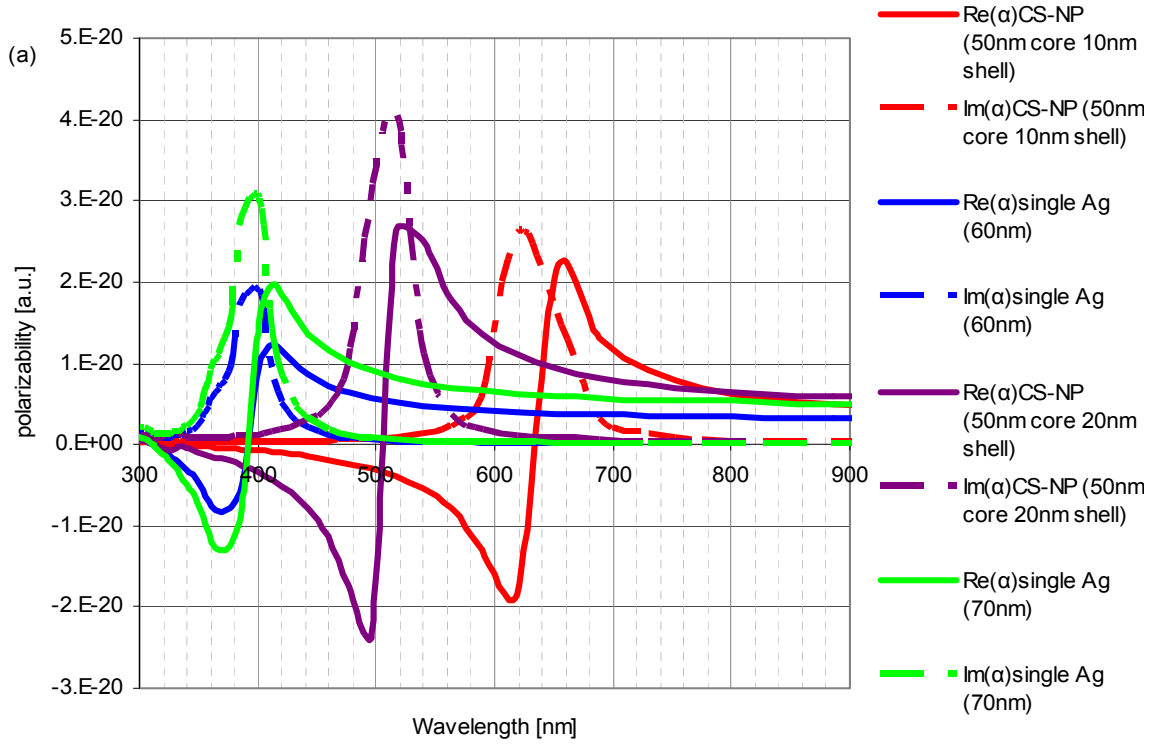

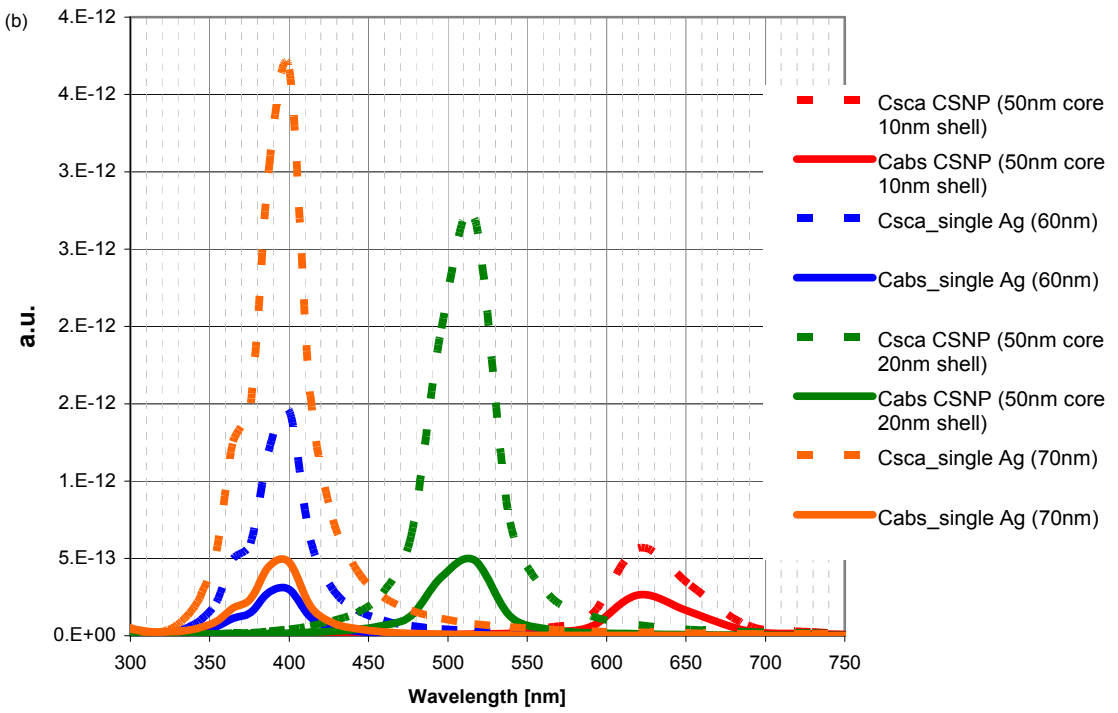

Figure 40. (a) Imaginary and real part of polarizability of Ag NP and SiO_2/Ag CS-NP with 10 and 20 nm thickness. (b) Absorption cross sections and scattering cross sections of Ag NP and SiO_2/Ag CS-NP with different sizes.

4.4 Electromagnetic (EM) Field Simulation

The response of a nanoparticle to an uniform static electric field of UV to IR wavelengths can be described with dipole moment of the particle. The dipole moment is the measure of the electrical polarity induced by assigned electro-magnetic field as expressed in equation 4.11

$$P = \varepsilon_m \alpha E_0 \tag{4.11}$$

where, E_0 is an assigned static field around the nanoparticle and α is polarizability defined in equation 4.5 and 4.6. Note that the dipole moment is induced by the induced oscillation of free electrons in response to the surrounding electro-magnetic field. which can directly affect the scattering of incident light from the nanoparticle. Compared with

pure nanoparticles, the polarizabiliy of CS-NPs is strongly affected not only by the material composition but also the geometry of the CS-NPs. It is indicated in the measurement of the previous section that the peak resonance of extinction cross section and the corresponding polarizability and dipole moment change with shell thicknesses of the CS-NPs, which is an important geometric factor of CS-NPs. In this section, 3D electromagnetic (EM) field simulation is performed to examine the local field enhancement around nanoparticles, which is also determined by the polarizabiliy of nanoparticle. Larger local field enhancement which corresponds to larger real part of the polarizability, generally speaking, corresponds to large absolute value of the polarizabiliyt which is the parameter determining the attenuating of light passing through nanoparticles as studied in the last section

4.4.1 Electromagnetic (EM) Field Simulation using COMSOL

A $0.8 \times 0.8 \times 1\ \mu m$ domain is applied to simulate the EM field distribution. A single NP or CS-NP is located at the center of frequency domain with a 40 nm core radius and t a 10 or 20 nm shell thicknesses. The configuration of applied geometry is shown in figure 41. Laser frequency is swapped from 4.1E15 Hz (729 nm in wavelength) to 8.9E15 Hz (335 nm) in the simulation. Plane waves are propagating through the z direction, and free tetrahedral mesh is applied as shown in figure 42. The required dielectric constant of Au, silica and DI water for the 3D simulation are from empirical tabulated data (refractive index, extinction coefficient) of ref 117[117] utilizing equation 4.7 and 4.8.

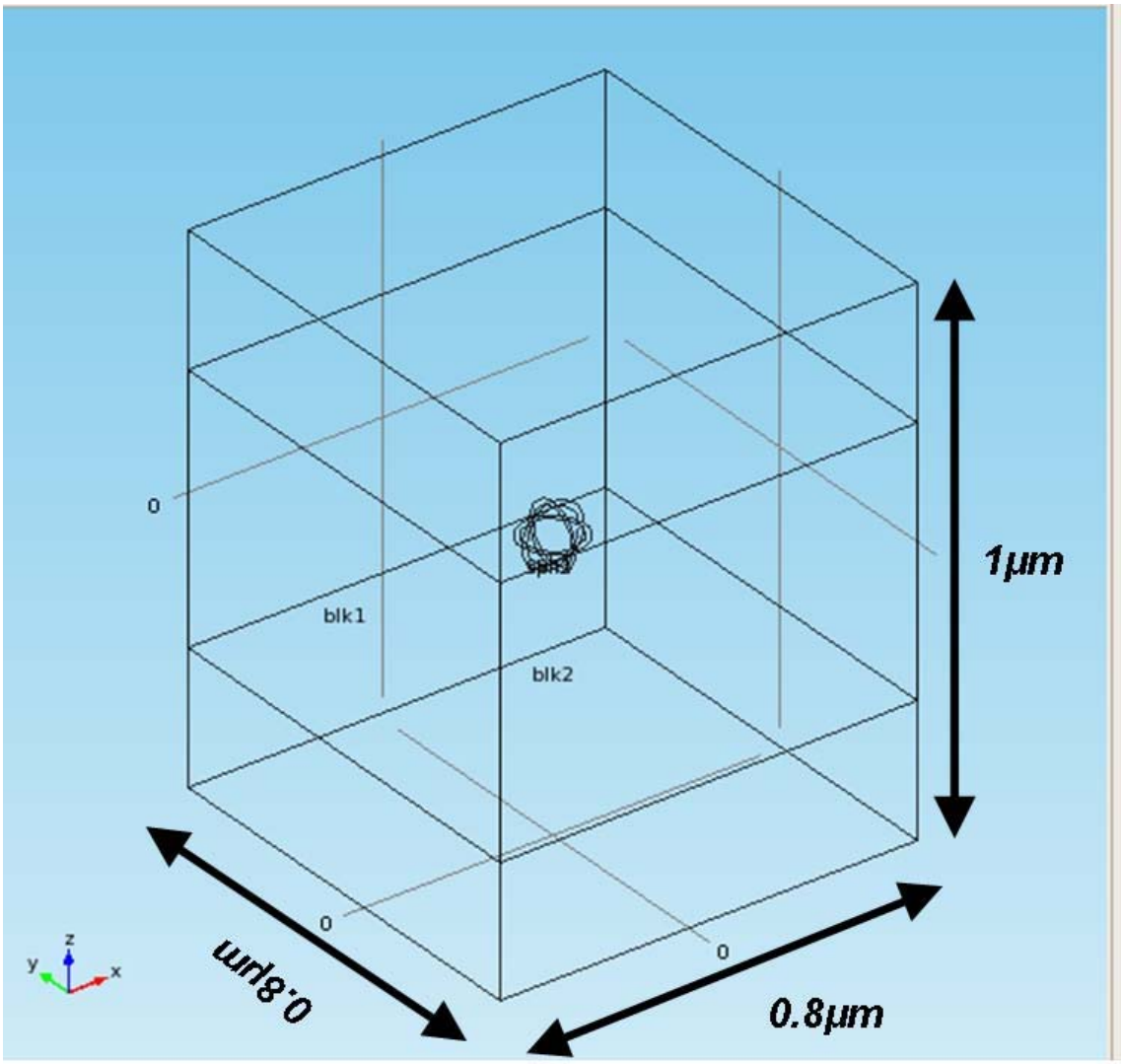

Figure 41. Configuration of the simulation domain in COMSOL software

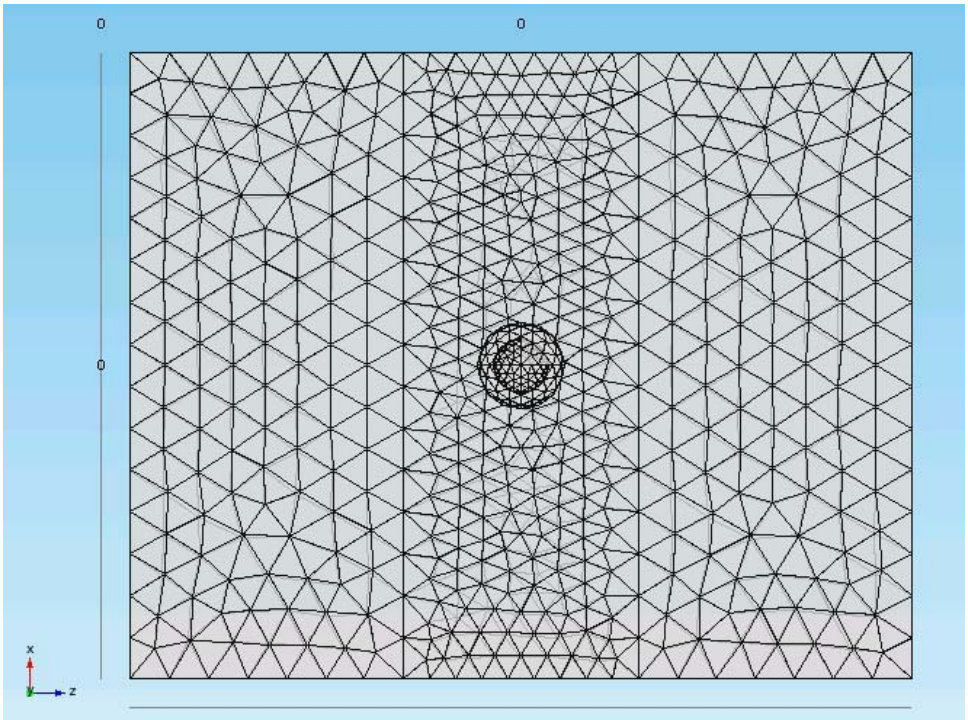

Figure 42. Applied. tetrahedral meshes in the 3D EM simulation with finite element method.

A zoomed in figure of nanoparticles placed at the center of the simulation domain as in figure 42 is illustrated in figure 43. The electric field vector of the entire domain can be simplified as following [105]

$$\nabla^2 \vec{E} = \mu_0 \varepsilon_0 \frac{\partial^2 \vec{E}}{\partial t^2} \tag{4.12}$$

Further, initial and boundary conditions are followed as

$$\begin{aligned} &t = 0, \quad \vec{E} = \vec{E}_0 \\ &r \to \infty, \quad \vec{E} \to \vec{E}_0 e^{-iwt} \\ &r = a, \quad \vec{n} \cdot (\vec{E}_s - \vec{E}_c) = 0, \quad \vec{n} \times (\vec{E}_s - \vec{E}_c) = 0 \\ &r = b, \quad \vec{n} \cdot (\vec{E}_{amb} - \vec{E}_s) = 0, \quad \vec{n} \times (\vec{E}_{amb} - \vec{E}_s) = 0 \end{aligned} \tag{4.13}$$

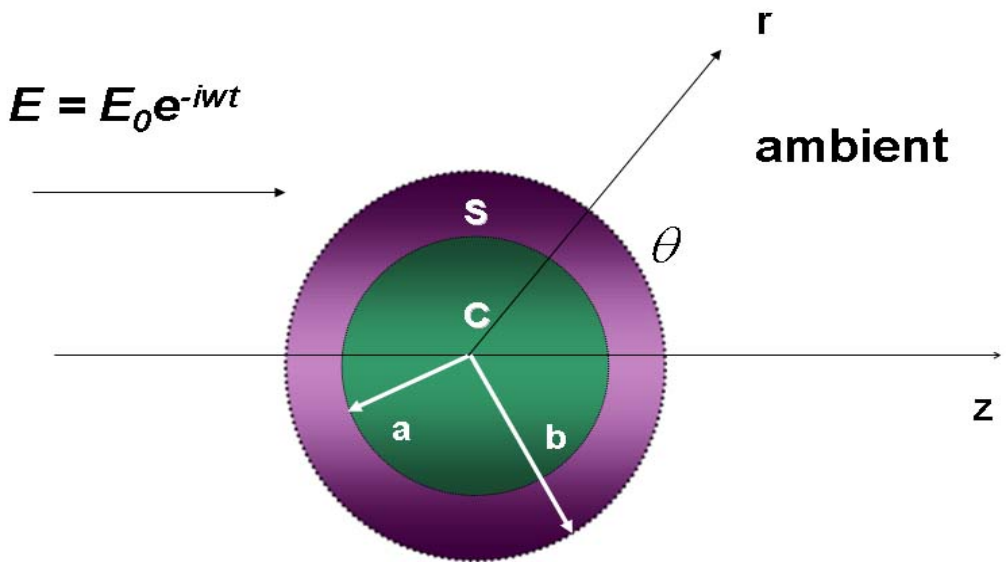

Figure 43. Geometric configuration of nanoparticle in the 3D EM simulation.

The obtained electric field distributions from solving equation41 with a commercial finite element platform (COMSOL 4.0a) are shown in figure 44-46. The color rendering of the obtained electric field intensity is unified in all simulations. The maximum electric field is illustrated figure 47. It is observed that the maximum E-field around the CS-NP is stronger than that of the single NP when λ >~500nm. Also, the electric field is enhanced as the shell thickness increases as illustrated in figure 47. Based on the simulation, the resonance peak is at ~516 nm for pure Au nanoparticles. For SiO2/Au CS-NPs, the stronger resonance peak shifts toward 729 nm. The electric field around the CS-NPs at λ=729 nm becomes stronger as shell thickness increases. The red shift and enhancement of the electric field enhancement around larger CS-NP compared with the pure nanoparticle in the simulation indicates the real portion of the polarizabiliy becomes larger and shifts toward longer wavelengths when pure nanoparticles are replaced with the CS-NPs. The trend of the change of the real portion of the polarizabiliy between pure and CS-NPs suggests the similar trend of the change of the absolute value of the polarizability which was observed experimentally in the last section.

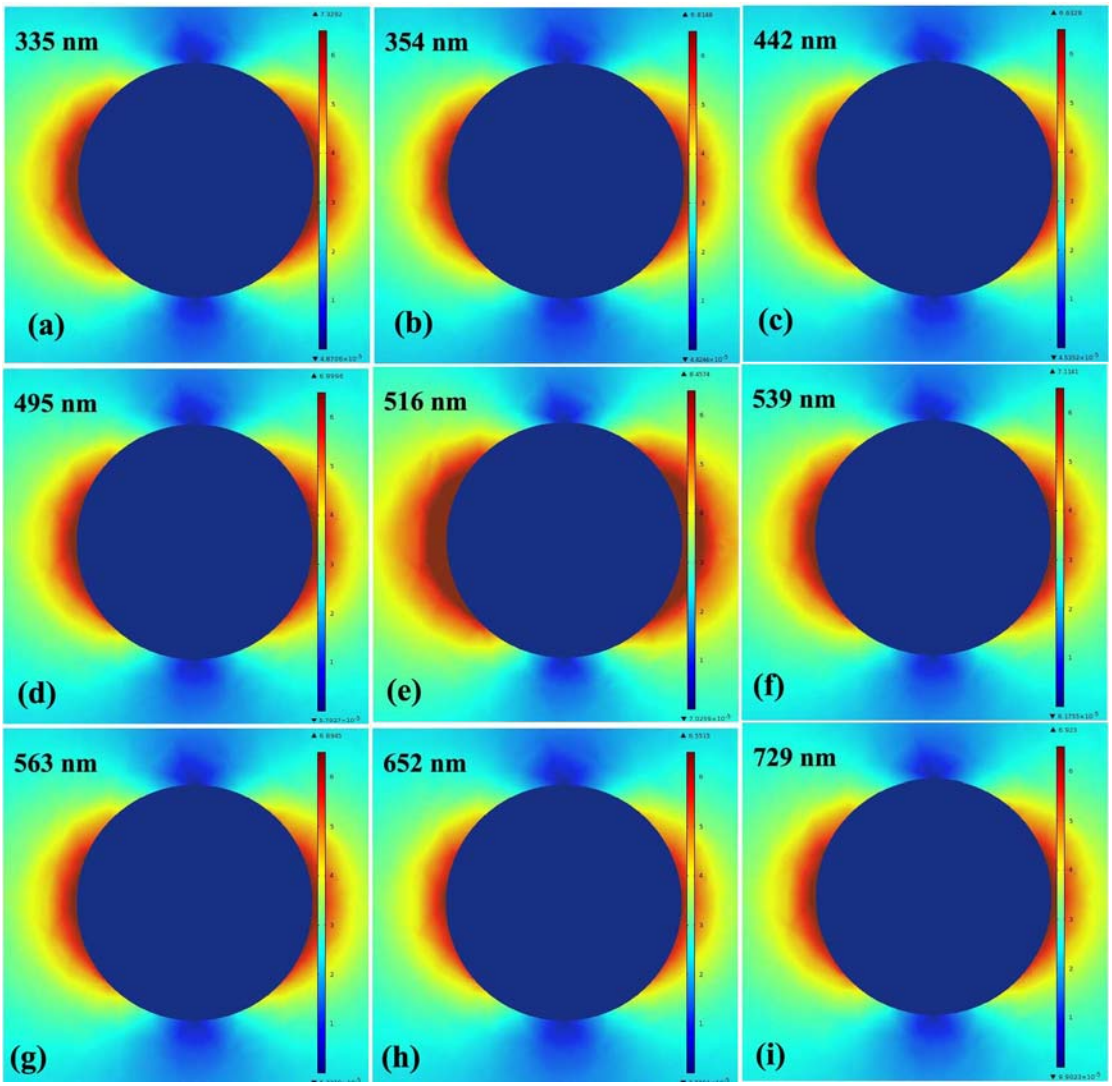

Figure 44. EM simulation result of 40nm single Au NP. The incident light is from the top of each figure.

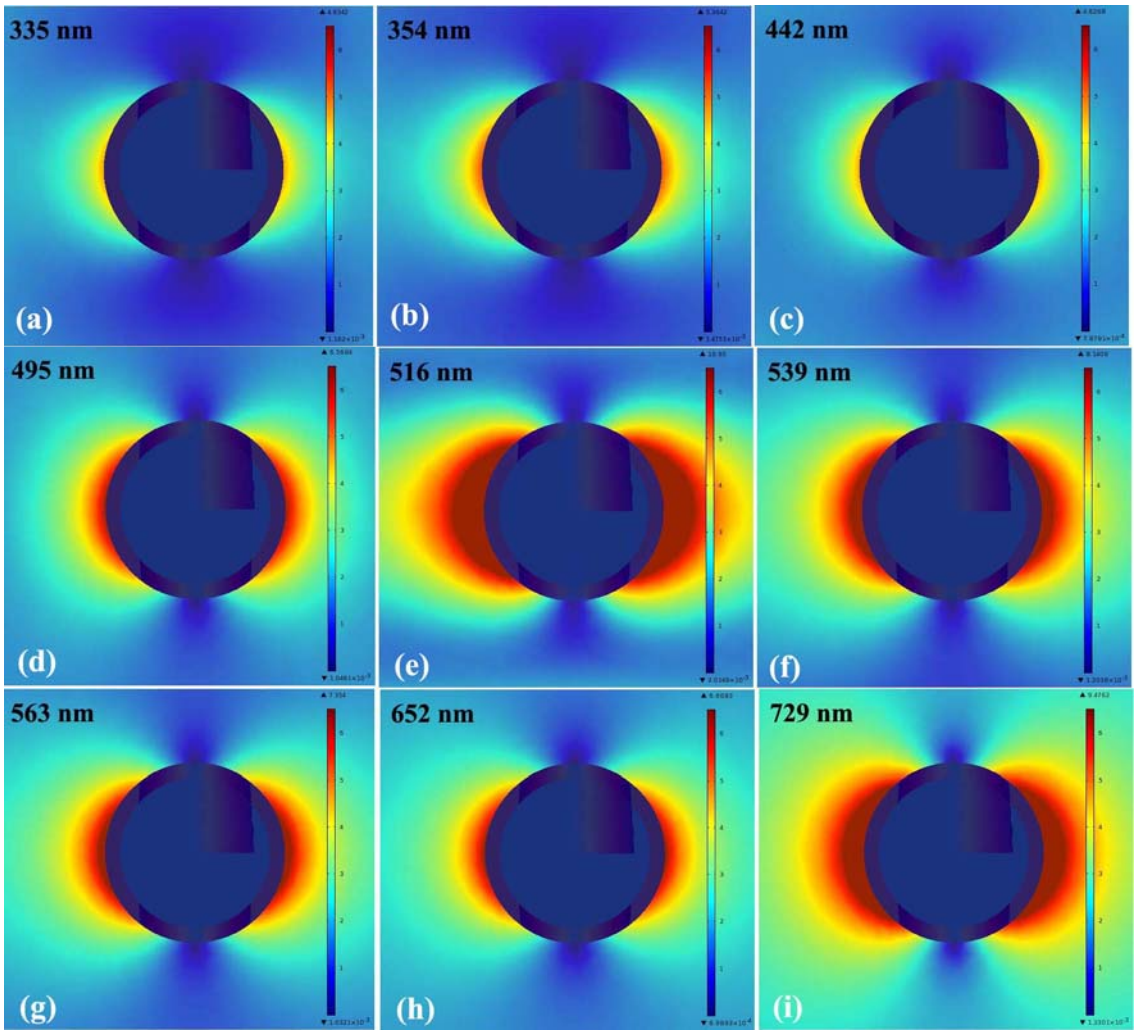

Figure 45. EM simulation result of SiO_2/Au CS-NP (10nm of shell thickness). The incident light is from the top of each figure.

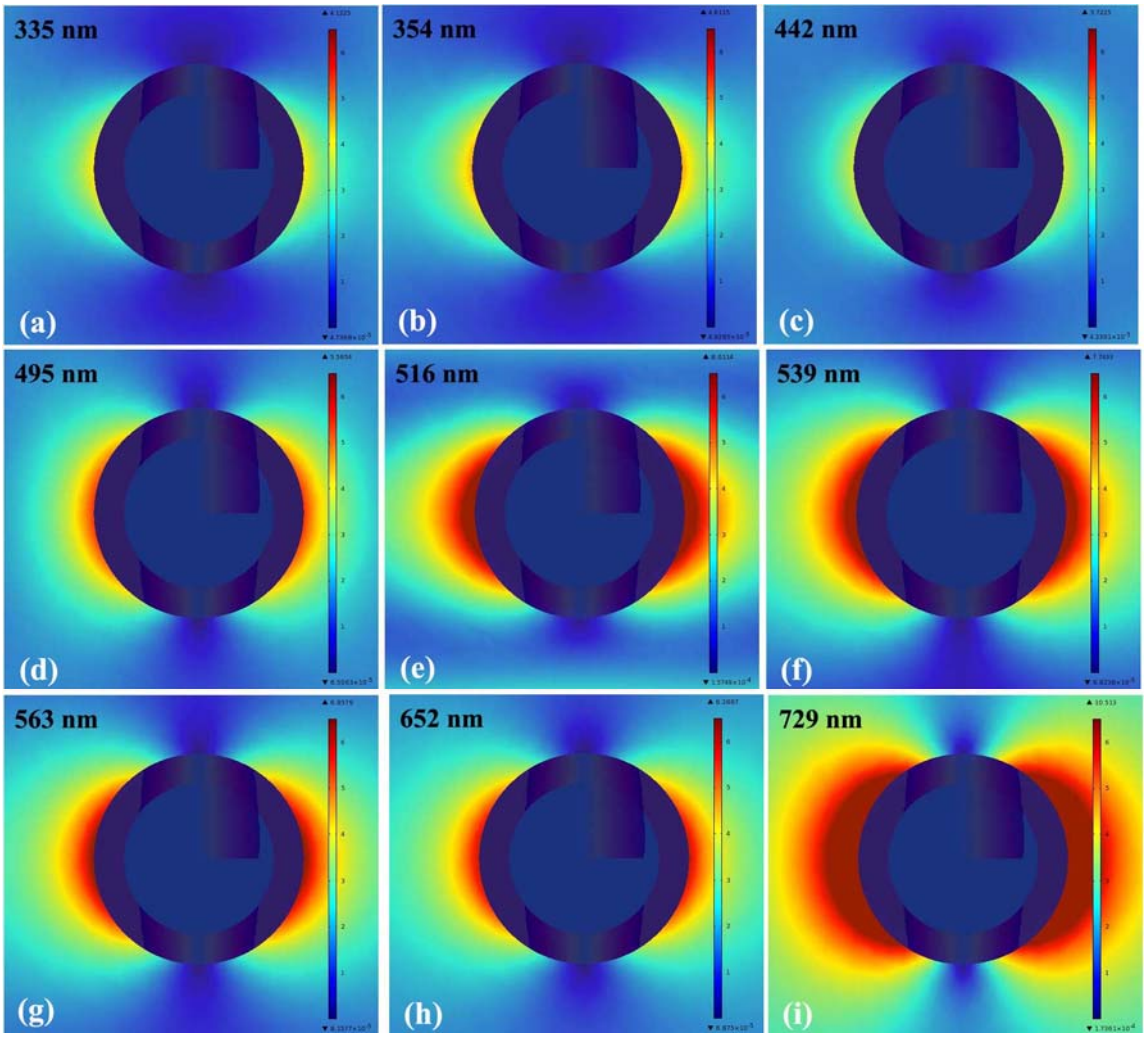

Figure 46. EM simulation result of SiO_2/Au CS-NP (20nm of shell thickness). The incident light is from the top of each figure.

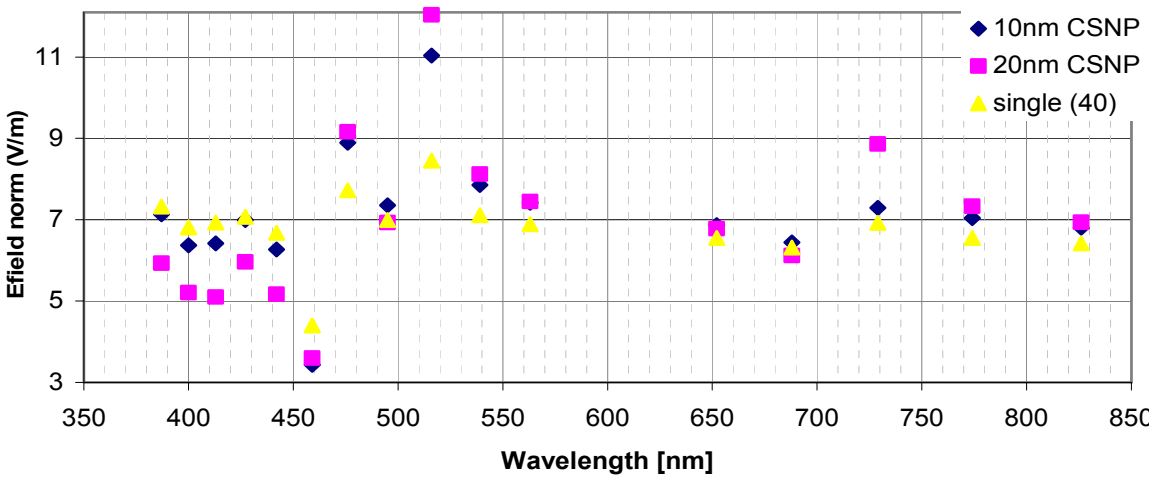

Figure 47. Comparison of electric field around nanoparticles of different configurations (40 nm pure Au particle, SiO_2/Au CS-NPs with 10 and 20 nm of shell thickness)

4.5 Summary

In this portion of study, theoretical and experimental optical properties of CS-NPs are presented. From the examination, absorption spectra of the resulting Ag and Au CS-NPs are measured with UV-VIS-NIR spectroscopy. The shift of the absorption peak is explained with the plasmon resonance as a function of the shell thickness and shell coverage. In order to visualize the localized surface plasmon resonance around the single NP and CS-NP, Electric field simulation is performed.

The absorption peak of single NP and CS-NP with Au and Ag is first determined theoretically with Beer lambert law and Mie theory. In order to find the absorption resonance peak, the extinction cross section of single NP and CS-NP are calculated. Due to different localized surface plasmon modes, calculation results show that Ag(Au)/SiO_2 CS-NP always provides red shifted compared with the single element Ag(Au) NP. In addition, the amount of red shift is proportional to the shell thickness of the CS-NPs.

The optical characteristics of resulting single NP and CS-NPs (Ag and Au) generated from laser ablation in colloidal solution as described in chapter 4.2 are also experimentally examined with the UV-VIS-NIR spectroscopy. Small red shift was observed with CS-NPs in the UV-VIS-NIR absorption spectra. In the smaller red shift compared with the theoretical prediction can be attributed to the poor shell coverage on the SiO_2 core for the examined Au/SiO_2 and Ag/SiO_2 CS-NPs. Since Ag an Au have less adhesion energy on the SiO_2 surface and small light absorption with our current laser condition, the shell quality is poor on the SiO_2. As a result, the strong red shift owing to the strong plasmon resonance in the perfectly coated CS-NPs used in the theoretical analysis does not fully represented in the experimental measurements with the UV-VIS-NIR spectroscopy.

Visualization of near field enhancement through CS-NP (and single NP) which directly relate the light absorption with NPs is also performed with a electric field simulation by solving Maxwell's equations with finite element method. Based on the simulation, stronger dipole moment (E-field) is generated on the particles in the normal direction of the incident light. The amount of enhancement is proportional to the shell thickness of the CS-NPs. The observation field enhancement and red shift of the absorption peak of the CS-NPs can be understood with the size dependency of localized plasmon resonance on the CS-NPs.

5. CONCLUSIONS AND FUTURE RESEARCH

5.1 Conclusions

Core/Shell Nanoparticls (CS-NPs) have attracted a significant attention from the last few decades owing to its unique capability in tuning the optical, chemical and magnetic properties to the desired conditions compared to traditional nanoparticles (NPs). Most of the existing CS-NPs generation approaches are associated with chemical methods which are optimized for the generation of single element NPs and involve with by-products such as hazard solvents which are not eco-friendly. As a result, physical methods for the generation of CS-NPs have been developed in the recent decade in order to solve the disadvantages involved with chemical methods. In this study, novel CS-NPs generation techniques with laser ablation are studied. Laser ablation has been widely accepted in material processing owing to its applicability for almost all materials and relatively fast processing speed compared with other methods. Two types of CS-NPs generation with laser ablation are studied in my PhD. research, namely, double pulse laser ablation and laser ablation in colloidal solutions. The optical properties of obtained CS-NPs are characterized experimentally and theoretically with the UV-VIS-NIR spectroscopy and electromagnetic (EM) field simulation respectively.

In the first part of this study, a sequence of double pulse laser ablation is applied on two adjacent samples to generate core/shell nanoparticles (CS-NPs). The condensation of the vapor plume from the first ablation forms the cores of the CS-NPs, which allow heterogeneous nucleation of the followed vapor plume of the second ablation on the shell material. Through properly control the experimental conditions such as the laser energy, delay time and the material combinations, we have successfully demonstrated the generation of CS-NPs. CS-NPs of Sn/Glass, Zn/Glass, Zn/Si, Ge/Si, Cu/Zn with this first scheme. It was found that the success of generation of CS-NPs with the double pulse scheme relies on the compatibility of the two selected target material along with

the experimental conditions during laser ablations. Key factors affecting the generation of CS-NPs with the double pulse laser ablation scheme and are examined in this study include; (1) surface tensions of the constructing materials and the associated Gibbs free energy of the CS-NPs, (2) contribution of background gases (i.e., He and Ar), (3) contribution of delay time between two laser pulses, and (4) contribution of the laser energy. CS-NPs can be successfully generated when the Gibbs free energy of the formation of CS-NP is lower than that for the formation of separated single component nanoparticles of the core and the shell material when two vaporized material are mixed together. In addition on the material compatibility, to successfully generate CS-NPs from double pulse laser ablation, the delay time between two lasers and the separation distance between the two targets should be precisely controlled to achieve the maximum mixing of the condensed core particles with the vaporized shell material from the second laser pulse. The diameter of the core of the CS-NPs can be increased through reducing the thermal conductivity of the background gas (e.g., replacing He with Ar) along with increasing the laser energy applied to ablated the core material.

The second scheme examined for the generation of CS-NPs is through laser ablation of solid targets in colloidal solutions. With an appropriate laser energy and ablation time, the ablated vapor plume from the solid target in the colloidal solution can deposit on the colloids and forms CS-NPs. Compared with the double pulse laser ablation, this second method provides easier control of the size and shape of the core of the CS-NPs along with higher productivity of CS-NPs with desired size and material combinations. Two colloidal solutions, namely, Au and SiO_2 colloidal solution are applied in the CS-NPs generation with the second scheme. Compared with the double pulse ablation, the second scheme has no explicit restriction of the compatibility between the core and shell material based on the experimental results and the Gibb's free energy analysis. Key factors affecting the formation of CS-NPs with the second scheme and are examined in this research includes the effect of (a) shell material, (b) core size and (c) the duration of laser ablation. Results show that Cu, compared with Sn, Au and Ag, provides smooth

and uniform shell structures when SiO_2 core was applied. The much better shell structure with Cu can be attributed to the extremely high adhesion energy between Cu and SiO_2 compared with other material examined. It is found that the shell formation is not strongly affected by core size in the current study when the core diameter is >~100 nm. The obtained shell thickness depends on the amount of ablation time. Thicker shell can be obtained with longer ablation time of the solid target in the colloidal solution.

The absorption spectra of resulting CS-NPs are experimentally and theoretically studied with UV-VIS-NIR spectroscopy and full wave electrodynamics analysis. Red shift of absorption peak occurs in both SiO_2/Au and SiO_2/Ag colloids compared with pure nanoparticles (NPs) of Au and Ag respectively. The amount of red-shift is sensitive to the shell condition and thickness of the CS-NPs. Poor coverage of the shell material corresponds to smaller red shift of the observed CS-NPs in the UV-VIS-NIR absorption spectra. In addition, the larger shell thickness also induces smaller red shift of the observed CS-NPs in the UV-VIS-NIR absorption spectra. The red shift is reproduced with the full wave analysis with finite element method under the same conditions. Visualization of near field enhancement through CS-NP (and single NP) is achieved with the 3D visualization of the commercial finite element package (COMSOL 4.0a). Based on the theoretical analysis, the strength of the localized surface plasmon resonance (dipole moment) is proportional to the shell thickness. As the experimental result, the amount of red shift of the absorption peak, however, is inversely proportional to the shell thickness. Based on the theoretical analysis, the red shift can be attributed to the additional surface plasmon resonance at the interface of metal/dielectric of the CS-NPs. Through adjusting the material and size combination of the core and shell of the CS-NPs, red shift of the absorption peak of the CS-NPs can be achieved within a limit range (~10-100 nm) around the intrinsic absorption peak of the metal of the CS-NPs. The freedom of adjusting the absorption peak of CS-NPs in favorable in bio and optical applications when specified absorption peak of fixed wavelength is desired.

5.2 Future Research

The current study can be extended for the generation of multi-layered CS-NPs by applying multiple laser ablation on different solid targets in the colloidal solution. The resulting NP is then covered with multiple shell of material from the multiple ablated targets (i.e., multiple-layered NP). The multi-layered CS-NPs with metal and dielectric materials can be applied as wide band plasmonic material with appropriate combination of the dielectric constants of the shell materials. These specially designed multi-layered CS-NPs can be important in bio-sensing, sub-diffraction limit, and single molecule detection as well as the construction blocks of plasmonic devices. To precisely construct the desired multi-layered CS-NPs with the designed parameters, the following factors should be studied in the future.

a. The ablation efficiency of solids and resulting plume dynamics in immersed liquids as functions laser conditions, material properties and liquid conditions
b. The interaction of ablated materials on the multi-layered NP during the formation of additional shells
c. The effective approached to extract the resulting CS-NPs from the liquid environment without causing additional reactions (e.g., oxidation of the shell material)

REFERENCES

[1] M. A. Gondal, T. A. Saleh, and Q. A. Drmosh, "Synthesis of nickel oxide nanoparticles using pulsed laser ablation in liquids and their optical characterization," *Applied Surface Science,* vol. 258, pp. 6982-6986, Jul 2012.

[2] P. R. Willmott and J. R. Huber, "Pulsed laser vaporization and deposition," *Reviews of Modern Physics,* vol. 72, pp. 315-328, Jan 2000.

[3] G. W. Yang, "Laser ablation in liquids: Applications in the synthesis of nanocrystals," *Progress in Materials Science,* vol. 52, pp. 648-698, 2007.

[4] B. E. Naes, "Elemental analysis of glass and ink by laser ablation inductively coupled plasma mass spectrometry (LA-ICP-MS) and laser induced breakdown spectroscopy (LIBS)," Ph.D. 3380834, Florida International University, Miami, 2009.

[5] K. Sugioka, *Laser Precision Fabrication*, First ed. New York: Springer, 2010.

[6] S. Sakabe, K. Shirai, M. Hashida, S. Shimizu, and S. Masuno, "Skinning of argon clusters by Coulomb explosion induced with an intense femtosecond laser pulse," *Physical Review A,* vol. 74, p. 043205, Oct 2006.

[7] A. Bogaerts, Z. Y. Chen, R. Gijbels, and A. Vertes, "Laser ablation for analytical sampling: what can we learn from modeling?," *Spectrochimica Acta Part B-Atomic Spectroscopy,* vol. 58, pp. 1867-1893, Nov 2003.

[8] A. V. Goncharenko, "Optical properties of core-shell particle composites. I. Linear response," *Chemical Physics Letters,* vol. 386, pp. 25-31, Mar 2004.

[9] S. Yang, H. Wang, W. Fu, and D. F. Kelley, "The synthesis and optical properties of GaSe/InSe core/shell nanoparticles," *Journal of Photochemistry and Photobiology A: Chemistry,* vol. 192, pp. 159-165, 2007.

[10] E. Gyorgy, A. P. del Pino, A. Giannoudakos, M. Kompitsas, and I. N. Mihailescu, "Tunable optical properties of laser grown double-structures with gold nanoparticles and zinc oxide thin films," *Physica Status Solidi a-Applications and Materials Science,* vol. 205, pp. 1978-1982, Aug 2008.

[11] H. Zeng, Z. Li, W. Cai, B. Cao, P. Liu, and S. Yang, "Microstructure control of Zn/ZnO core/shell nanoparticles and their temperature-dependent blue emissions," *Journal of Physical Chemistry B,* vol. 111, pp. 14311-14317, Dec 2007.

[12] F. Hubenthal, T. Ziegler, C. Hendrich, M. Alschinger, and F. Trager, "Tuning the surface plasmon resonance by preparation of gold-core/silver-shell and alloy nanoparticles," *European Physical Journal D,* vol. 34, pp. 165-168, Jul 2005.

[13] C. J. O'Connor, J. A. Sims, A. Kumbhar, V. L. Kolesnichenko, W. L. Zhou, and J. A. Wiemann, "Magnetic properties of FePtx/Au and CoPtx/Au core-shell nanoparticles," *Journal of Magnetism and Magnetic Materials,* vol. 226-230, pp. 1915-1917, 2001.

[14] T. Seto, H. Akinaga, F. Takano, K. Koga, T. Orii, and M. Hirasawa, "Magnetic properties of monodispersed Ni/NiO core-shell nanoparticles," *Journal of Physical Chemistry B,* vol. 109, pp. 13403-13405, Jul 2005.

[15] N. V. Long, T. D. Hien, T. Asaka, M. Ohtaki, and M. Nogami, "Synthesis and characterization of Pt-Pd alloy and core-shell bimetallic nanoparticles for direct methanol fuel cells (DMFCs): Enhanced electrocatalytic properties of well-shaped core-shell morphologies and nanostructures," *International Journal of Hydrogen Energy,* vol. 36, pp. 8478-8491, Jul 2011.

[16] S. Alayoglu, A. U. Nilekar, M. Mavrikakis, and B. Eichhorn, "Ru-Pt core-shell nanoparticles for preferential oxidation of carbon monoxide in hydrogen," *Nat Mater,* vol. 7, pp. 333-338, Mar 2008.

[17] J. L. Arias, M. Lopez-Viota, M. A. Ruiz, J. Lopez-Viota, and A. V. Delgado, "Development of carbonyl iron/ethylcellulose core/shell nanoparticles for biomedical applications," *International Journal of Pharmaceutics,* vol. 339, pp. 237-245, Jul 2007.

[18] H. L. Duan, Y. Jiao, X. Yi, Z. P. Huang, and J. Wang, "Solutions of inhomogeneity problems with graded shells and application to core-shell

nanoparticles and composites," *Journal of the Mechanics and Physics of Solids,* vol. 54, pp. 1401-1425, Jul 2006.

[19] Z. H. Li, K. M. Wang, W. H. Tan, J. Li, Z. Y. Fu, Y. L. Wang, J. B. Liu, and X. H. Yang, "Preparation of luminescent CdTe quantum dots doped core-shell nanoparticles and their application in cell recognition," *Chinese Science Bulletin,* vol. 50, pp. 1703-1707, Aug 2005.

[20] R. Thakar, Y. C. Chen, and P. T. Snee, "Efficient emission from core/(doped) shell nanoparticles: Applications for chemical sensing," *Nano Letters,* vol. 7, pp. 3429-3432, Nov 2007.

[21] P. W. Mauriz, M. S. Vasconcelos, and E. L. Albuquerque, "Surface plasmon-polaritons' contribution to the specific heat of quasiperiodic GaAS/SiO2 structures," *Surface Science,* vol. 482, pp. 537-539, Jun 2001.

[22] K. S. Oh, K. E. Lee, S. S. Han, S. U. H. Cho, D. Kim, and S. H. Yuk, "Formation of core/shell nanoparticles with a lipid core and their application as a drug delivery system," *Biomacromolecules,* vol. 6, pp. 1062-1067, Mar-Apr 2005.

[23] N. Sounderya, and Yong Zhang, "Use of Core/Shell Structured Nanoparticles for Biomedical Applications," *Recent Patents on Biomedical Engineering* vol. 1.1, pp. 34-42, 2010.

[24] A. M. F. Garcia, M. S. F. Fernandes, and P. J. G. Coutinho, "CdSe/TiO(2) core-shell nanoparticles produced in AOT reverse micelles: applications in pollutant photodegradation using visible light," *Nanoscale Research Letters,* vol. 6, Jun 2011.

[25] J. H. Son, H. Y. Park, D. P. Kang, and D. S. Bae, "Synthesis and characterization of Ag/Pd doped SiO2 nanoparticles by a reverse micelle and sol–gel processing," *Colloids and Surfaces A: Physicochemical and Engineering Aspects,* vol. 313–314, pp. 105-107, 2008.

[26] Y. Wang, X. Teng, J.-S. Wang, and H. Yang, "Solvent-Free Atom Transfer Radical Polymerization in the Synthesis of Fe2O3@Polystyrene Core−Shell Nanoparticles," *Nano Letters,* vol. 3, pp. 789-793, 2003/06/01 2003.

[27] A. M. Boies, "Gas-Phase Synthesis of Gold- and Silica-Coated Nanoparticles," Ph.D. 3461694, University of Minnesota, Twin Cities, 2011.

[28] F. Yu, J. N. Wang, Z. M. Sheng, and L. F. Su, "Synthesis of carbon-encapsulated magnetic nanoparticles by spray pyrolysis of iron carbonyl and ethanol," *Carbon,* vol. 43, pp. 3018-3021, Nov 2005.

[29] S. Jain, G. P. Fotou, and T. T. Kodas, "A Theoretical Study on Gas-Phase Coating of Aerosol Particles," *Journal of Colloid and Interface Science,* vol. 185, pp. 26-38, 1997.

[30] B. S. Lee, D. J. Kang, and S. G. Kim, "Properties of binary TiO2-SiO2 composite particles with various structures prepared by vapor phase hydrolysis," *Journal of Materials Science,* vol. 38, pp. 3545-3552, Sep 2003.

[31] Q. H. Powell, G. P. Fotou, T. T. Kodas, and B. M. Anderson, "Synthesis of alumina- and alumina/silica-coated titania particles in an aerosol flow reactor," *Chemistry of Materials,* vol. 9, pp. 685-693, Mar 1997.

[32] L. Zhang, M. B. Ranade, and J. W. Gentry, "Formation of organic coating on ultrafine silver particles using a gas-phase process," *Journal of Aerosol Science,* vol. 35, pp. 457-471, Apr 2004.

[33] A. M. Nienow and J. T. Roberts, "Chemical vapor deposition of zirconium oxide on aerosolized silicon nanoparticles," *Chemistry of Materials,* vol. 18, pp. 5571-5577, Nov 2006.

[34] P. Biswas, C. Y. Wu, M. R. Zachariah, and B. McMillin, "Characterization of iron oxide-silica nanocomposites in flames .2. Comparison of discrete-sectional model predictions to experimental data," *Journal of Materials Research,* vol. 12, pp. 714-723, Mar 1997.

[35] B. K. McMillin, P. Biswas, and M. R. Zachariah, "In situ characterization of vapor phase growth of iron oxide-silica nanocomposites .1. 2-D planar laser-induced fluorescence and Mie imaging," *Journal of Materials Research,* vol. 11, pp. 1552-1561, Jun 1996.

[36] K. S. Kim, D. J. Kim, and Q. Q. Zhao, "Numerical analysis on particle coating by the pulsed plasma process," *Chemical Engineering Science,* vol. 61, pp. 3278-3289, May 2006.

[37] M. Schallehn, M. Winterer, T. E. Weirich, U. Keiderling, and H. Hahn, "In-situ preparation of polymer-coated alumina nanopowders by chemical vapor synthesis," *Chemical Vapor Deposition,* vol. 9, pp. 40-44, Jan 2003.

[38] D. Vollath and D. V. Szabo, "Coated nanoparticles: A new way to improved nanocomposites," *Journal of Nanoparticle Research,* vol. 1, pp. 235-242, Jun 1999.

[39] Q. Ou, T. Tanaka, M. Mesko, A. Ogino, and M. Nagatsu, "Characteristics of graphene-layer encapsulated nanoparticles fabricated using laser ablation method," *Diamond and Related Materials,* vol. 17, pp. 664-668, 2008.

[40] K. Sakiyama, K. Koga, T. Seto, M. Hirasawa, and T. Orii, "Formation of Size-Selected Ni/NiO Core−Shell Particles by Pulsed Laser Ablation," *The Journal of Physical Chemistry B,* vol. 108, pp. 523-529, 2004/01/01 2003.

[41] A. Ceylan, A. K. Rumaiz, and S. I. Shah, "Inert gas condensation of evaporated Ni and laser ablated CoO," *Journal of Applied Physics,* vol. 101, p. 6, May 2007.

[42] H. Y. Kwong, M. H. Wong, C. W. Leung, Y. W. Wong, and K. H. Wong, "Formation of core/shell structured cobalt/carbon nanoparticles by pulsed laser ablation in toluene," *Journal of Applied Physics,* vol. 108, Aug 2010.

[43] G. Bajaj, A. Chaudhary, H. Naaz, B. Kumar, and R. K. Soni, *Laser ablation synthesis of Zn/ZnO core-shell nanoparticles*, First ed. New York: IEEE, 2007.

[44] D. C. Schinca, L. B. Scaffardi, F. A. Videla, G. A. Torchia, P. Moreno, and L. Roso, "Silver-silver oxide core-shell nanoparticles by femtosecond laser ablation: core and shell sizing by extinction spectroscopy," *Journal of Physics D-Applied Physics,* vol. 42, Nov 2009.

[45] H. F. Han, Y. Fang, Z. P. Li, and H. X. Xu, "Tunable surface plasma resonance frequency in Ag core/Au shell nanoparticles system prepared by laser ablation," *Applied Physics Letters,* vol. 92, Jan 2008.

[46] Y. K. Jo and S. B. Wen, "Direct generation of core/shell nanoparticles from double-pulse laser ablation in a background gas," *Journal of Physics D-Applied Physics,* vol. 44, Aug 2011.

[47] I. Gallardo, K. Hoffmann, and J. W. Keto, "CdSe & ZnS core/shell nanoparticles generated by laser ablation of microparticles," *Applied Physics a-Materials Science & Processing,* vol. 94, pp. 65-72, Jan 2009.

[48] F. Bozon-Verduraz, R. Brayner, V. V. Voronov, N. A. Kirichenko, A. V. Simakin, and G. A. Shafeev, "Production of nanoparticles by laser-induced ablation of metals in liquids," *Quantum Electronics,* vol. 33, pp. 714-720, Aug 2003.

[49] S. I. Dolgaev, A. V. Simakin, V. V. Voronov, G. A. Shafeev, and F. Bozon-Verduraz, "Nanoparticles produced by laser ablation of solids in liquid environment," *Applied Surface Science,* vol. 186, pp. 546-551, 2002.

[50] A. T. Izgaliev, A. V. Simakin, and G. A. Shafeev, "Formation of the alloy of Au and Ag nanoparticles upon laser irradiation of the mixture of their colloidal solutions," *Quantum Electronics,* vol. 34, pp. 47-50, Jan 2004.

[51] D. Babonneau, J. Toudert, S. Camelio, F. Pailloux, T. Cabioc'h, and T. Girardeau, "Encapsulation of metallic nanoclusters in carbon and boron nitride thin films prepared by ion-beam sputtering," *Surface and Coatings Technology,* vol. 200, pp. 6251-6257, 2006.

[52] C. Liu, "A study of particle generation during laser ablation with applications," Ph.D. 3211429, University of California, Berkeley, 2005.

[53] S. B. Wen, "Experimental and theoretical study of laser ablation processes including vapor plume expansion, cooling, and condensation with an ambient gas," Ph.D, Mechanical engineering, University of California, Berkeley, 2006.

[54] S. B. Wen, R. Greif, and R. E. Russo, "Background gas effects on the generation of nanopatterns on a pure silicon wafer with multiple femtosecond near field laser ablation," *Applied Physics Letters,* vol. 91, pp. 251113 - 251113-3 Dec 2007.

[55] S. B. Wen, X. L. Mao, R. Greif, and R. E. Russo, "Experimental and theoretical studies of particle generation after laser ablation of copper with a background gas at atmospheric pressure," *Journal of Applied Physics,* vol. 101, pp. 123105-123105-15, Jun 2007.

[56] S. B. Wen, X. L. Mao, R. Greif, and R. E. Russo, "Laser ablation induced vapor plume expansion into a background gas. II. Experimental analysis," *Journal of Applied Physics,* vol. 101, pp. 023115 - 023115-14 Jan 2007.

[57] S. B. Wen, X. L. Mao, R. Greif, and R. E. Russo, "Expansion of the laser ablation vapor plume into a background gas. I. Analysis," *Journal of Applied Physics,* vol. 101, pp. 023114 - 023114-13 Jan 2007.

[58] Y. Ralchenko, Kramida, A.E., Reader, J., and NIST ASD Team. NIST Atomic Spectra Database (ver. 4.1.0), [Online]. Available: http://physics.nist.gov/asd [Online].

[59] B. S. Luk'yanchuk, W. Marine, and S. I. Anisimov, "Condensation of vapor and nanoclusters formation within the vapor plume, produced by ns-laser ablation of Si," *Laser Physics,* vol. 8, pp. 291-302, Jan-Feb 1998.

[60] T. Ohkubo, M. Kuwata, B. Luk'yanchuk, and T. Yabe, "Numerical analysis of nanocluster formation within ns-laser ablation plume," *Applied Physics a-Materials Science & Processing,* vol. 77, pp. 271-275, 2003.

[61] M. Ullmann, S. K. Friedlander, and A. Schmidt-Ott, "Nanoparticle Formation by Laser Ablation," *Journal of Nanoparticle Research,* vol. 4, pp. 499-509, 2002.

[62] V. P. Carey, *Liquid-Vapor Phase-Change Phenomena*, Second ed. New York: Taylor&Francis Group, 2008.

[63] E. Bertrand, T. D. Blake, and J. De Coninck, "Influence of solid-liquid interactions on dynamic wetting: a molecular dynamics study," *Journal of Physics-Condensed Matter,* vol. 21, Nov 2009.

[64] T. D. Blake and J. De Coninck, "The influence of solid-liquid interactions on dynamic wetting," *Advances in Colloid and Interface Science,* vol. 96, pp. 21-36, Feb 2002.

[65] T. D. Blake and J. M. Haynes, "Kinetics of liquid/liquid displacement," *Journal of Colloid and Interface Science,* vol. 30, pp. 421-&, 1969.

[66] D. A. Shashkov, "Atomic-Scale Studies of the Structure and Chemistry of Ceramic/Metal Heterophase Interfaces," Ph.D, Northwestern University, Illinois, Evanston, 1997.

[67] H. Vehkamäki, *Classical nucleation theory in multicomponent systems*, First ed. Berlin: Springer Berlin Heidelberg 2006.

[68] T. Ujihara, G. Sazaki, K. Fujiwara, N. Usami, and K. Nakajima, "Physical model for the evaluation of solid-liquid interfacial tension in silicon," *Journal of Applied Physics,* vol. 90, pp. 750-755, Jul 2001.

[69] P. S. Elizabeth Allen, Jim Henshaw, "A review of particle agglomeration," US Department of Energy 2001.

[70] O. Yavas, P. Leiderer, H. K. Park, C. P. Grigoropoulos, C. C. Poon, and A. C. Tam, "Enhanced acoustic cavitation following laser-induced bubble formation: Long-term memory effect," *Physical Review Letters,* vol. 72, pp. 2021-2024, 1994.

[71] O. Yavas, P. Leiderer, H. K. Park, C. P. Grigoropoulos, C. C. Poon, W. P. Leung, N. Do, and A. C. Tam, "Optical and acoustic study of nucleation and growth of bubbles at a liquid-solid interface induced by nanosecond-pulsed-laser heating," *Applied Physics A: Materials Science & Processing,* vol. 58, pp. 407-415, 1994.

[72] H. K. Park, C. P. Grigoropoulos, C. C. Poon, and A. C. Tam, "Optical probing of the temperature transients during pulsed-laser induced boiling of liquids," *Applied Physics Letters,* vol. 68, pp. 596-598, 1996.

[73] H. K. Park, X. Zhang, C. P. Grigoropoulos, C. C. Poon, and A. C. Tam, "Transient Temperature During the Vaporization of Liquid on a Pulsed Laser-Heated Solid Surface," *Journal of Heat Transfer,* vol. 118, pp. 702-708, 1996.

[74] H. K. Park, D. Kim, C. P. Grigoropoulos, and A. C. Tam, "Pressure generation and measurement in the rapid vaporization of water on a pulsed-laser-heated surface," *Journal of Applied Physics,* vol. 80, pp. 4072-4081, 1996.

[75] L. Berthe, R. Fabbro, P. Peyre, L. Tollier, and E. Bartnicki, "Shock waves from a water-confined laser-generated plasma," *Journal of Applied Physics,* vol. 82, pp. 2826-2832, 1997.

[76] L. Berthe, A. Sollier, P. Peyre, R. Fabbro, and E. Bartnicki, "The generation of laser shock waves in a water-confinement regime with 50 ns and 150 ns XeCl excimer laser pulses," *Journal of Physics D: Applied Physics,* vol. 33, p. 2142, 2000.

[77] M. S. El-Shall, S. Li, T. Turkki, D. Graiver, U. C. Pernisz, and M. I. Baraton, "Synthesis and Photoluminescence of Weblike Agglomeration of Silica Nanoparticles," *The Journal of Physical Chemistry,* vol. 99, pp. 17805-17809, 1995/12/01 1995.

[78] S. I. Dolgaev, A. V. Simakin, V. V. Voronov, G. A. Shafeev, and F. Bozon-Verduraz, "Nanoparticles produced by laser ablation of solids in liquid environment," *Applied Surface Science,* vol. 186, pp. 546-551, 2002.

[79] B. Kumar, D. Yadav, and R. K. Thareja, "Growth dynamics of nanoparticles in laser produced plasma in liquid ambient," *Journal of Applied Physics,* vol. 110, pp. 074903-8, 2011.

[80] X. H. Huang, P. K. Jain, I. H. El-Sayed, and M. A. El-Sayed, "Gold nanoparticles: interesting optical properties and recent applications in cancer diagnostic and therapy," *Nanomedicine,* vol. 2, pp. 681-693, Oct 2007.

[81] M. A. Noginov, G. Zhu, A. M. Belgrave, R. Bakker, V. M. Shalaev, E. E. Narimanov, S. Stout, E. Herz, T. Suteewong, and U. Wiesner, "Demonstration of a spaser-based nanolaser," *Nature,* vol. 460, pp. 1110-1112, 2009.

[82] T. Ung, L. M. Liz-Marzan, and P. Mulvaney, "Optical properties of thin films of Au@SiO2 particles," *Journal of Physical Chemistry B,* vol. 105, pp. 3441-3452, May 2001.

[83] Y. Yang, J. Shi, H. Chen, S. Dai, and Y. Liu, "Enhanced off-resonance optical nonlinearities of Au@CdS core-shell nanoparticles embedded in BaTiO3 thin films," *Chemical Physics Letters,* vol. 370, pp. 1-6, 2003.

[84] Y. Wang, "Asymmetric crack problems calculated by the boundary collocation method," *Engineering Fracture Mechanics,* vol. 40, pp. 133-143, 1991.

[85] L. L. Beecroft and C. K. Ober, "Nanocomposite Materials for Optical Applications," *Chemistry of Materials,* vol. 9, pp. 1302-1317, 1997.

[86] Y. Hu, R. C. Fleming, and R. A. Drezek, "Optical properties of gold-silica-gold multilayer nanoshells," *Optics Express,* vol. 16, pp. 19579-19591, Nov 2008.

[87] C. Radloff and N. J. Halas, "Plasmonic Properties of Concentric Nanoshells," *Nano Letters,* vol. 4, pp. 1323-1327, 2004/07/01 2004.

[88] C. J. Radloff, "Concentric nanoshells and plasmon hybridization," Ph.D. 3122525, Rice University, Texas, Houston, 2004.

[89] H. Y. Lin, Y. F. Chen, J. G. Wu, D. I. Wang, and C. C. Chen, "Carrier transfer induced photoluminescence change in metal-semiconductor core-shell nanostructures," *Applied Physics Letters,* vol. 88, Apr 2006.

[90] P. V. Kamat and B. Shanghavi, "Interparticle Electron Transfer in Metal/Semiconductor Composites. Picosecond Dynamics of CdS-Capped Gold Nanoclusters," *The Journal of Physical Chemistry B,* vol. 101, pp. 7675-7679, 1997/09/01 1997.

[91] W. Lu, B. Wang, J. Zeng, X. P. Wang, S. Y. Zhang, and J. G. Hou, "Synthesis of core/shell nanoparticles of Au/CdSe via Au-Cd bialloy precursor," *Langmuir,* vol. 21, pp. 3684-3687, Apr 2005.

[92] B. R. Tull, J. E. Carey, M. A. Sheehy, C. Friend, and E. Mazur, "Formation of silicon nanoparticles and web-like aggregates by femtosecond laser ablation in a background gas," *Applied Physics a-Materials Science & Processing,* vol. 83, pp. 341-346, Jun 2006.

[93] S.-B. Wen, "Experimental and theoretical study of laser ablation processes including vapor plume expansion, cooling, and condensation with an ambient gas," Ph.D. 3254134, University of California, Berkeley, 2006.

[94] H. Vehkamäki, *Classical Nucleation Theory in Multicomponent Systems*, First ed. Berlin: Springer Berlin Heidelberg 2006.

[95] C. Loo, L. Hirsch, M. H. Lee, E. Chang, J. West, N. J. Halas, and R. Drezek, "Gold nanoshell bioconjugates for molecular imaging in living cells," *Optics Letters,* vol. 30, pp. 1012-1014, May 2005.

[96] A. R. Lowery, A. M. Gobin, E. S. Day, N. J. Halas, and J. L. West, "Immunonanoshells for targeted photothermal ablation of tumor cells," *International Journal of Nanomedicine,* vol. 1, pp. 149-154, 2006.

[97] D. Nagao, Y. Kon, T. Satoh, and M. Konno, "Electrostatic interactions in formation of particles from tetraethyl orthosilicate," *Journal of Chemical Engineering of Japan,* vol. 33, pp. 468-473, 2000.

[98] A. Van Blaaderen, J. Van Geest, and A. Vrij, "Monodisperse colloidal silica spheres from tetraalkoxysilanes: Particle formation and growth mechanism," *Journal of Colloid and Interface Science,* vol. 154, pp. 481-501, 1992.

[99] Y. Kobayashi, Y. Tadaki, D. Nagao, and M. Konno, "Deposition of gold nanoparticles on silica spheres by electroless metal plating technique," *Journal of Colloid and Interface Science,* vol. 283, pp. 601-604, 2005.

[100] W. Stöber, A. Fink, and E. Bohn, "Controlled growth of monodisperse silica spheres in the micron size range," *Journal of Colloid and Interface Science,* vol. 26, pp. 62-69, 1968.

[101] K. S. S. Harsha, *Principles of Physical Vapor Deposition of Thin Films*, First ed. San Diego: Elsevier Ltd., 2006.

[102] C. T. Campbell, "Ultrathin metal films and particles on oxide surfaces: Structural, electronic and chemisorptive properties," *Surface Science Reports,* vol. 27, pp. 1-111, 1997.

[103] R. Sangiorgi, M. L. Muolo, D. Chatain, and N. Eustathopoulos, "Wettability and work of adhesion of nonreactive liquid-metals on silica," *Journal of the American Ceramic Society,* vol. 71, pp. 742-748, Sep 1988.

[104] L. M. Liz-Marzán, "Nanometals: formation and color," *Materials Today,* pp. 26-31, Apr 2004.

[105] S. A. MAIER, *Plasmonics: Fundamentals and Applications*, First ed. New York: Springer, 2007.

[106] Z. Q. Tian, B. Ren, J. F. Li, and Z. L. Yang, "Expanding generality of surface-enhanced Raman spectroscopy with borrowing SERS activity strategy," *Chemical Communications,* pp. 3514-3534, Sep 2007.

[107] S. Moon, Y. Kim, Y. Oh, H. Lee, H. C. Kim, K. Lee, and D. Kim, "Grating-based surface plasmon resonance detection of core-shell nanoparticle mediated DNA hybridization," *Biosensors and Bioelectronics,* vol. 32, pp. 141-147, 2012.

[108] O. G. Tovmachenko, C. Graf, D. J. van den Heuvel, A. van Blaaderen, and H. C. Gerritsen, "Fluorescence enhancement by metal-core/silica-shell nanoparticles," *Advanced Materials,* vol. 18, pp. 91-95, Jan 2006.

[109] S. J. Oldenburg, R. D. Averitt, S. L. Westcott, and N. J. Halas, "Nanoengineering of optical resonances," *Chemical Physics Letters,* vol. 288, pp. 243-247, May 1998.

[110] W. L. Shi, Y. Sahoo, M. T. Swihart, and P. N. Prasad, "Gold nanoshells on polystyrene cores for control of surface plasmon resonance," *Langmuir,* vol. 21, pp. 1610-1617, Feb 2005.

[111] N. Phonthammachai, J. C. Y. Kah, G. Jun, C. J. R. Sheppard, M. C. Olivo, S. G. Mhaisalkar, and T. J. White, "Synthesis of contiguous silica-gold core-shell structures: Critical parameters and processes," *Langmuir,* vol. 24, pp. 5109-5112, May 2008.

[112] K. S. Chou and Y. C. Lu, *Preparation and characterization of Ag nanoshell on SiO(2) spheres via electroless plating technique in acidic conditions*, First ed. New York: IEEE, 2006.

[113] V. G. Pol, A. Gedanken, and J. Calderon-Moreno, "Deposition of gold nanoparticles on silica spheres: A sonochemical approach," *Chemistry of Materials,* vol. 15, pp. 1111-1118, Mar 2003.

[114] D. R. H. Craig F. Bohren, *Absorption and Scattering of Light by Small Particles* First ed. San Francisco: John Wiley & Sons, Inc, 1983.

[115] A. L. Aden and M. Kerker, "Scattering of Electromagnetic Waves from Two Concentric Spheres," *Journal of Applied Physics,* vol. 22, pp. 1242-1246, 1951.

[116] J. C. Heckel, "Synthesis and optical properties of silver nanostructures," Ph.D. 3439351, Clemson University, South Carolina, Clemson, 2010.

[117] E. D. Palik, *Handbook of Optical Constants of Solids*, First ed. Oxford: Elsevier, 1998.

VITA

Name: Young Kyong Jo

Address: Texas A&M University
Department of Mechanical Engineering
3123 TAMU
College Station TX 77843

E-mail Address: j2y509@gmail.com

Education: B.E., Mechanical Engineering, Kyung Hee University, Republic of Korea, 2004
M.E., Mechanical Engineering, Kyung Hee University, Republic of Korea, 2006